Experimental investigation of the effects of windscreens on air-cooled condenser fan performance and dynamic blade loading

by
Fredrik Simon Marincowitz

Thesis presented in partial fulfilment of the requirements for the degree of Master of Engineering (Mechanical) in the Faculty of Engineering at Stellenbosch University

Supervisor: Dr MTF Owen
Co-supervisor: Dr J Muiyser

April 2019

Declaration

By submitting this thesis electronically, I declare that the entirety of the work contained therein is my own, original work, that I am the sole author thereof (save to the extent explicitly otherwise stated), that reproduction and publication thereof by Stellenbosch University will not infringe any third party rights and that I have not previously in its entirety or in part submitted it for obtaining any qualification.

Date: .....April 2019.....

UNIVERSITEIT·STELLENBOSCH·UNIVERSITY
jou kennisvennoot • your knowledge partner

Plagiaatverklaring / *Plagiarism Declaration*

1 Plagiaat is die oorneem en gebruik van die idees, materiaal en ander intellektuele eiendom van ander persone asof dit jou eie werk is.
Plagiarism is the use of ideas, material and other intellectual property of another's work and to present is as my own.

2 Ek erken dat die pleeg van plagiaat 'n strafbare oortreding is aangesien dit 'n vorm van diefstal is.
I agree that plagiarism is a punishable offence because it constitutes theft.

3 Ek verstaan ook dat direkte vertalings plagiaat is.
I also understand that direct translations are plagiarism.

4 Dienooreenkomstig is alle aanhalings en bydraes vanuit enige bron (ingesluit die internet) volledig verwys (erken). Ek erken dat die woordelikse aanhaal van teks sonder aanhalingstekens (selfs al word die bron volledig erken) plagiaat is.
Accordingly all quotations and contributions from any source whatsoever (including the internet) have been cited fully. I understand that the reproduction of text without quotation marks (even when the source is cited) is plagiarism.

5 Ek verklaar dat die werk in hierdie skryfstuk vervat, behalwe waar anders aangedui, my eie oorspronklike werk is en dat ek dit nie vantevore in die geheel of gedeeltelik ingehandig het vir bepunting in hierdie module/werkstuk of 'n ander module/werkstuk nie.
I declare that the work contained in this assignment, except otherwise stated, is my original work and that I have not previously (in its entirety or in part) submitted it for grading in this module/assignment or another module/assignment.

FS Marincowitz **Voorletters en van / *Initials and surname***	**April 2019** **Datum / *Date***

Abstract

Experimental investigation of the effects of windscreens on air-cooled condenser fan performance and dynamic blade loading

F.S. Marincowitz

Department of Mechanical and Mechatronic Engineering,
University of Stellenbosch,
Private Bag X1, 7602 Matieland, South Africa.

Thesis: MEng (Mech)

April 2019

Air-cooled condensers (ACCs) are the preferred cooling method for power plants that make use of the Rankine cycle in regions that have limited water resources. However, using air as the cooling fluid has its limitations as environmental conditions such as wind affects ACCs thermal performance. Wind specifically influences the ACCs perimeter fans, as the strong cross-flow caused by winds results in distorted inflow conditions which lead to a reduction in fan performance and excessive dynamic blade loading. One method used to mitigate these effects is the use of windscreens along the perimeter of the fan platform, but studies done on this topic are however inconclusive as computational fluid dynamics (CFD) studies indicate windscreens help increase perimeter fan performance while site specific full-scale experimental studies indicate windscreens are mostly beneficial in reducing the dynamic blade loading. As the exact influence of windscreens on the perimeter fans appears to be not well understood, a controllable and repeatable experimental investigation was deemed a good method to aid in this understanding. This experimental investigation was then done on a scaled ACC fan row at a fixed platform height, consisting of 3 fans, and subjected to a controllable cross-flow to simulate wind. Using this test setup, the fan performance and dynamic blade loading under strong cross-flow could be investigated and used as a baseline to compare with the results once a windscreen was installed. The results indicated that with increasing cross-flow the performance of the perimeter fan suffered increasingly due to the formation of a separation region on the upstream edge of the bellmouth. This then resulted in a significant difference between the up-and downstream velocity profiles into the perimeter fan (perpendicular to the blade) which led to an increase in the dynamic loading on the fan blade. With the installation of a windscreen the perimeter fan's performance was mostly negatively affected as the majority of the incoming flow was deflected away from the intake of the perimeter fan, and the flow permeating through the windscreen was insufficient to help improve the performance. In most cases the windscreen did however help to reduce the difference in up-and downstream velocity profiles into the perimeter fan, reducing the dynamic blade loading on the perimeter fan. Where the fan performance results with and without a windscreen, for the scaled ACC fan row, had very similar trends to that recorded at a full-scale facility of a similar

dimensionless platform height which instilled confidence in the experimental methods used.

Uittreksel

Eksperimentele ondersoek na die effekte van windskerms op lug-verkoelde kondensor waaier en dinamiese lem belasting

("*Experimental investigation of the effects of windscreens on air-cooled condenser fan performance and dynamic blade loading*")

F.S. Marincowitz

Departement Meganiese en Megatroniese Ingenieurswese,
Universiteit van Stellenbosch,
Privaatsak X1, Matieland 7602, Suid Afrika.

Tesis: MIng (Meg)

April 2019

Lugverkoelde kondensors (LVKs) is die verkose afkoel metode vir kragsentrales wat gebruik maak van die "Rankine" siklus in gebiede met beperkte waterbronne. Die gebruik van lug as verkoelings medium het egter sy beperkings as gevolg van verskeie omgewings veranderlikes, insluitend wind effekte. Sterk atmosferiese wind veroorsaak 'n daling in die LVK se termiese vermoë. Die wind beïnvloed spesifiek die LVKs se randwaaiers, as gevolg van kruisvloei wat deur die wind veroorsaak word, dié lei tot versteurings in die invloeipatrone van die waaiers en lei tot 'n afname in die waaier se volumetriese vermoë asook 'n toename in die dinamiese belasting van die waaierlemme. Een metode wat gebruik word om hierdie effekte te verminder, is die gebruik van windskerms wat geïnstalleer word om die rand van die waaierplatform. Die studies wat oor hierdie onderwerp gedoen is, is egter onbeslis omdat die numeriese vloei dinamika studies (NVD) aandui dat windskerms help om die randwaaiers se volumetriese vermoë te verbeter onder winderige toestande, terwyl volskaalse eksperimentele studies dui dat windskerms meestal net voordelig is om die dinamiese lembelasting te verminder. Omdat die presiese invloed wat windskerms het op LVKs nie goed gedokumenteer is nie, is 'n beheerbare en herhaalbare eksperimentele ondersoek 'n goeie metode om begrip van die onderwerp te verbeter. So 'n eksperimentele ondersoek is gedoen op 'n afgeskaalde LVK waaier ry met 'n vaste platformhoogte, bestaande uit 3 waaiers, wat onderworpe was aan 'n beheerbare kruisvloei met die doel om wind te simuleer. Deur hierdie toets opstelling te gebruik, kon die waaier se volumetriese vermoë en dinamiese lembelasting onder sterk kruisvloei ondersoek word en as 'n maatstaf gebruik word om die veranderinge wat 'n windskerm aan die waaier se volumetriese vermoë en dinamiese lembelasting aanbring mee te vergelyk. Die resultate het aangedui dat met toenemende kruisvloei neem die volumetriese vermoë van die randwaaier slegs af as gevolg van die formasie van 'n vloei weg brekings gebied op die op stroom rand van die waaierinlaat. Dit het gelei tot 'n beduidende verskil in die op- en afwaartse stroom invloei snelheidsprofiele van die waaier (loodreg met die lem) en gelui het tot 'n toename in die dinamiese lem belasting. Die installasie van 'n windskerm het die volumetriese vermoë van die randwaaier meestal negatief

beïnvloed, aangesien die meerderheid van die inkomende vloei gedeflekteer was deur die windskerm en die vloei wat wel deur die windskerm beweeg het onvoldoende was. In die meeste gevalle het die windskerm egter gehelp om die verskil in op- en afwaartse snelheidsprofiele van die waaier se invloei te verminder, en daarmee saam die dinamiese lembelasting. Die toetse wat op die geskaleerde waaierry gedoen was, met en sonder 'n windskerm, het baie soortgelyke tendense gelewer as wat bevind was op 'n volskaalse LVK met dieselfde dimensielose platformhoogte, wat dus vertroue verleen aan die eksperimentele metodes wat in hierdie studie toegepas is.

Acknowledgements

I would like to give special thanks to my two supervisors, Michael and Jacques for their continuous support, excellent advice and patience over the past two years. To my parents for their never-ending support and motivations. To John Wahl for his help with the final editing of the report. To the workshop staff for their help with all the experimental procedures. Finally, to Howden Netherlands B.V. for their financial support over the past two years.

Table of contents

List of figures

Page

List of tables

Nomenclature

Abbreviations

ACC	Air-cooled condenser
ADM	Actuator disk model
DAQ	Data acquisition
NS	No-screen
NW	No-wind
PIV	Particle imagery velocimetry
rms	Root mean square
VSD	Variable speed drive

Variables

A	Area	[m^2]
d	Diameter	[m]
E	Voltage output	[V]
f	Frequency	[1/s]
g	Gravitational constant	[m/s^2]
H	Platform height; height	[m]
N	Fan rotational speed	[rpm]
p	Pressure	[Pa]
P	Power	[W]
r	Radius	[m]
t	Time	[s]
T	Torque	[N·m]

T	Temperature	[K]
v	Velocity	[m/s]
V	Volumetric flow rate	[m^3/s]
w	Humidity ratio	
W	Width	[m]

Greek Symbols

α	Solidity	
β	Dimensionless cross-flow	
ε	Strain	
μ	Viscosity	[m^2/s]
ρ	Density	[kg/m^3]
ξ	Volumetric effectiveness	
σ	Standard deviation	
Ω	Fan rotational frequency	[1/s]

Subscripts

a	Air
abs	Absolute
amb	Ambient
dyn	Dynamic
f	Fan
h	Hydraulic
hex	Hex-core
id	Ideal

in	Induced
m	Measured
n	Nozzle; natural
ns	No-screen
nw	No-wind
pl	Plenum
ref	Reference
s	Static
sf	Static fan
sys	System
t	Total
w	Wind
wa	Wind average
wb	Wet bulb
wp	Wind profile
ws	Windscreen
x	*x*-direction, cross-flow
y	*y*-direction
z	*z*-direction

1 Introduction

1.1 Background

Energy generation using steam as a working fluid makes use of the Rankine cycle. The Rankine cycle consists of four processes namely (Figure 1): (1-2) compression of the working fluid (pump), (2-3) heat addition (boiler), (3-4) expansion of the working fluid (turbine) and (4-1) heat rejection (condenser). Electrical energy is generated as the fluid is expanded in the turbine. Globally the majority of electrical energy is generated using steam power stations (Cengel and Boles, 2011).

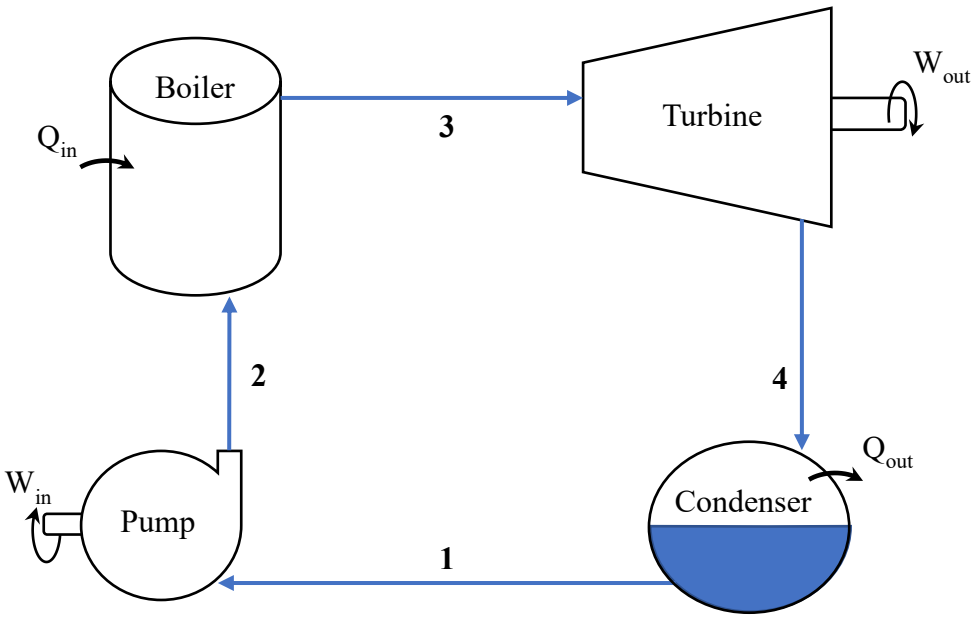

Figure 1: Rankine cycle (Adapted from Cengel and Boles (2011))

High thermal efficiency is very important as it indicates the extent to which energy added can be converted to work, in this case, electrical energy. High efficiency can be achieved in the Rankine cycle when the boiler is operated at the highest possible pressure by generating superheated steam at the highest possible temperature, and the condenser is operating at the lowest possible pressure (Cengel and Boles, 2011).

Considering the condenser only, the efficiency of a Rankine cycle depends on the ability of the condenser to perform at the specified turbine back pressure (lowest possible pressure). The condenser makes use of a heat exchanger to reject heat from the incoming turbine exhaust steam and subsequently reduce the steam to condensate. Condensers typically reject heat to either water (wet cooling) or

ambient air (dry cooling) and in some cases a combination of the two (hybrid cooling) (Kröger, 2004).

Wet cooling systems are globally the most common method of power plant cooling (Maulbetsch and DiFilippo, 2008). Modern wet-cooling systems typically require an average of between 1.6 and 2.5 liters of cooling water per kWh of cooling load (Kröger, 2004). This is what accounts for more than 80% of a plant's total water usage (DiFilippo, 2008).

Considering that only 0.01% of the world's water is considered as fresh water which sustains the life of almost 6% of all earth's species, overexploitation of freshwater resources is a major concern to freshwater biodiversity (Dudgeon *et al.*, 2006) and the sustainability of water resources (Barker, 2007). As a result, regulations on the use of fresh water for power plant cooling are being implemented increasingly (Gadhamshetty *et al.*, 2006).

In arid regions with limited fresh water supplies, dry cooling systems are often used instead of wet cooling (Kröger, 2004). Dry cooling is considered a good alternative to reduce the consumption of fresh water resources and is finding increasing application worldwide.

Dry cooling systems are operated either directly or indirectly. In an indirect system, cooling water is cycled through a secondary loop that is used to condense steam, the added heat is subsequently rejected through a natural or mechanical draft cooling tower. Alternatively, in a direct system, turbine exhaust steam is condensed directly in an air-cooled steam condenser (ACC) (Kröger, 2004).

ACCs are mechanically operated where the air is either forced or induced through a finned tube heat exchanger bundle (Kröger, 2004). Forced draft ACCs make use of large axial fans to force ambient air through the heat exchangers. A single "fan unit" or "cell" of a forced draft A-frame ACC is shown in Figure 2. The low-pressure steam leaving the turbine exhaust is ducted to steam headers that run along the apex of a row of several fan units in the ACC. The finned tubes are normally arranged in an A-frame configuration to reduce the ACC footprint and to help with the drainage of condensate (Kröger, 2004). ACCs consist of multiple cells to increase the heat transfer potential of the plant.

Due to air having poor thermophysical properties (low specific heat and density) ACCs require large volumes of air to be circulated through the heat exchanger bundles (Kröger, 2004). To maximize the heat transfer, all the tubes within the heat exchange bundles are typically externally finned.

Using ambient air as the cooling medium adds a limitation on the performance of the condenser as forced draft ACCs are strongly influenced by ambient conditions such as ambient temperature and wind (Maulbetsch and DiFilippo, 2008). High winds or temperatures cause a reduction in the ACC's heat transfer rate which

increases the turbine back pressure and subsequently reduces the efficiency of the Rankine cycle.

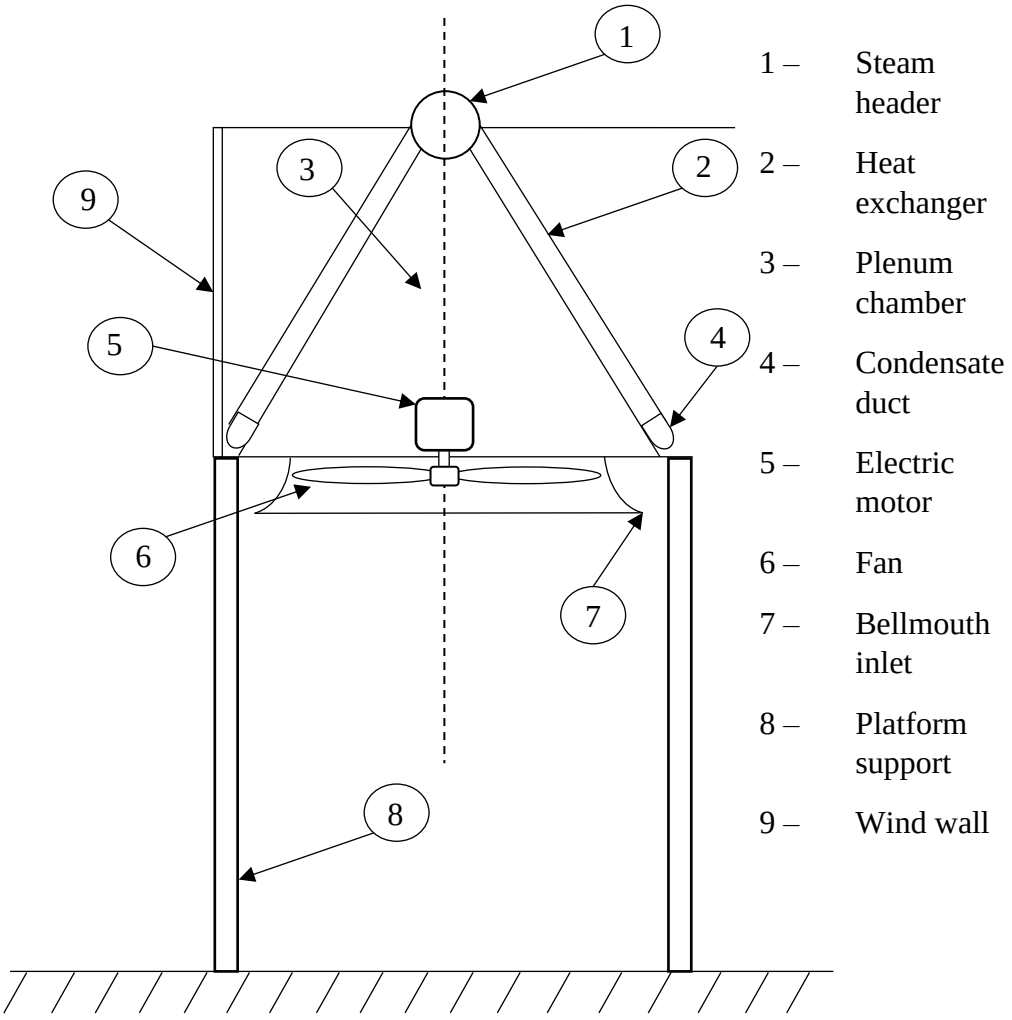

Figure 2: Single cell of an A-frame forced draft ACC

Under windy conditions, a reduction in air flow through the ACC due to the loss in fan performance on the windward side perimeter fans appears to be the most influential mechanism causing a reduction in the thermal performance of the ACCs (Maulbetsch and DiFilippo, 2008). Because of this reduction in the perimeter fan's performance, the A-frame heat exchanger's heat transfer rate becomes less, due to the air moving through the heat exchanger having a lower velocity.

The reduction in fan performance is due to the distorted fan inlet conditions caused by wind or any form of cross-flow (van der Spuy, 2011). These conditions also lead to vibration of the perimeter fans due to the variation in aerodynamic loading as the fan blades rotate around the axis (Muiyser *et al.*, 2016). Excessive blade vibration

can lead to gearbox damage, blade fatigue and even total blade failure (Muiyser *et al.*, 2016).

Numerous methods of mitigating the negative effects of wind on ACC fan performance have been investigated (Section 2.2 presents a detailed review of the relevant literature). A relatively new approach involves the installation of windscreens or wind barriers in various configurations in an attempt to reduce the adverse effects of winds (Maulbetsch and DiFilippo, 2008). This study will experimentally investigate the effect of perimeter windscreens (Figure 3) on ACC fan performance and dynamic blade loading.

Figure 3: Perimeter windscreen at Caithness Energy Center in New York, USA (J. Maulbetsch and DiFilippo, 2016)

Due to the physical scale of ACCs and the dynamic nature of ambient winds the study had to be conducted on a scaled ACC fan row subject to a simulated wind. The multiple fan test facility, as shown in Figure 4, was ideally suited for the study as it was originally designed to model an ACC fan row (Visser, 1990), although multiple modifications had to be made, these are discussed later in Section 3.2.

Figure 4: Multiple fan testing facility (van der Spuy, 2011)

1.2 Problem statement

Multiple studies have been conducted on the wind effects of air-cooled condensers and methods to counter the subsequent adverse effects (discussed within the literature study). One such method is the use of perimeter windscreens to improve fan performance and reduce dynamic blade loading.

Site-specific experimental studies (Maulbetsch and DiFilippo, 2016) indicated that perimeter windscreens are beneficial to reduce dynamic blade loading under windy conditions whilst computational fluid dynamics (CFD) investigations (Zhang and Chen, 2015) indicate that perimeter windscreens are beneficial to ACC fan performance, but the exact reasons why and how are not well understood (see Section 2.2 for detail). Due to the scale of ACCs and the dynamic nature of ambient winds, full-scale experimental studies and verified CFD studies are extremely difficult to achieve and tend to generate results with somewhat limited application and are generally considered to be site specific.

From literature, experimental studies indicate that perimeter windscreens are beneficial for dynamic blade loading but cannot provide enough conclusive evidence that they would improve the volumetric performance of the ACC perimeter fans (Maulbetsch and DiFilippo, 2016). CFD studies indicate that perimeter windscreens do, in fact, increase the volumetric performance of the perimeter fans, but uncertainty exists about the validation of these CFD models.

1.3 Project aim and objectives

The project aim is to experimentally investigate the effect that perimeter windscreens have on a scaled ACC fan row's fan performance and perimeter fan dynamic blade loading under simulated wind conditions. The influence of the windscreens on the fan performance and blade loading will be investigated for different percentages of the windward inlet covered by screens under increasing cross-flow conditions. The results of this study will enhance the understanding of how windscreens affect fan performance, as well as the dynamic blade loading of the perimeter fan and will be used in a follow-on numerical study as verification for the CFD model. This is required to develop a well verified CFD modeling technique in an attempt to increase the validity of full-scale ACC CFD models that are used to investigate the effects of windscreens.

The experimental investigation will entail simulating a controllable cross-flow wind with a uniform flow pattern across a scaled fan row. The following specific objectives are relevant:

1. Modify Stellenbosch University's multiple fan test facility to be able to simulate cross-flow wind conditions at a fixed platform height.

2. Experimentally investigate the effect that increasing cross-flow has on the fan performance of an ACC fan row as well as the dynamic blade loading of the perimeter fan. Also, to investigate the subsequent effect on both parameters after the installation of a perimeter windscreen and noting the influence of varying screen coverage and solidity.

3. Generate high-quality velocity field visualizations in the vicinity of the perimeter fans for the purpose of better understanding the wind effects and how windscreens influence this flow field.

2 Literature review

2.1 Wind effects on ACC fans

Prevailing winds cause an increase in inlet flow distortions which result in a reduction of fan performance because of maldistribution of air at the fan inlet. Inlet flow distortions are primarily caused by separation at the perimeter fans inlets due to strong cross-flow (Bredell *et al.*, 2006). The effect of inlet flow distortions under windy conditions is predominant on upwind perimeter fans (Maulbetsch and DiFilippo, 2008).

The performance of fans operating under inlet flow distortions can be defined through the volumetric effectiveness of the fan. Volumetric effectiveness (ξ) is defined as the ratio of actual flow rate (V) through a fan to the "ideal" flow rate (V_{id}) when the fan is operating with no inlet flow distortions (Salta and Kröger, 1995) and is given by Equation 1.

$$\xi = \frac{V}{V_{ID}} \tag{1}$$

Although wind increases inlet flow distortions at the perimeter fans it is not necessarily the only cause, as induced cross-flow can also be a significant contributor to these observed effects. Induced cross-flow is caused by the interior fans drawing air in past the perimeter fan, Figure 5 shows a schematic of a fan row subjected to wind and induced cross-flow.

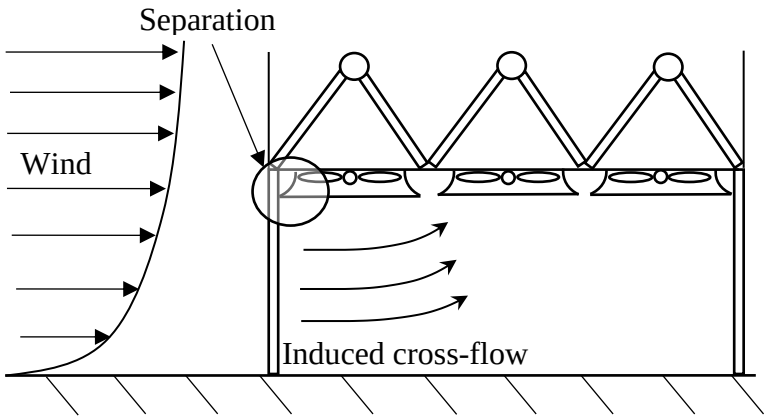

Figure 5: ACC fan row subjected to inlet flow distortions

Induced cross-flow would increase with a reduction in the platform height (H) or by increasing the number of fans in the fan row. Both contribute to an increased induced cross-flow velocity past the perimeter fan, increasing the scale of inlet flow

distortions present at the inlet of the perimeter fan. As such the induced cross-flow causes the volumetric effectiveness of the perimeter fans to always be lower than the inner fans (Salta and Kröger, 1995). Under windy conditions, the cross-flow past the perimeter fan is a combination of fan induced cross-flow and wind induced cross-flow, both of which increase the cross-flow velocity past the perimeter fan resulting in perimeter fan inlet flow distortions.

A less predominant wind effect is recirculation of hot air from the heat exchanger outlets referred to as hot plume recirculation (Maulbetsch and DiFilippo, 2008). This is where hot air leaving the ACC is drawn back reducing the effectiveness of the ACC's heat exchangers as a result of the increased air temperature (Kröger, 2004). Under windy conditions, the plume of hot air can be bent over to such an extent that a portion of the warmer air is drawn in by the downwind fans of the ACC (Maulbetsch and DiFilippo, 2008). Maulbetsch and DiFilippo (2008) stated that the effect of plume recirculation is small compared to that of reduction in fan performance for most windy conditions. Owen and Kröger (2010) concluded that a reduction in fan performance is more detrimental to ACC performance at El Dorado power plant in Nevada United States. Reduction in fan performance is therefore considered as the main component resulting in decreasing ACC performance under windy conditions.

In addition to a reduction in fan performance, inlet flow distortions cause a variation in aerodynamic loading on the fan blades because of the maldistribution of air (Muiyser *et al.*, 2016). Maldistribution of air at the fan inlet is caused by the flow separation at the fan inlet shroud (Turner, 1975). The variation in aerodynamic loading is thought to be the main cause for the excessive blade vibration observed in the upwind perimeter fans under windy conditions.

Muiyser *et al.* (2016) did experimental work on the vibration of fan blades that experienced distorted inlet air flow. With an increasing cross-flow component, it was seen that the measured dynamic blade loading on the fan blades increased. It was thought that the cause of the increased dynamic blade loading was due to the periodic excitation caused by the variation in aerodynamic loading on the blade as a result of the inlet flow distortions present.

2.2 Reducing cross-flow effects

Various methods have been investigated to reduce the negative effects that are attributed to cross-flow and associated inlet flow distortions. Some examples of relevant studies are discussed below.

Salta and Kröger (1995), using a scaled model of a fan row, experimentally investigated the effect of a walkway along the perimeter of an ACC platform (refer to Figure 6) and concluded that increasing the width of the walkway improved the volumetric effectiveness of the perimeter fan. They also investigated the effect of increasing the platform height of the fans. This improved the volumetric

performance of the perimeter fans because of the reduction in cross-flow velocity attributed to the increased inflow area. Using their experimental data, they formulated an empirical correlation (Equation 2) for the fan system volumetric effectiveness based on the dimensionless platform height (H/d_f) and the number of fans in the row (n_f)

$$\xi_{sys} = 0.985 - \exp\left[-1 \cdot \left(1 + \frac{45}{n_f}\right) \cdot \left(\frac{H}{6.35 d_f}\right)\right] \quad (2)$$

Duvenhage *et al.* (1996) concluded that the fan inlet shroud is an important feature in an ACC, as experimentation showed that different types of shrouds affected the volumetric effectiveness of the fans under cross-flow conditions.

Bredell *et al.* (2006) used a numerical model of a fan row to predict the effect of lowering the platform height as well as the effect of a walkway, their results being similar to that of Salta and Kröger (1995). Bredell *et al.* (2006) reasoned that the increase in volumetric effectiveness observed in the fan system was a result of a reduction in cross-flow velocity, meaning the abatement of separation and off-axis inflows.

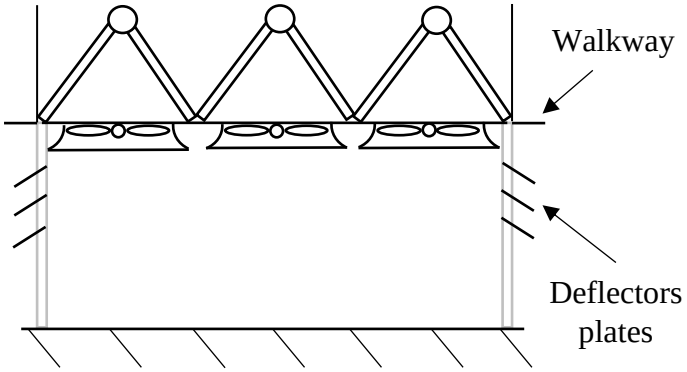

Figure 6: Schematic of an ACC with a walkway and deflectors

There are multiple numerical studies that approximate full-scale ACCs to inspect how the different methods for countering wind effects influence the fan performance of a full-scale ACC. These numerical simulations do however lack rigorous validation procedures as validation of the numerical model is normally achieved by comparing the volumetric flow rates and outlet temperatures from the numerical model for a single unit ACC with that calculated analytically (Van Rooyen, 2007; Louw, 2011; Fourie, 2014).

Van Rooyen (2007) completed a numerical study on the effect of wind on the performance of a 6 × 5 fan unit ACC. Using this model, he investigated the influence that either a walkway or a windscreen in a cross configuration (cruciform) beneath the platform (refer to Figure 7, although for a different ACC configuration), covering the entire area from the ground up, had on the numerical ACC model's

fan performance under windy conditions. His numerical model indicated that the presence of wind had a significant influence on the fan performance of the windward perimeter fan due to the formation of a low-pressure zone at the intake of the perimeter fan, the low-pressure zone is indicative of where separation is occurring. With the addition of a walkway, the performance of the perimeter fans increased due to the displacement of the low-pressure zone upstream. With the windscreen present there was no noticeable changes to the location of the low-pressure zone yet there was a slight increase in the performance of the perimeter fans. Due to the computational intensity involved in solving the entire ACC model only a select few fan units were directly simulated, the results were then used to determine the performance of the remaining fans by means of interpolation.

Gao *et al.* (2010) made use of a numerical model of an ACC under windy conditions to investigate if deflector plates (refer to Figure 6) along the perimeter of the ACC could reduce the negative effects associated with the increase in wind. Their model indicated that having deflector plates along the perimeter improved fan performance under high wind speed conditions as the deflectors guided the flow into the fans, reducing the size of the separation region.

Zhang and Chen (2015) conducted a numerical investigation on an ACC of a 600 MW direct dry-cooled power plant under windy conditions to investigate how the presence of 55% solidity windscreens in various configurations covering approximately 15% of the inlet would affect the ACC's fan and thermal performance. The numerical model indicated that the installation of a perimeter windscreen resulted in improved volumetric effectiveness of all the perimeter fans under windy conditions as the windscreen reduced the size of the low-pressure zone under the intake of the perimeter fans. Their investigation mainly focused on the use of a perimeter windscreen, but they did however make a comparison between different screen configurations, as indicated in Figure 7, based on the ACC thermal performance under windy conditions which indicated that the perimeter windscreen performed best. All 3 windscreen configurations did however improve the ACC thermal performance, compared to a situation where no windscreen was used and increasingly so under higher wind speeds.

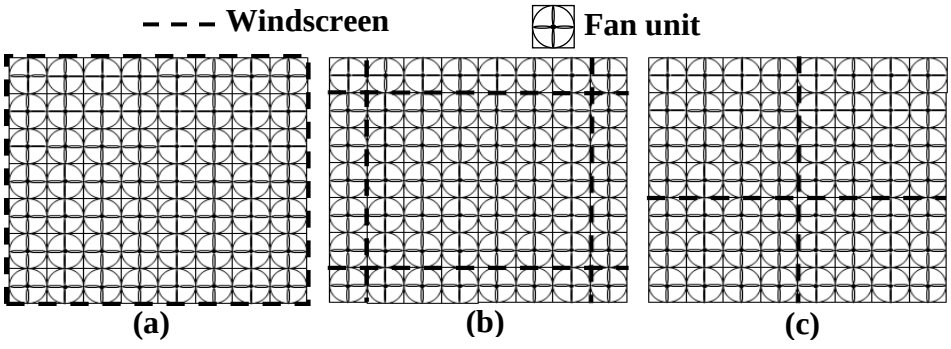

Figure 7: Screen configuration, (a) perimeter windscreen, (b) grid windscreen and (c) cruciform screen (adapted from Zhang and Chen, 2015)

Maulbetsch and DiFilippo (2008) conducted a lengthy experimental investigation into the effect that wind speed and direction have on operational full-scale ACC performance. Some of the ACC facilities inspected in this study were retrofitted with windscreens in an attempt to reduce the negative effects associated with wind. These retrofits appear to be beneficial which inspired a follow-on study specifically aimed at quantifying the improvements associated with the installation of perimeter windscreens.

Maulbetsch and DiFilippo (2016) experimentally investigated the use of perimeter windscreens on a full-scale ACC. In an attempt to quantify the effect of a wind barrier, they did on-site experimentation at Caithness Energy Center which is a 350 MW gas-fired combined cycle plant in New York, USA (Figure 8 shows an aerial view of the facility).

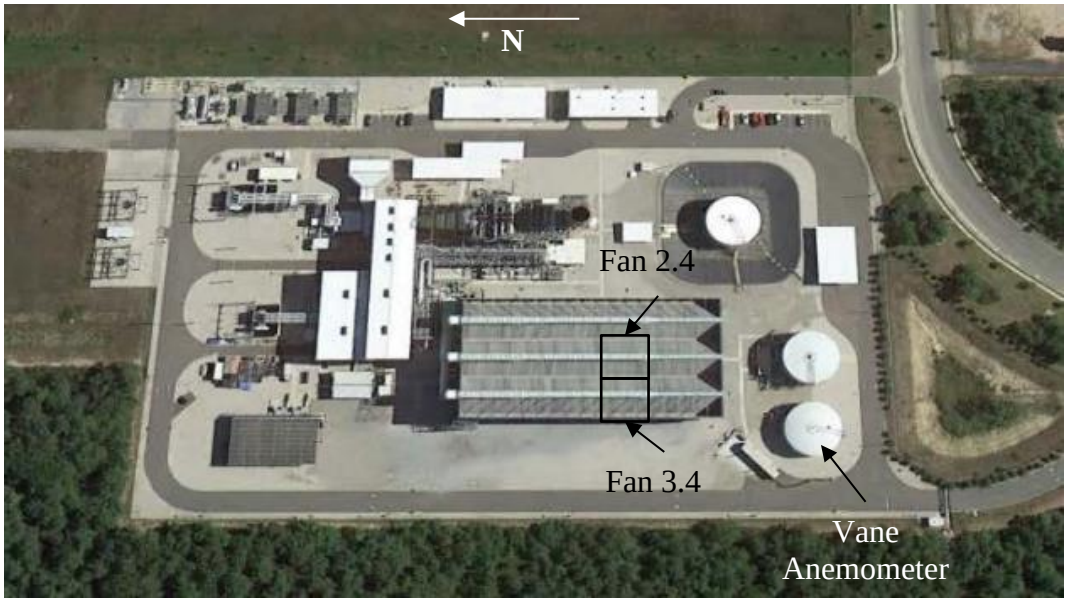

Figure 8: Aerial view of Caithness Energy Center (Maulbetsch and DiFillipo, 2016)

The ACC at Caithness makes use of retractable windscreens (refer to Figure 3) which enabled on-site testing with screens deployed or retracted. By taking multiple velocity measurements at the inlets of fan 3.4 and fan 2.4 (see Figure 9 for fan layout) they could determine the average inflow velocity and compare these with the wind speed, measured away from the ACC at platform height. The wind speed was measured using a vane anemometer situated at the top of a storage tank at the height of the platform. The site layout of Caithness as given in Figure 8, indicates both the positions of fan 3.4 and the position of the vane anemometer that was used to measure the wind speed. While conducting these tests, the wind direction was mainly from a northwest (NW) to southwest (SW) direction meaning the wind was almost perpendicular to fan 3.4 (See Figure 9 for wind directional range).

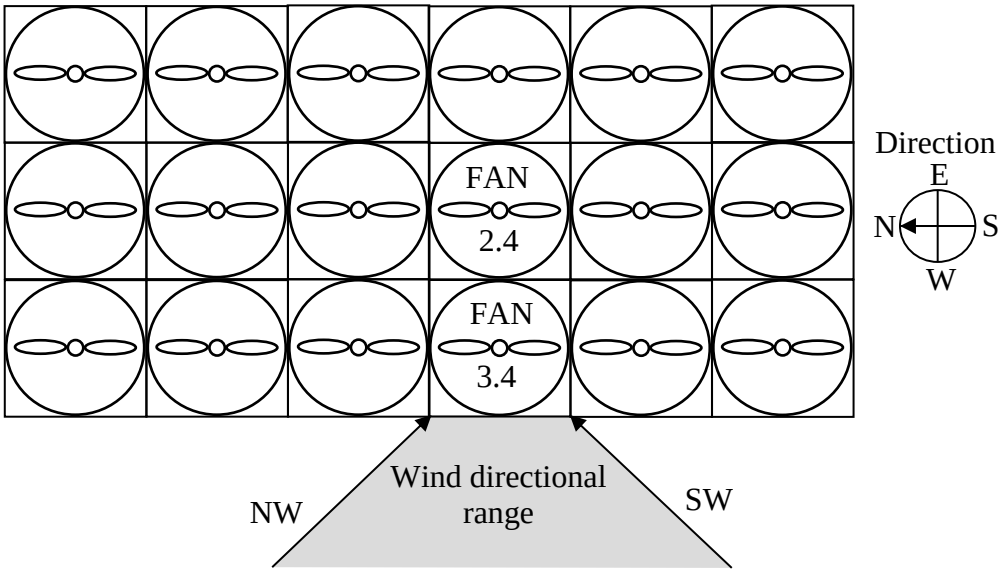

Figure 9: Fan layout and wind directions at the Caithness facility

Maulbetsch and DiFilippo (2016) investigated the effect of different windscreen heights, expressed as a percentage of the total inlet area (upwind) covered by the screen, and how these would affect the average air flow into fans 3.4 and 2.4 compared to when no windscreens were deployed. The recorded data for the average inlet velocity into fan 3.4 and 2.4 at different wind speeds, measured on the storage tank (as indicated in Figure 8) are shown in Figure 10 and Figure 11.

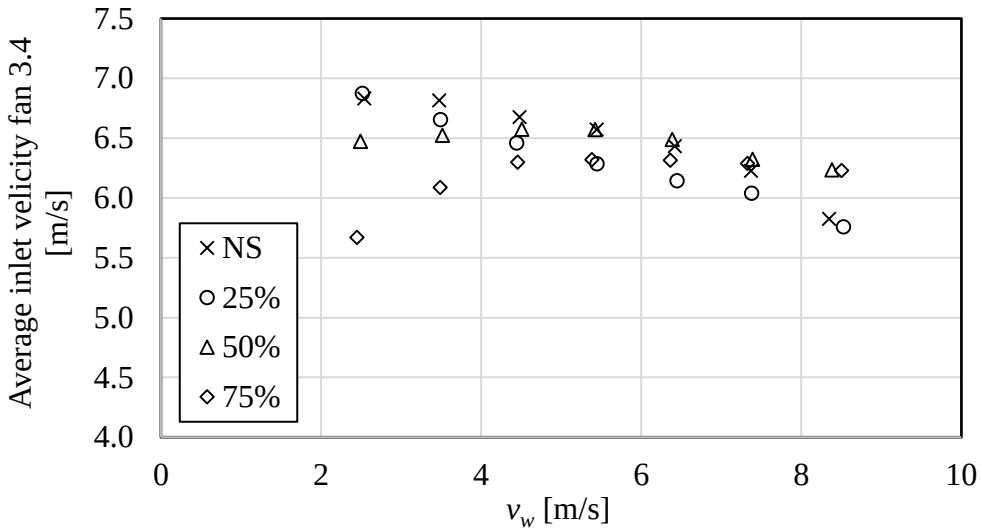

Figure 10: Average inlet velocity into fan 3.4 (Maulbetsch and DiFillipo, 2016)

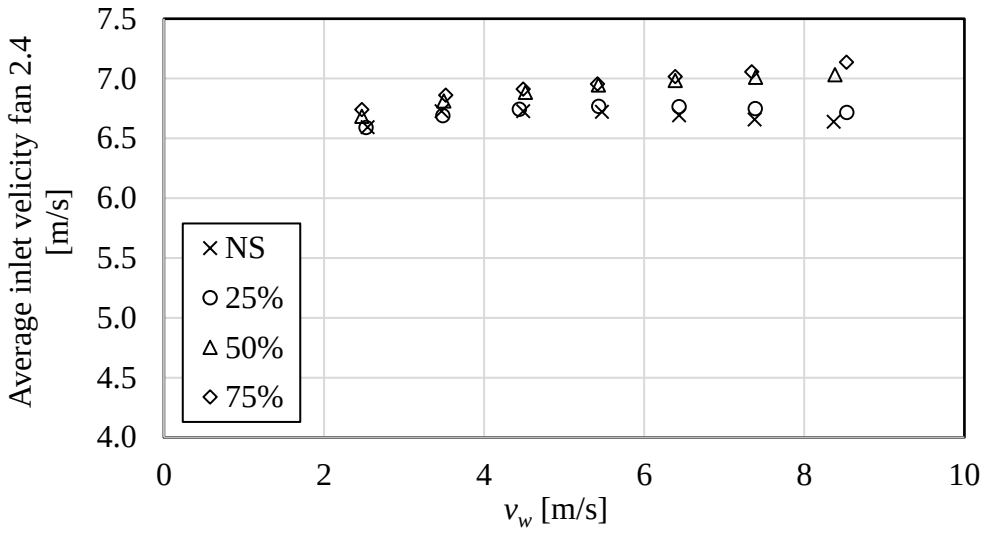

Figure 11: Average inlet velocity into fan 2.4 (Maulbetsch and DiFillipo, 2016)

Figure 10 and Figure 11 illustrate that the perimeter fan performance (fan 3.4), in terms of average inlet velocity, does not experience a performance increase, in fact, it is mostly hindered by the presence of the windscreen. The second fan (fan 2.4) does however experience a performance increase. These experimental findings contradict that which was found in the CFD study done by Zhang and Chen (2015), which indicated that the presence of a windscreen would lead to an increase in the performance of the perimeter fans.

In addition to measuring the inlet velocities at fan 3.4 and 2.4, Maulbetsch and DiFilippo (2016) measured the dynamic loading experienced by 7 of the 9 blades of fan 3.4 using load cells. These results indicated that the deployment of screens resulted in a significant reduction in the dynamic blade loading under windy conditions. Based on the concurrent velocity measurements of the inflow area they could conclude that the screens created a more uniform inlet velocity profile which leads to a reduction in fan vibration.

There is evidence suggesting that perimeter windscreens may be beneficial to both reducing dynamic blade loading and improving perimeter fan performance however based on available literature regarding this topic the evidence is inconsistent, and the exact influence of perimeter windscreens appears to be not well understood. Studies done on this topic have mostly been either numerical or full-scale experimental tests, where numerical studies lack rigorous validation and full-scale experimental studies are subjected to numerous uncontrollable variables due to the dynamic nature of ambient conditions. Therefore a controllable laboratory investigation would be of great value in the process of enhancing the understanding of how windscreens effect fan performance and dynamic blade loading of the perimeter fans.

3 Multiple fan test facility

3.1 Original multiple fan test facility

The multiple fan test facility shown in Figure 12 was designed by Visser (1990) to simulate the axial fan performance of an ACC. Due to physical and practical constraints, the design only consisted of a single fan row. Visser argued that simulating an internal ACC fan row, the incoming flow can be approximated as two dimensional as no flow would cross over between two adjacent fan rows. Based on this assumption he modeled a single fan row with periodic boundaries on either side of the inlet chamber (see Figure 12). The original design was based on an ACC consisting of 48 fans in an 8 × 6 fan configuration situated adjacent to the turbine, therefore the original test facility consisted of 6 fan unit test sections with the inlet chamber having a fixed back wall as to simulate the turbine hall. Each fan test section conformed to the BS 848 type B fan test standard (the ISO version of this standard is the ISO 5801 type B) for a free-inlet ducted outlet fan performance test (ISO, 2007). The facility was also fitted with an adjustable floorboard making it possible to adjust the size of the inlet chamber to simulate different platform heights.

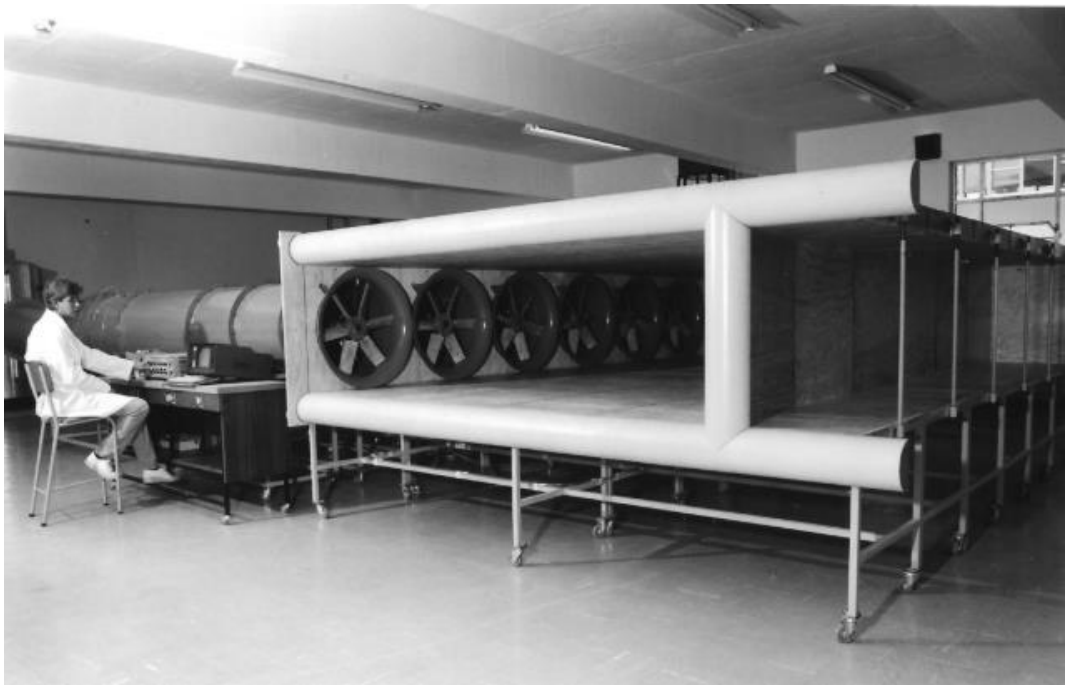

Figure 12: Original multiple fan test facility as used by Visser (Visser 1990)

This original facility was later used by Salta and Kröger (1995) to investigate the effect that inlet flow distortions have on the fan performance. This was done by varying the platform height and the number of simulated fans (by removing fan test

sections) to alter the induced cross-flow at the perimeter fan. They argued that 6 fans with a fixed back wall effectively simulated a fan row of 12 fans in a free-standing ACC (away from the turbine hall) as the back wall essentially acted as a symmetry plane. Based on their results they formulated an empirical correlation to predict fan performance based on platform height and number of fans within the fan row (Equation 2).

Conradie (2010) modified the original facility by reducing the number of fan test sections to 3, with the back-symmetry plane, so the facility now modeled only a 6 unit fan row. This setup is typical of ACC plants in South Africa. He also made multiple upgrades to the old facility including new measurement equipment and upgraded electric motors fitted with a variable speed drive (VSD). The facility was further modified by replacing the 8-vane "Etoile" flow straighteners as specified in the BS 848 standard with a plenum chamber fitted with a porous mesh sheet (hex-core mesh), to enable a more realistic comparison with full-scale ACCs (van der Spuy, 2011).

This updated version of the facility was used by van der Spuy (2011) to gather experimental data on perimeter fan performance and inlet velocity profiles for different types of fans under distorted inlet conditions. This data was used to compare different CFD methods for modeling axial fans in order to determine which method predicts the fan performance the most accurately under distorted inlet conditions. van der Spuy (2011) used particle image velocimetry (PIV) to experimentally measure the velocity profiles at the inlet of the perimeter fan for comparison with CFD generated results. Figure 13 shows a schematic of the multiple fan test facility as used by van der Spuy (2011).

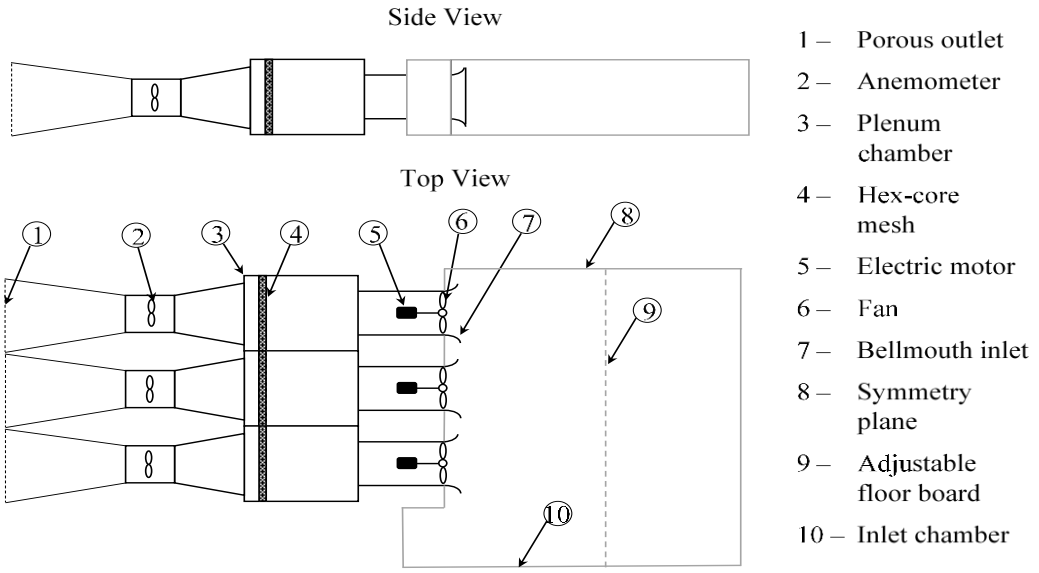

Figure 13: Schematic of the multiple fan test facility (Adapted from van der Spuy (2011))

Fourie (2014) used the facility to investigate the performance of different types of fans under distorted inlet flow conditions. He used hot-wire anemometry to obtain velocity vectors of the flow near the inlet of the perimeter fan. These velocity vectors were used to draw a comparison between the multiple fan test facility and a full-scale numerical ACC model subjected to crosswind. To account for the dimensional difference between the test facility and full-scale CFD results, Fourie (2014) nondimensionalised the velocity vector with the fan blade tip speed (v_{tip}) and by doing so, achieved a good correlation between the two.

Muiyser *et al.* (2016) use the facility to experimentally investigate the effect that increasing inlet flow distortions have on the dynamic blade loading experienced by a single blade of the perimeter fan. The blade loading was measured using strain gauges in a full-bridge configuration, in order to measure the bending strain experienced by the blade. Measurements were recorded at a fan speed of 930 rpm which corresponds to a frequency of approximately half that of the blade natural frequency so as to excite the blade at a harmonics of it's natural frequency.

For this study the same concept of modeling a fan row with three consecutive fan test sections was incorporated, with the difference being that the cross-flow component was generated by an external source to simulate a controllable wind at a fixed fan platform height.

3.2 Multiple fan facility modifications

To investigate the effect that windscreens have on the fan performance of an ACC fan row as well as the dynamic blade loading of the perimeter fan it was necessary to simulate windy conditions to recreate the inlet flow distortions associated with wind. It was resolved to achieve this by modifying the multiple fan test facility to have a fixed platform height and ducting a controllable cross-flow past the scaled fan row to simulate wind. Such a modification would allow for comparison to full-scale test data at a specific ACC. Maulbetsch and DiFilippo's (2016) experimental study of windscreen effects at Caithness Energy Center's ACC provides an opportunity to verify the experimental results against full-scale tests and provide/gain additional insight through a comparison of the two studies. The multiple fan facility was thus modified to achieve geometrical and dynamic similarity with the Caithness ACC.

3.2.1 Similarity to Caithness Energy Center

In this case, geometrical similarity was achieved by matching the dimensionless platform heights (H/d_f), where Caithness Energy Center's ACC has a dimensionless platform height of $H/d_f = 1.32$. Dynamic similarity can be achieved by matching the Reynolds numbers for the fans as well as that of the inlet area. The Reynolds number for the fan is given by Equation 3 and for the inlet area by Equation 4.

$$Re_F = \frac{\rho v_t d_f}{\mu} \tag{3}$$

$$Re_I = \frac{\rho v_x D_H}{\mu} \tag{4}$$

where v_t is the blade tip speed, v_x is the average cross-flow velocity beneath the platform, d_f is the fan diameter and D_H is the hydraulic diameter of the ACC inlet (below the fan platform).

On this scale achieving dynamic similarity is practically impossible as this would require the fans to run at 25 000 rpm and would need to be subjected to an average cross-flow velocity of $v_{xs} = 16.8v_{xf}$ (where the subscript *s* refers to scaled and *f* to full-scale). Although it is impossible to achieve dynamic similarity between the full-scale facility and the scaled model a comparison can still be made as the two are geometrically similar although this comparison would be subjected to discrepancies. To account for these discrepancies the comparison was done based on a nondimensional parameter namely fan volumetric effectiveness, as given by Equation 1, at a normalized wind speed where the wind speed was normalized with respect to the fan blade tip speed (v_{tip}), as used by Fourie (2014).

The availability of full-scale data with windscreens deployed, made it possible to compare this data to that recorded in the scaled facility. The windscreens that were used in the scaled facility are typical industrial windscreen and these are the actual windscreens being used at full-scale facilities such as Caithness Energy Center. For the studies purpose 3 different solidity screens namely: M50, M60, and M75 were used (shown in Figure 14), were the numeric indicates the solidity of the screen (α_{ws}) as defined by Equation 5.

$$\alpha_{ws} = (d_{ws}/P_{ws})^2 \tag{5}$$

where d_{ws} is the diameter of the mesh wires and P_{ws} is the dimension of the square openings.

Again, in order to make a valid comparison between the windscreens used in a full-scale setting to that of the scaled model the two had to exhibit geometrical and dynamical similarity. To achieve geometrical similarity, the ratio between the rectangular dimensions of the openings and the fan blade diameter (P_{ws}/d_f) should be similar. As this is the exact same windscreen that is used in a full-scale setting this was not possible and would have required the openings dimension to be $P_{ws} = 2\times10^{-4}$ m and the mesh wires diameter should have been $d_{ws} = 5\times10^{-5}$ m which is practically impossible.

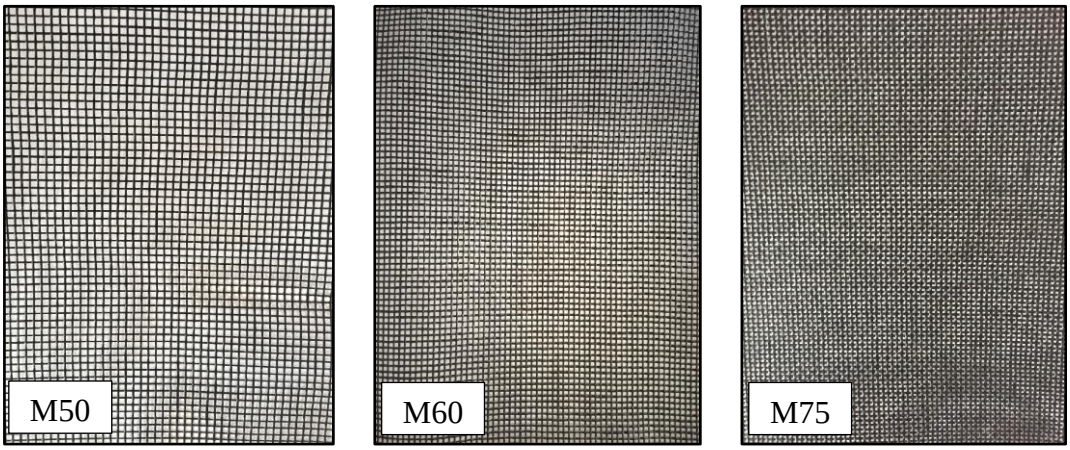

Figure 14: Different solidity windscreens

Dynamic similarity can be achieved when the screen Reynolds numbers are similar. The screen Reynolds number is defined by Equation 6.

$$Re_s = \frac{\rho v_x d_s}{\alpha_s \mu} \tag{6}$$

In this case, dynamic similarity was achieved because similar cross-flow velocities were expected in the scaled facility as were measured at the full-scale facility and because exactly the same windscreens were used the Reynolds numbers would be similar. This indicates that the turbulence caused by the windscreen's mesh wires and square opening would have been similar in magnitude for both the scaled facility and the full-scale facility had it not been for the significant difference in the magnitude of the turbulence of the incoming flow.

3.2.2 Controllable cross-flow

To allow for the required externally generated cross-flow the multiple fan test facility, as described in Section 3.1 was modified to have a fixed platform height (based on Caithness Energy Center's ACC) and an open outlet allowing for free flow across the fan row, as shown in Figure 15.

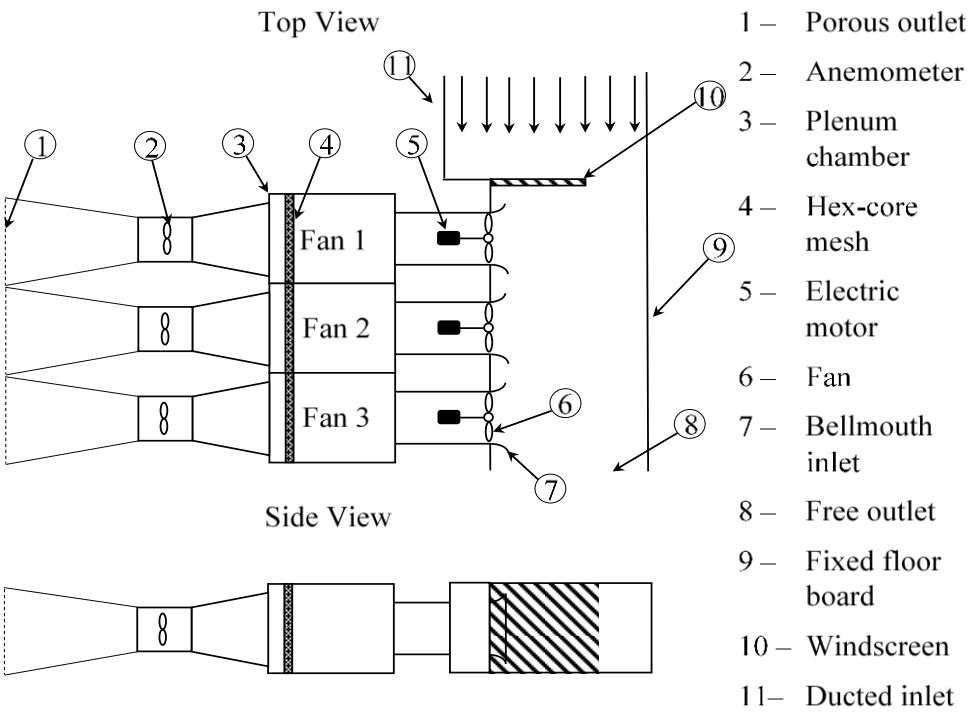

Figure 15: Modified multiple fan test facility's layout

To create the controllable cross-flow velocity an open circuit low-speed wind tunnel, as shown in Figure 16, was used as the flow after the settling chamber had a very uniform velocity profile (see Figure D.7 in Appendix D.6 for the velocity profile of the wind tunnel's test section). The open circuit low-speed wind tunnel has a centrifugal blower that is powered by a 22 kW electric motor and controlled by Yaskawa Varispeed E7 variable speed drive.

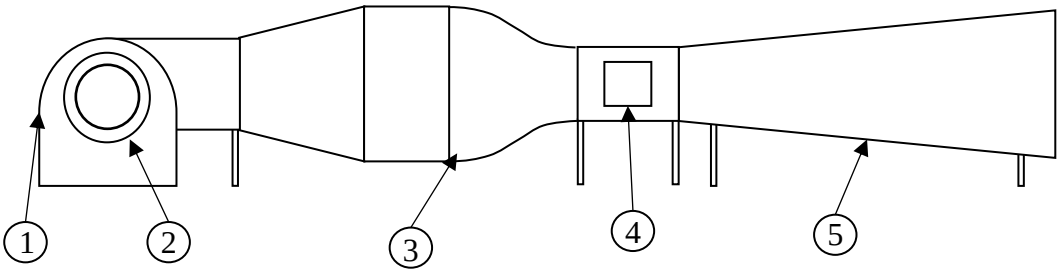

1. Centrifugal blower
2. Air inlet
3. Settling chamber
4. Test section
5. Diffusing outlet

Figure 16: Open loop low-speed wind tunnel

The effect of the volumetric flow from the open loop wind tunnel on the total volumetric effectiveness of the fan row (ξ_{sys}) can be determined by manipulating Equation 2 (that gives a correlation for fan volumetric effectiveness at a certain platform height) into Equation 7 (refer to Appendix B.1 for derivation).

$$V_c = V_{IDsys} \cdot \xi_{sys} \cdot \left[6.35 \cdot Ln\left[0.985 - \xi_{sys}\right] \cdot \left(\frac{n_f}{n_f+45}\right)\right]^{-1} \cdot \frac{H}{d_f} \quad (7)$$

where V_c is the required volumetric cross-flow, ξ_{sys} is the system volumetric effectiveness, V_{IDsys} is the ideal system fan flow rate (results from previous studies can be used for this parameter) and H/d_f is the dimensionless platform height of the new facility.

At the maximum volumetric flow rate of the open loop wind tunnel, which is 8.5 m^3/s, the volumetric effectiveness of the modified test facility would approximately be $\xi_{sys} = 0.65$ for a $H/d_f = 1.32$ and $V_{IDsys} = 4.3$ m^3/s (as measured by Fourie (2014)). This is worse than that which was achieved by changing the platform height, where a system volumetric effectiveness within the range of $0.7 \leq \xi_{sys} \leq 0.75$ was recorded (van der Spuy, 2011). This is because the open loop wind tunnel can generate a higher cross-flow velocity compared to that achievable by simply changing the platform height. Figure 17 shows the predicted operational range of the modified facility according to Equation 7.

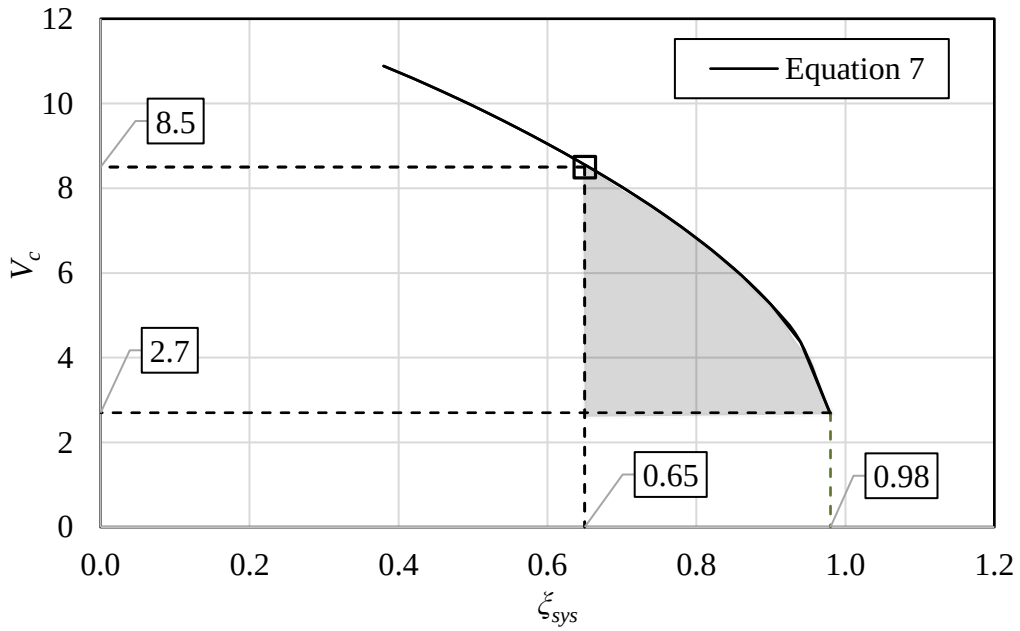

Figure 17: Modified test facility operation range

3.2.3 Duct height selection

The flow capacity of the low-speed wind tunnel and laboratory layout were ideally suited for the updated version of the multiple fan test facility, but this required flow from the outlet of the low-speed wind tunnel to be ducted to the inlet chamber of the modified multiple fan test facility. The dimensions of the open loop wind tunnel's outlet are 610 × 1205 mm (w × h), and as a result the ducting had to diffuse horizontally and contract vertically to interface with the test section's inlet chamber (830 × 800 mm). To simplify manufacturing and to allow for easy disconnection to facilitate installation or removal of windscreens the ducting was split into two sections: a diffusing section and a straightening section as shown in Figure 18. The windscreens were installed at the intersection of the inlet chamber and the straightening section's flanges as this is the edge of the fan platform which is where perimeter windscreens are installed in practice. The screen was fastened onto the inlet chamber's flange using Velcro and locating pins and then clamped in place when the straightening section was attached.

Both the inlet chamber and the straightening section were fitted with Perspex windows, as shown in Figure 18, to enable velocity field visualizations which are discussed in Section 4.3.

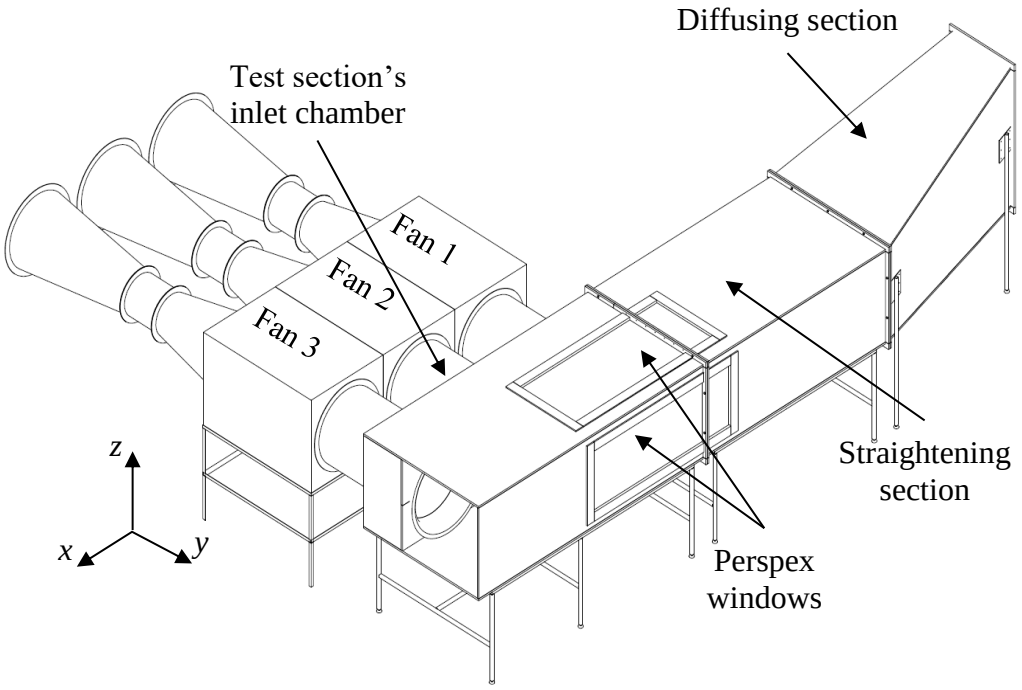

Figure 18: Schematic of the updated multiple fan test facility

To ensure that the ducted-inlet still accurately represented the free-inlet of a real ACC subjected to crosswind, the height of the inlet duct had to be determined and optimized to prevent or reduce differences between the two cases. To achieve this,

the inlet duct's height was designed to correspond with the height (from the ground up) at which a strong cross-flow diverges along the wind-wall of a free-inlet ACC fan row, as depicted in Figure 19.

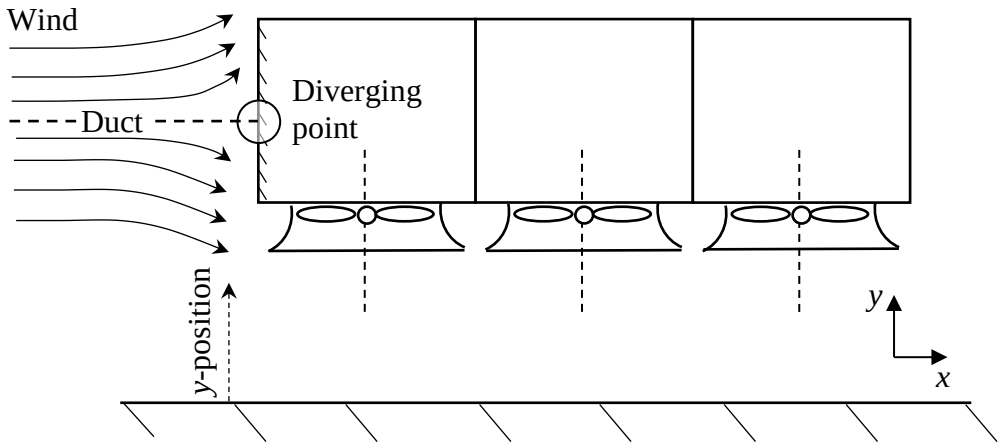

Figure 19: Free-inlet ACC fan row

To determine this height a two-dimensional CFD model of a fan row consisting of three fans modeled on the scale of the multiple fan test facility was used. The geometry of the model was similar to that shown in Figure 19. The fans were modeled as one-dimensional pressure-jump boundary conditions while the system resistance was modeled as a one-dimensional porous-jump boundary condition (Fluent, 2017). More detail on the CFD model is given in Appendix C.1.

The diverging point along the wind-wall was determined by comparing the *y*-velocity component of the incoming wind along the *y*-position line (as indicated in Figure 19) as shown in Figure 20. This was repeated for inlet wind speeds ranging from 0 m/s to 9 m/s. The position where the *y*-velocity underwent a sign change from negative to positive indicated the diverging point.

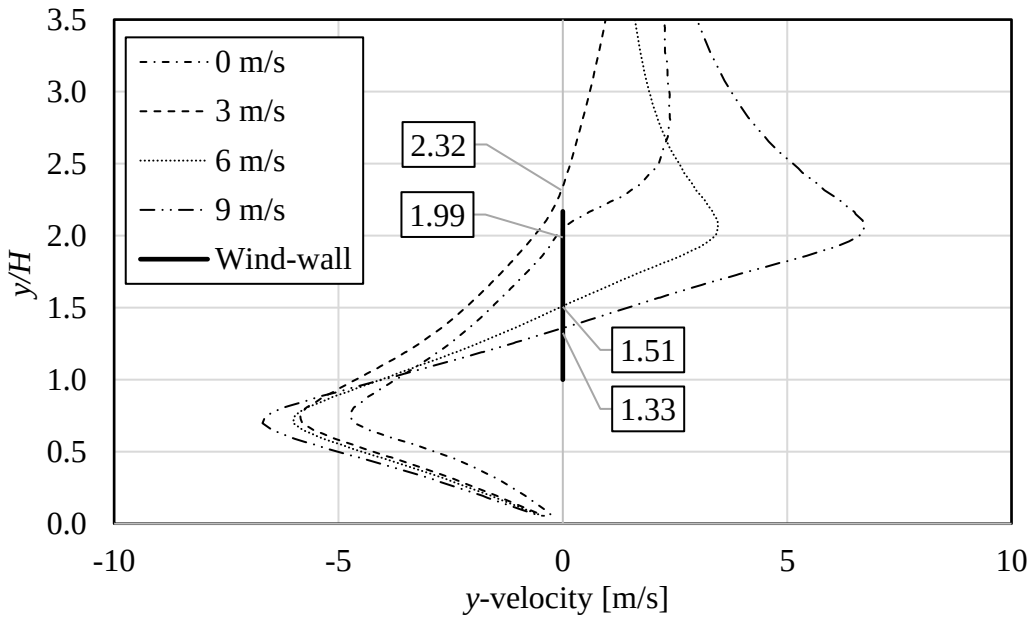

Figure 20: *y*-velocity along *y*-position line

As seen from Figure 20 the point of divergence shifted downward as the inlet wind speed was increased. Due to this phenomenon selecting a fixed duct height would cause discrepancies between the free-inlet and ducted-inlet cases over a range of wind speeds. An initial duct height of H/d_f = 1.51 was selected to inspect how having a fixed ducted-inlet would affect the two-dimensional CFD simulation compared to that of the free-inlet simulation. This value for the duct height was based on the height at which the incoming flow separated along the wind-wall for an inlet velocity boundary condition of 6 m/s. This duct height was a compromise between high and low cross-flow scenarios. The comparison between the free-inlet simulation and the fixed ducted-inlet simulation was done based on the *x*-velocity profiles along the *y*-position line as shown in Figure 21. The results are shown in Figure 22.

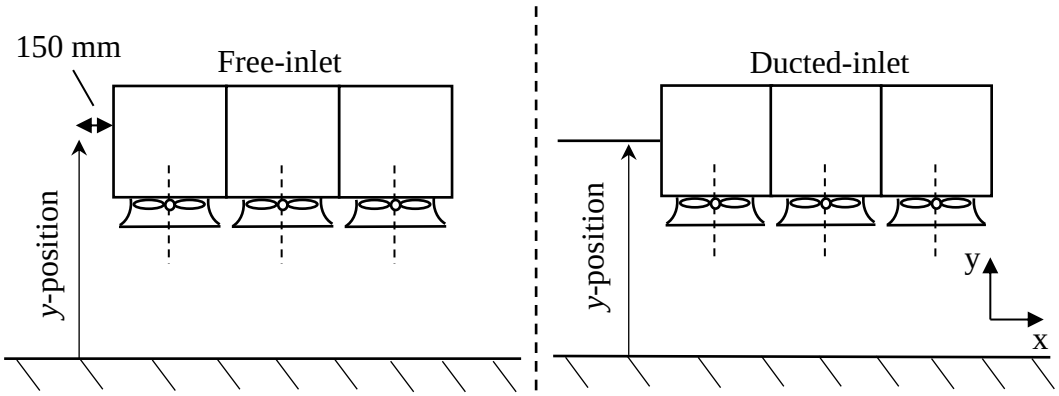

Figure 21: Free-inlet and ducted-inlet

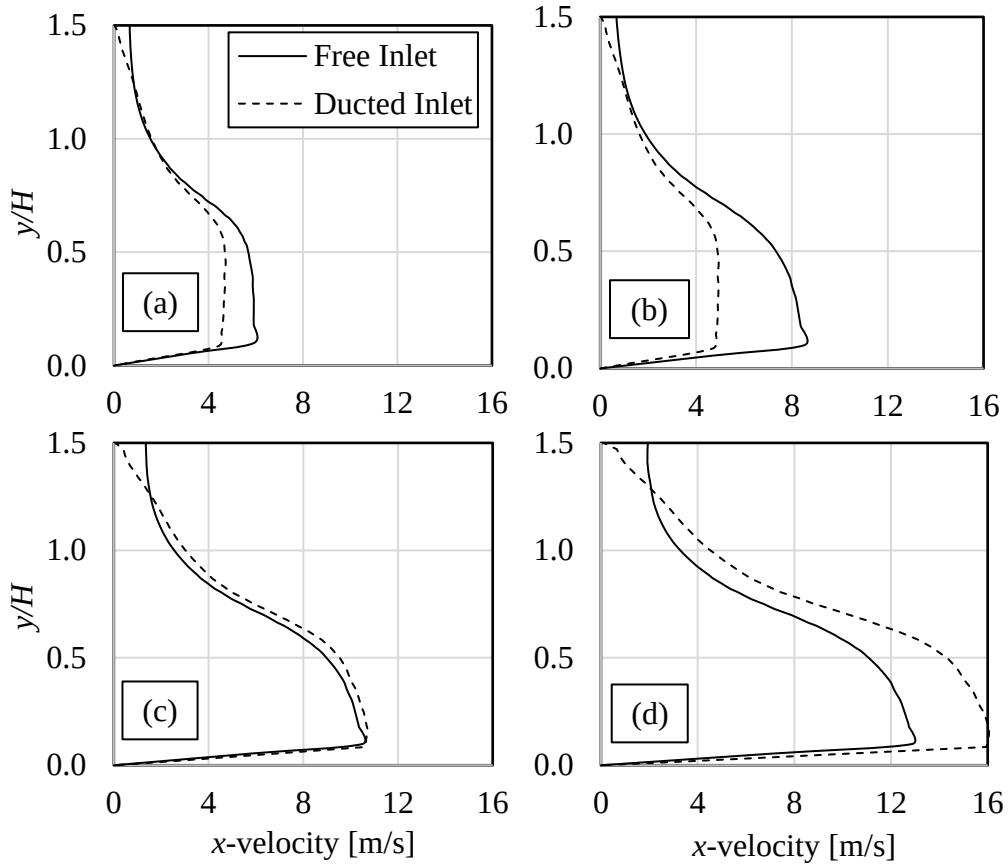

Figure 22: *x*-velocity along the *y*-position line of inlet wind speeds of (a) 0 m/s, (b) 3 m/s, (c) 6 m/s and (d) 9 m/s

At an inlet boundary condition of 6 m/s, as shown in Figure 22 (c), the two models have a good correlation as the duct height was selected based on that specific inlet velocity condition's point of divergence. But there is discrepancy at different wind speeds (a), (b) and (d) due to the shifting divergence point shown in Figure 20. For the two models to be similar the duct height must be adjusted at each inlet velocity condition to align with the point of divergence for that specific case.

It would be impractical to have separate ducts manufactured for each of the required wind speeds, so an alternative method of comparing the two cases was needed. The cross-flow velocity beneath the fan platform is thought to be the cause for inlet flow distortions, then assuming that similar average cross-flow velocities (v_x) beneath the platform in both the free- and ducted-inlet cases would have the same effect on the perimeter fan's performance and dynamic blade loading, the physical differences between the two cases could be ignored. The assumption of comparing the free-inlet to the ducted-inlet based on average cross-flow velocity can be validated by using CFD modeling or by comparing the total system volumetric

effectiveness at a given average cross-flow velocity, calculated using Equation 7, with test data recorded using the updated facility.

Validation through CFD would require modeling the test facility and free-standing ACC fan row and then comparing fan performance based on the average cross-flow beneath the platform. This was done using the two-dimensional CFD models described above - the result based on the volumetric effectiveness of the perimeter fan (ζ_{f1}) at increasing average cross-flow velocity for both the free-and ducted-inlet is shown in Figure 23.

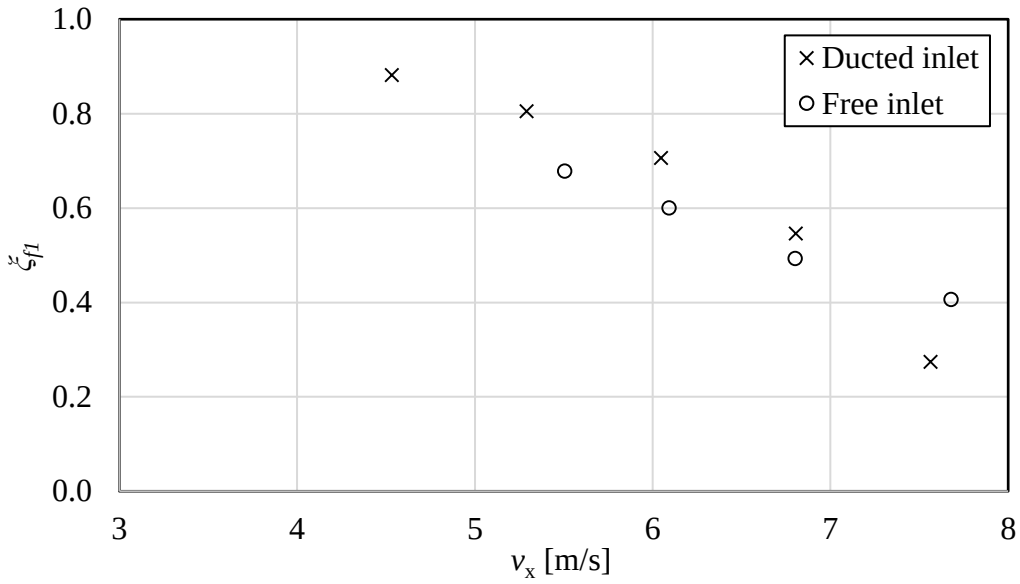

Figure 23: Two-dimensional CFD prediction of volumetric effectiveness for the free-and ducted-inlet

Figure 23 indicates a similarity in the results, although ideally this comparison should be made based on a three-dimensional CFD model with the fan being modeled with an actuator disk model (ADM) as van der Spuy (2011) concluded that the ADM captures inlet flow distortions more accurately. For the purpose of this preliminary validation such a complex CFD analysis is deemed unnecessary. The comparison between test data and Equation 7 is given in section 5.2.2.

Having a fixed ducted-inlet has a definite influence on the incoming flow, but comparing the ducted-inlet to a free-inlet based on the average cross-flow velocity allows for similarity in the magnitude of the inlet flow distortions present at the perimeter fan. The primary aim of the modifications on the facility was to create inlet flow distortions at the perimeter fan using a controllable cross-flow velocity to inspect how the presence of a windscreen would influence the flow and potentially mitigate these inlet flow distortions. As the open loop low-speed wind tunnel could produce this required cross-flow and the simplified CFD validation

indicated similarity between the two cases, there was confidence in the proposed modification.

The final challenge in having a fixed inlet duct is that the average cross-flow velocity measured beneath the platform (v_x) is effectively a combination of induced draft (v_{in}), caused by the fans, and the average simulated wind (v_{wa}) as shown in Figure 24, and expressed in Equation 8. The simulated wind component would therefore be an unknown. This is unfortunate as it makes it difficult to compare the experimental results to that of full-scale results where a comparison is drawn between fan performance and ambient wind speed at platform height.

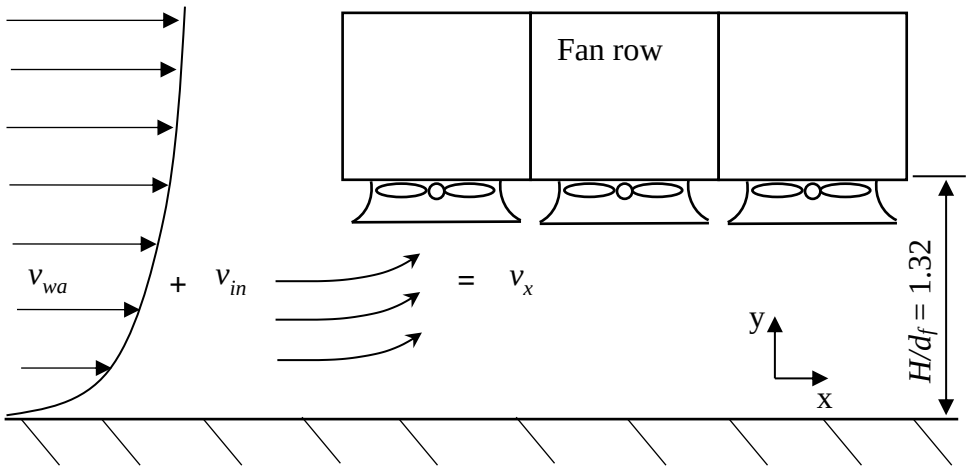

Figure 24: Wind and average cross-flow velocity

The average cross-flow velocity past the windward perimeter fan can be given as the sum of the average wind speed and the average induced draft through the windward inlet area.

$$v_x = v_{wa} + v_{in} \tag{8}$$

where the average wind speed (v_{wa}) can be calculated using Equation 9:

$$v_{wa} = \frac{\int_0^H v_{wp}(y)dy}{H} \tag{9}$$

and where the wind velocity profile is approximated using a power law (Equation 10):

$$v_{wp}(y) = v_w \left(\frac{y}{H}\right)^b \tag{10}$$

where v_{wp}(y) is the horizontal wind speed at a certain height off the ground (y), v_w is the wind speed at platform height (H) and b is based on which power law is used

to define the wind velocity profile, in this study $b = 1/7$ was used as this is regarded as a good representative for neutral ambient conditions (Touma, 1977).

The wind speed at platform height can however be approximated from the experimental data by subtracting the induced draft from the average cross-flow velocity and multiplying this with an integrational constant (see Equation 13 in Section 5.2.2). This approximated wind speed, normalized with respect to fan tip speed, could then be used to compare fan volumetric effectiveness measured at the multiple fan test facility with that recorded at Caithness Energy Center by Maulbetsch and DiFilippo (2016). This comparison would then be based on an approximated wind speed that is derived from the measured average cross-flow velocity and therefor based on the assumption that similar average cross-flow velocities (v_x) will cause the same subsequent effect on the perimeter fan's performance.

The final duct height was kept as $y/d_f = 1.51$ as to include a portion of the wind-wall to capture the associated flow effects and to allow for future installation of a walkway. Although this duct height was initially selected based on the point of divergence of an unverified two-dimensional CFD model, it was kept unchanged based on the assumption that the perimeter fan would perform similarly in both cases at similar average cross-flow velocities (v_x) therefore there was no need to change the duct height.

3.2.4 Duct length selection

Finally, the inlet ducting itself had to be analysed, due to the fact that the shape of the outlet of the small wind tunnel, the connecting duct was required to diffuse horizontally and contract vertically to interface with the test section inlet chamber. The dimension of the wind tunnel's outlet was 610 x 1205 mm ($w \times h$) and the duct had the required dimension of 1250 × 800 mm. As mentioned, the connecting duct comprised of two sections namely a diffusing section and a straightening section that connected the wind tunnels outlet to the inlet chamber of the fan test sections. The reason for dividing the connecting duct into two sections was to allow for easy installation of the windscreens. Due to the connecting duct diffusing the flow, the diffusing angle of the duct had to be optimized to prevent separation along the duct walls and to produce an outlet velocity profile, within the available space, to be as uniform as possible. Having already set the dimensions for the outlet of the straightening duct section, the only way to prevent separation was to increase the lengths of the diffusing and straightening sections.

To prevent separation occurring within a diffuser the angle along which the flow diffuses should be approximately 7º or less (Sparrow et al., 2009) but due to the space limitations within the laboratory, this target angle could not be met as it would require the diffusing section to have a length of 5 m. With the help of a three-dimensional CFD model of the connecting duct, an optimal length for both the diffusing and straightening sections could be determined that would result in a uniform outlet flow within the available space. The model's geometry consisted of

the diffusing section with $10D_H$ up-and downstream to ensure that a fully developed turbulent velocity profile enters the diffusing section and that the outlet boundary condition does not influence flow within the diffusing section. To improve the modeling of separation, the k-ω SST turbulence model was used (Fluent, 2017). More details on the CFD model is given in Appendix C.2. Figure 25 shows the geometry and meshing used for the CFD.

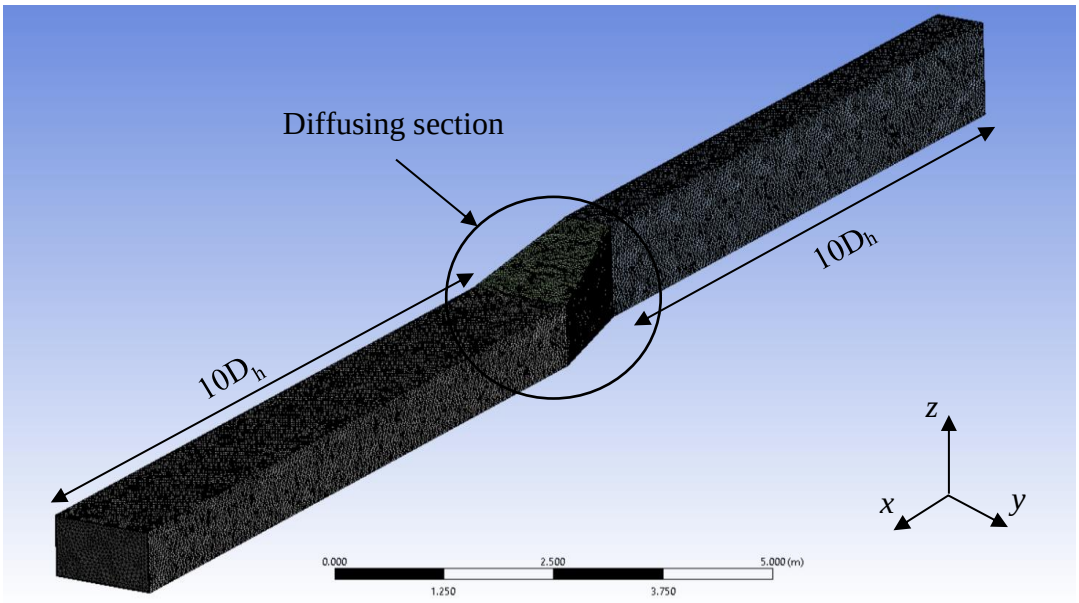

Figure 25: Geometry and mesh of duct sections

Figure 26 compares the area-based uniformity index of the outlet plane of the diffusing section and straightening section to that of $10D_h$ downstream, to visualize the effect of changing the length of the diffusing section. Uniformity index is given by Equation 11, where a perfectly uniform velocity profile would have a uniformity index of $Y = 1$.

$$Y = 1 - \sum_{i=1}^{N} \frac{|v_i - \bar{v}|}{2\bar{v}X} X_i \tag{11}$$

where v_i is the local cell's velocity and $\bar{v}$ is the average velocity through the plane. X_i is the area of the cell and X is the planes cross-sectional area.

From Figure 26 it is seen that increasing the length of the diffusing section results in an increase in the uniformity index due to the diffusing angle being altered. A length of 2 m was selected for the diffusing section as the uniformity index was deemed adequate without requiring an excessively long diffusing section as available space within the laboratory was a problem.

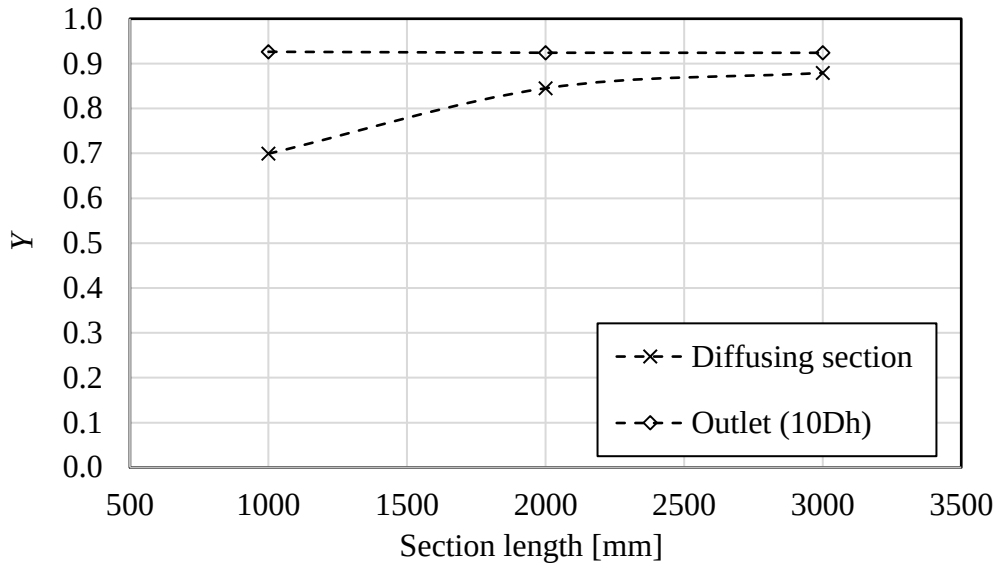

Figure 26: Uniformity index of the diffusing and straightening section

Figure 27 shows the *x*-velocity profile along the center plane of the duct for an inlet velocity of 6 m/s. The figure also depicts the effect of having a straightening section as well as how different straightening section lengths affect the velocity profile.

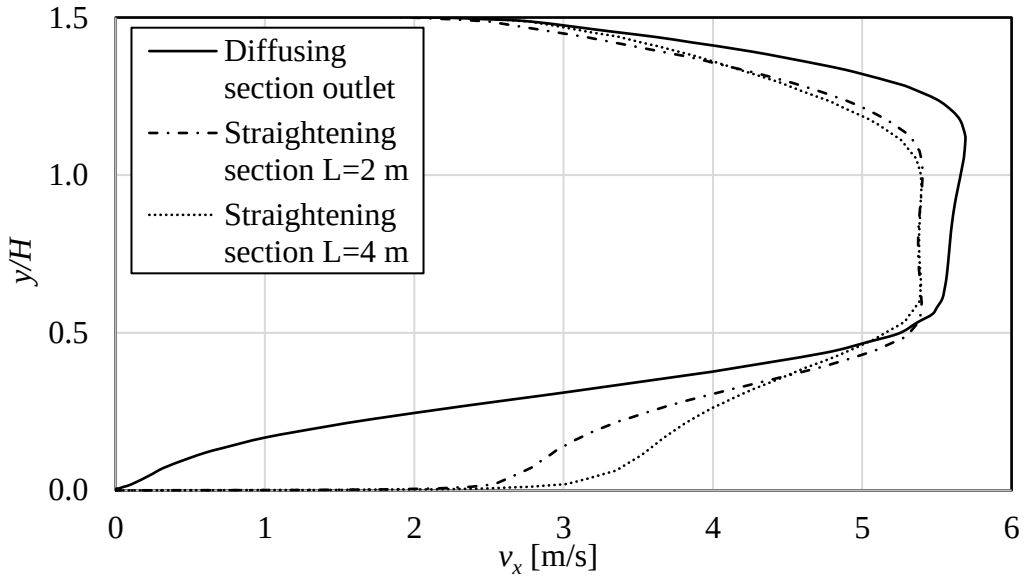

Figure 27: *x*-velocity profile along the center line of the straightening section

The length for the straightening section was selected based on the *x*-velocity profile along the center plane as given in Figure 27. Based on the results shown a length of 2 m was selected for the straightening section as this produced a profile very similar

to that of a 4 m section. The uniformity index of the straightening section's outlet (with a length of 2 m) was unaffected by changing the inlet velocity.

Having fixed the dimensionless platform height for the modified facility and determined all the required dimensions for the inlet duct the original multiple fan test facility had been successfully modified to allow for a controllable cross-flow at a fixed platform height to recreate the inlet distortion associated with windy conditions. Figure 28 shows the newly modified multiple fan test facility.

Figure 28: The modified multiple fan test facility

4 Experimental procedures

4.1 Individual fan performance

Individual fan performance tests were performed on the 630L fan blade which is a scaled model of an industrial application fan. The scaling of the fan was done by Augustyn (2013). The fan performance tests were required to gain confidence in the measuring techniques used in this study, by comparing results to those obtained by Fourie (2014) who performed identical fan tests using the same facility.

The individual fan performance tests were performed on a single test section of the multiple fan test facility without the inlet chamber connected. The fan tests were performed in accordance with ISO 5801 category B (free-inlet and ducted outlet) testing standard (ISO, 2007).

Figure 29 shows the experimental setup for the individual fan tests where the flow rate was measured with a WeatherTronics propeller anemometer, the static pressure was measured after the hex-core mesh (point 3) using an AutoTran Model 860 pressure transducer and fan speed was measured using a magnetic pickup with a frequency to voltage converter. These measurements were logged with a National Instrument data acquisition system (DAQ). The torque was measured with an HBM T5 20 N·M transducer and amplified using an HBM spider-8 bridge amplifier and logged using Catman Easy software. See Appendix A for calibration curves.

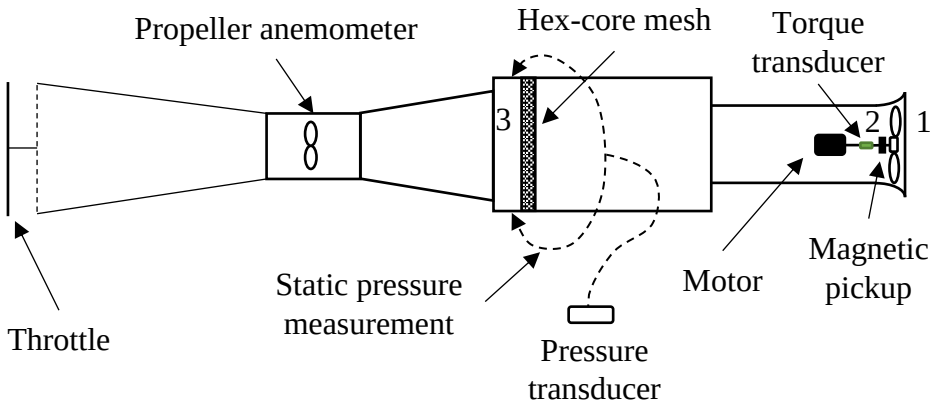

Figure 29: Individual fan performance test

All the performance tests were done at a fan speed of 1000 rpm. The test procedure was as follows: Without the fan blade installed the motor was set to run at operating speed for 10 minutes, torque zero readings were taken before and after, where this torque measurement was used to determine the mechanical losses caused by friction in the bearings. The fan was then installed, and all instrumentations' zero readings

were taken, the motor was set to run at 1000 rpm again and left for 10 minutes. Data was recorded at various flow rates by adjusting the outlet flow throttle, at each throttle position the system was allowed to settle before taking the next measurement. At the end of the test zero values were again recorded.

Because the facility has a free-inlet and ducted-outlet, the static pressure measured at point 3 in Figure 29 is, in fact, the total-to-static pressure rise from the fan inlet (point 1) to after the hex-core mesh (point 3). The total-to-static pressure rise across the fan had to be analytically calculated based on the static pressure measured at point 3, see Appendix B.4 for a sample calculation. All the recorded results were scaled to a density of ρ = 1.2 kg/m^3 using the fan scaling laws, see Appendix B.4 for a sample calculation of the post-processing of the measured data.

After the completion of the fan performance tests, the operating point for each of the 3 fan test sections were individually set by changing the system resistance. This was done by adding to, or removing plugs from the porous outlet, where the porous outlet replaced the throttle at the completion of the fan performance tests (refer to Figure 13). The operating point of the three fan test sections was set to be within 10% of the desired operating point. The selected operating point (Table 1) was the same as that used by Fourie (2014) which is a scaled version of the design point used by Bruneau (1994). Each of the test sections operating points' volumetric flow rate was considered as the ideal volumetric flow rate as the flow would have been axially aligned and not subjected to inlet flow distortions.

Table 1: Fan operating point

Static pressure [Pa]	Volumetric flow rate [m^3/s]
62.3	1.455

4.2 Multiple fan performance

This section will discuss tests procedures for the following three tests: Free-inlet, ducted-inlet and multiple fan performance test under increasing cross-flow. Free-inlet and ducted-inlet tests were required in the setup procedure of the final multiple fan performance tests under increasing cross-flow.

4.2.1 Free-inlet

As mentioned in Section 3.2.2, outlet flow from an open loop low-speed wind tunnel provides the cross-flow component at the fan inlet chamber. But because this flow is ducted to the inlet of the fan row it was required to experimentally measure and limit the effect of the ducted-inlet upon the performance of the system, as it caused the system to perform unsymmetrically because of the added flow resistance at the windward inlet. As such the performance of the fan row with a free-inlet had to be determined, as this was the baseline of comparison with the ducted-inlet

performance. The free-inlet performance test was done by measuring the volumetric flow rate through each of the 3 fan test sections with the inlet chamber attached.

A pitot tube traverse of the windward inlet was also done along the center plane of the inlet chamber, as shown in Figure 30, to obtain the inlet velocity profiles. The velocity profile was determined by taking 18 pressure differential measurements, with the pitot tube, along the center plane of the inlet from platform height to the floorboard. An Endress and Hauser Deltabar S pressure transducer was used to measure the differential pressure across the pitot tube probes, the data was recorded on the DAQ. See Appendix A.3 for the calibration curve. Figure 30 indicates where the pitot tube traverse was done with reference to the perimeter fan, note that the traverse was done along the center plane.

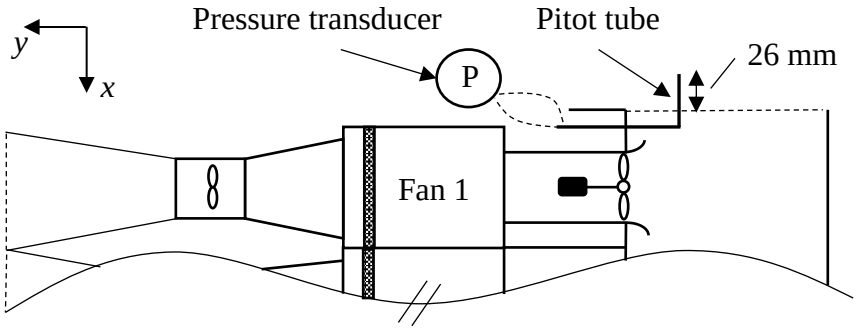

Figure 30: Pitot tube traverse at the inlet of fan 1

4.2.2 Ducted-inlet

As mentioned, attaching the inlet duct causes an additional flow resistance and to overcome this resistance the low-speed wind tunnel was to deliver an auxiliary flow rate enabling the system to perform similarly to the free-inlet case. The ducting was installed to allow the outlet flow from the wind tunnel to be blown past the fan row where the auxiliary flow rate required was determined by adjusting the supply from the wind tunnel and monitoring the fan performance of each of the 3 test sections, in terms of volumetric flow rate. This was done until the fan performance was similar to that of the free-inlet case, the auxiliary flow rate at this point was approximately half the volume flow rate delivered by the 3 fans under the free-inlet case. This was defined as the no-wind scenario as the performance of the fans at the free-inlet case represents a fan row functioning with no cross-flow other than that induced by its own fans.

The auxiliary flow rate provided by the low-speed wind tunnel was determined by measuring the velocity at the center of the wind tunnel's test section (refer to Figure 16), using a pitot tube, and multiplying with the test section area (under the assumption of incompressible flow). This method was validated by measuring the velocity profile of the wind tunnel test section at the no-wind scenario by means of

pitot tube traverses (in both the *x*- and *y*-directions), as the no-wind scenario required the lowest auxiliary flow rate meaning that if the measured velocity profiles were turbulent they would stay fully turbulent across the entire spectrum in which the tests was required to be performed. The velocity measurements were constant along the *x*- and *y*- directions, thus the flow could be assumed to be fully turbulent as the boundary layer was too small to measure with the pitot tube and the profile was essentially uniform. As a result, this method of using a single point velocity measurement for calculating the volume flow rate was deemed accurate. See Appendix D.5 for the velocity profile of the wind tunnel's test section at no-wind volume flow rate.

The pressure difference between the total and static pressure measured by the pitot tube in the low-speed wind tunnels test section was recorded with an Endress and Hauser Deltabar S pressure transducer and logged with the DAQ. See Appendix A.3 for the calibration curve.

A pitot tube traverse was also performed on the windward inlet, a similar process as described for the free-inlet case to compare the inlet velocity profile of the ducted-inlet case to that of the free-inlet case.

4.2.3 Multiple fan performance under cross-flow

The test conducted in this experiment was used to determine the effect that a strong cross-flow has on the performance of the fans in terms of volumetric effectiveness, fan power consumption, and dynamic blade loading. This test was performed without a windscreen installed and subsequently repeated with the installation of the 3 different solidity windscreens (M50, M60, and M75) at 3 different percentage inlet area covered (windward side) (25%, 50% and 75%). Each of the 10 tests was repeated a minimum of 3 times to determine the repeatability and standard deviation between the tests.

The volume flow rate through each of the 3 fan test sections was measured to determine the volumetric effectiveness of each of the fans under the increasing cross-flow. The dynamic blade loading and fan torque were measured exclusively on the perimeter fan (windward side).

The dynamic blade loading was characterized by measuring the bending strain experienced by the blade, this is the same technique used by Muiyser *et al.* (2016). The bending strain was measured using four HBM 350Ω strain gauges configured in full Wheatstone bridge configuration. The strain gauges were stuck onto the blade using cyanoacrylate glue and were connected to a MicroStrain SG-link LSXR wireless bridge amplifier. The Sensorconnect software package, developed by Microstrain, was used to record the strain measurements. Figure 31 shows two of the strain gauges attached to the blade and connected to the SG-link, the latter being attached to the hub with a bracket and a counterweight attached on the opposite side of the hub for balancing. This bracket attaching the SG-link and the counterweight

did not have any influence on the perimeter fan's performance in terms of volumetric effectiveness.

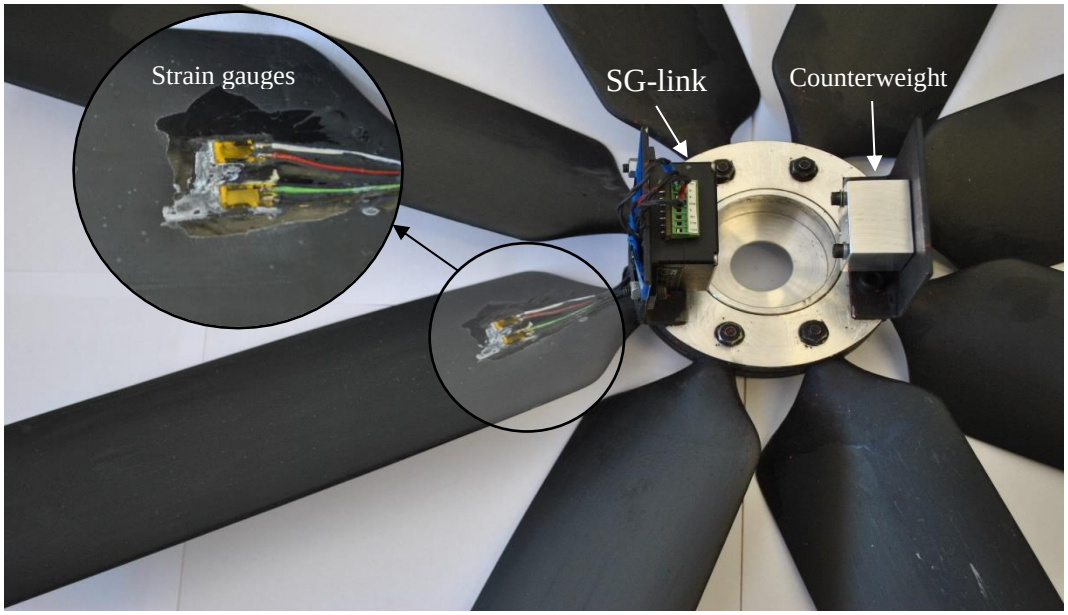

Figure 31: Perimeter fan blade strain measurement

The test procedure for each of the sets was as follows: zero values of the torque transducer and pressure transducers were recorded, thereafter the low-speed tunnel was set to the "no-wind' volume flow rate determined as per section 4.2.2. The fans were set to 1000 rpm and the system was given 5 minutes to stabilize, whereafter the data was recorded for 5 minutes to reduce the significance of the transient's effects in the flow. Upon completion, the cross-flow rate was incrementally increased, and the flow was given 2.5 minutes to stabilize before recording the next measurements, this was repeated for a total of 9 measurements each at different cross-flow rates. At the end of the test zero values were again measured. Each test was repeated a minimum of 3 times to quantify the standard deviation between the measurements.

4.3 Particle imagery velocimetry (PIV)

An important part of the study was to experimentally visualize the flow field around the inlet of the perimeter fan with and without a windscreen installed. This was achieved by making use of particle image velocimetry (PIV) which is a method used to measure the velocity vector within the flow field. This is done by spraying fine mineral oil particles into the flow far away from the region of interest in order for the particles to be distributed throughout the flow. At the region of interest, the oil particles are illuminated by a laser beam and multiple images are subsequently, using a high-speed camera, are subsequently captured of the illuminated particles moving across the image frame. See Figure 32 for the experimental setup.

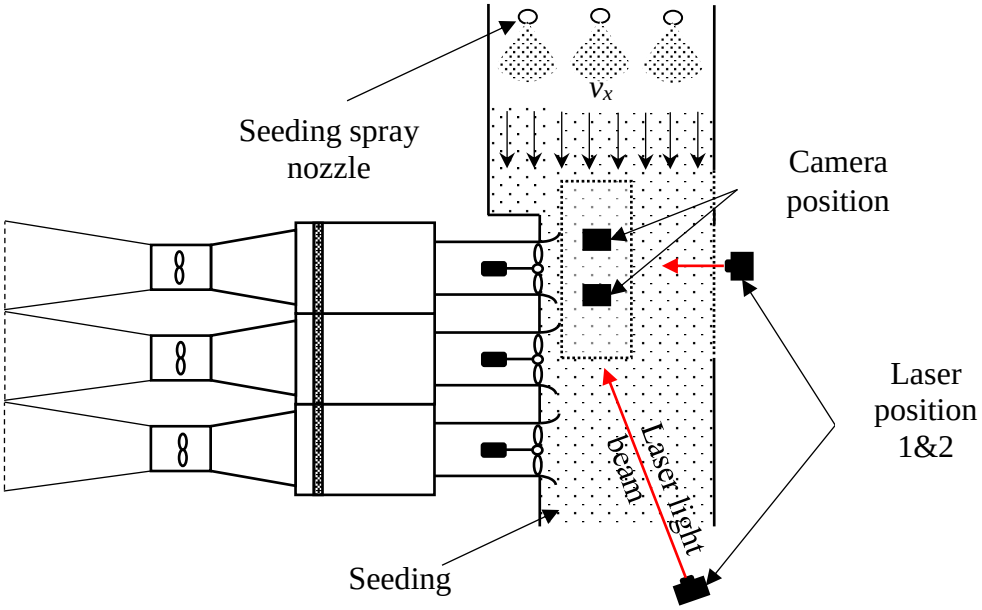

Figure 32: PIV experimental setup

Only a two-dimensional flow field was required and thus the two available cameras could be used in the same plane to capture a wider region. The PIV setup included Nikon 60 mm lenses, with a narrow angle of view and to capture the required flow field the cameras had to be placed far away from the region of interest and multiple image sets had to be taken along the plane of the region of interest and stitched together, using the available software package, to create a single image set. The cameras were attached above the inlet chamber with railings at a distance of 1.6 m above the region of interest. The railings also made it possible to adjust the position of the camera. The laser position was controlled using a 3-axis traverse system which made it easy to align the laser beam with the flow field plane as well as to traverse the laser along this plane.

A calibration procedure was performed on the cameras before testing could commence: first, focusing the cameras' lenses on the right plane and second, calibrating a captured image to the actual size of the area being photographed. Both procedures were done using a dot grid calibration target, on which the camera could be focused. The spacing between each of the dots is set and thus using this grid spacing the software package could calibrate the captured image according to the actual size of the area captured. Finally, the laser beam had to be aligned to the height of the testing plane in such a way that the illuminated particles would be in focus.

To capture the whole 2-D vector field stretching across the front of the first and half of the second fan required multiple cameras -and laser positions. To capture the

flow field in front of the perimeter fan, the two cameras were aligned to capture the upstream and downstream half of the flow field separately with the laser being in position 1 (refer to Figure 32). But because the laser has a narrow beam only one camera at a time could be used. So, the laser was aligned with camera 1 and as soon as the adequate number of images was taken the laser was traversed to align with camera 2. To capture the flow field in front of the downstream half of the perimeter fan and the upstream half of the second fan, the camera positions were adjusted, and the laser was placed in position 2 (shown in Figure 33). The benefit of the laser in position 2 was that both cameras could be used to take images simultaneously as the laser beam stretched across both the cameras' view. Laser position 2 could not be used to capture the flow field in front of the first fan because with the windscreen installed the laser beam reflected off the windscreen into the view of the camera, causing light distortion resulting in the data being unusable.

Figure 33: PIV setup with the laser in position 2

The PIV test had to be conducted at night as during the day the room had too much natural light and as a result, the illuminated particle would not appear as bright on the images. For the tests, all lights in the room were switched off and the low-speed wind tunnel was set to the required speed and fans were set to 1000 rpm. The seeding generator was switched on and the system was left for approximately 2 minutes to stabilize. After stabilizing, an image set was taken (in accordance with the required procedure, as discussed above) whereafter the cross-flow rate was incrementally increased. This process was done at five cross-flow rates without a windscreen installed, thereafter repeated with the M50 windscreen installed at 25%,

50%, and 75% inlet covering. For each of these cases, the same five cross-flow rates were used.

Figure 34 shows the dot grid calibration target, from the figure one can see that the inlet chamber's interior was painted matt black to reduce the reflection of light. More details on the PIV equipment and validation are given in Appendix E.

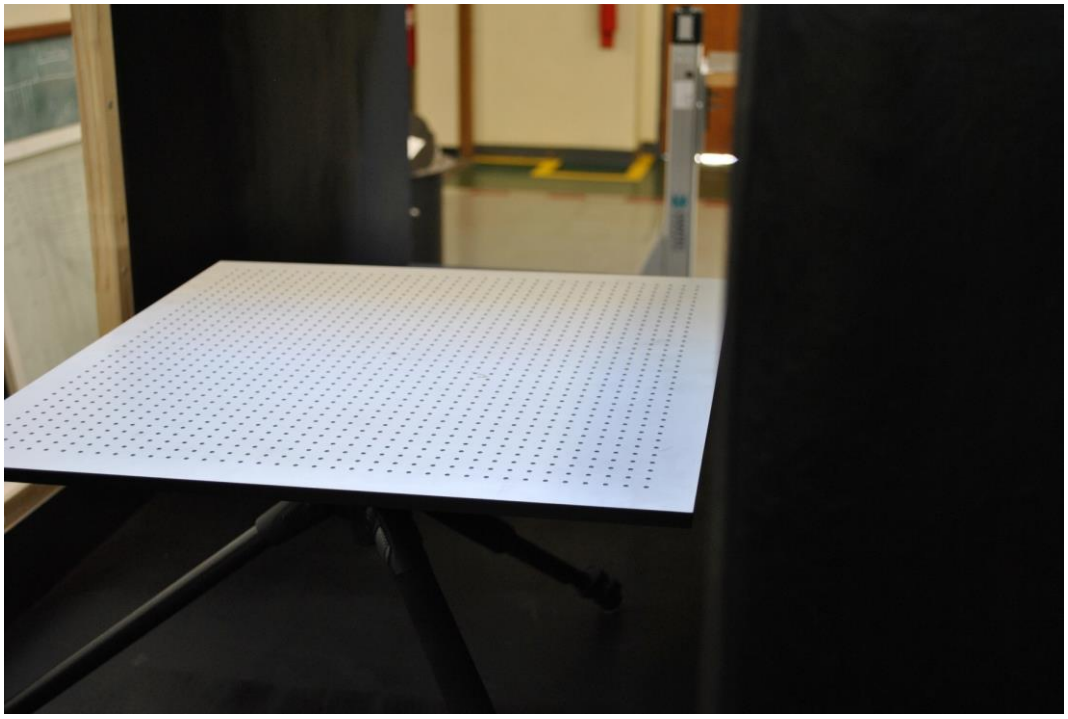

Figure 34: Dot grid calibration target

5 Experimental results and discussion

5.1 Individual fan performance

The measured static pressure rise for the 630L blade at a blade angle of 10.5º±0.2º is given in Figure 35. The data captured by Fourie (2014) is also displayed as a comparison.

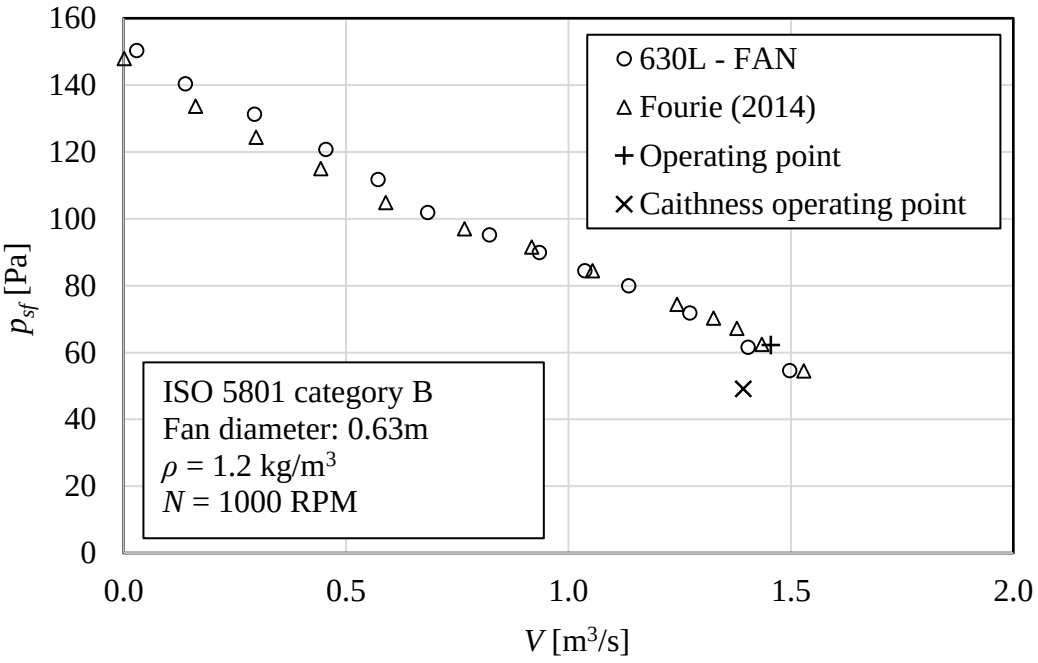

Figure 35: Fan static pressure rise

The two sets of data for the fan static pressure compare well, with a maximum difference between the two, in terms of static pressure, only being 4.9%. The measured fan power, shown in Figure 36, also had a good comparison with the maximum difference being 4.2%. This good similarity adds confidence in the measurement techniques as well as the calibration procedure used.

For comparison, the operating point (OP) for the multiple fan test facility and Caithness' design operating point (Maulbetsch and DiFilippo, 2016), scaled according to the fan laws, is also indicated in Figure 35.

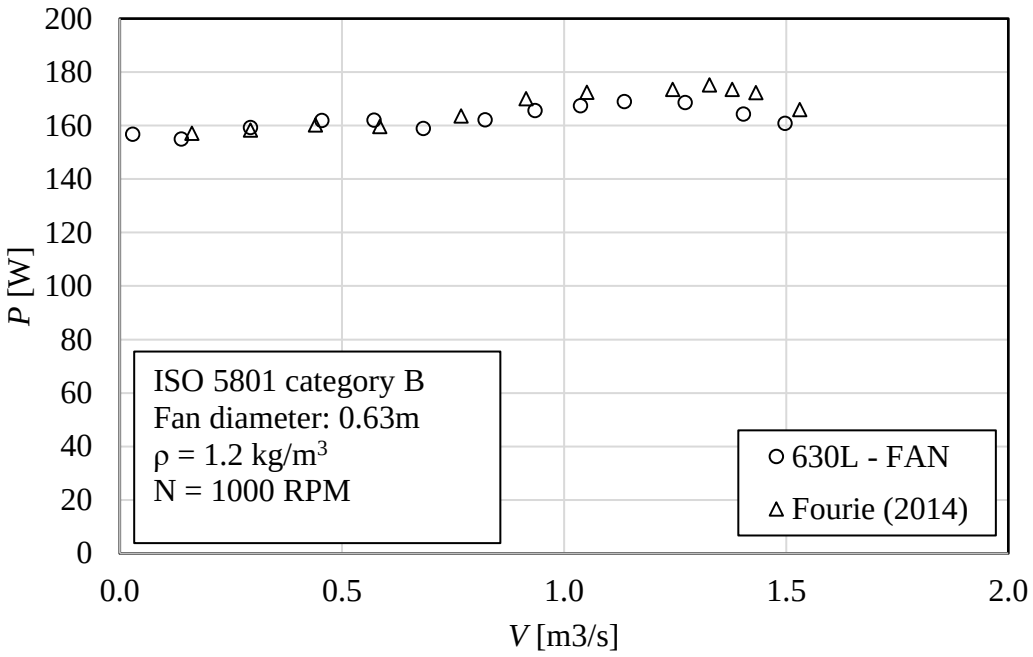

Figure 36: Fan power

The performance characteristics of the fan were tested under ideal inlet conditions and thus with increasing cross-flow, the inlet is subjected to distortions that affect the performance and causes off-curve performance. As a result, the individual fan performance results cannot be used to predict the performance of the fan under strong cross-flow conditions.

The ideal flow rate through each fan test section was recorded by measuring volume flow rate through each section under ideal inlet conditions (without the inlet chamber connected) and is given in Table 2. This was needed to calculate the volumetric effectiveness as given by Equation 1.

Table 2: Ideal volume flow rate

V_{ID1} $[m^3/s]$	V_{ID2} $[m^3/s]$	V_{ID3} $[m^3/s]$
1.42	1.45	1.45

5.2 Fan performance without a windscreen

This section gives the results for the free-inlet, ducted-inlet and fan performance test under increasing cross-flow without a windscreen installed.

5.2.1 Performance comparison between free-inlet and ducted-inlet

The performance of the ducted-inlet case had to be matched to that of the free-inlet case. The two cases were compared with regards to the volumetric effectiveness of each of the 3 fans as well as the inlet velocity profile. As mentioned, an auxiliary flow rate was provided for the ducted-inlet case, which was equal to approximately half the volume flow rate delivered by the 3 fans under the free-inlet case. The auxiliary flow rate was equal to V_{nw} = 2.07 m^3/s. This is referred to as the no-wind scenario. Table 3 shows the volumetric effectiveness through each of the fans for the free-inlet and ducted-inlet cases.

Table 3: Comparison between the volumetric effectiveness of the free-inlet and ducted-inlet cases

Free-inlet			**Ducted-inlet**		
ξ_{f1}	ξ_{f2}	ξ_{f3}	ξ_{f1}	ξ_{f2}	ξ_{f3}
0.948	0.973	0.952	0.949	0.915	0.933

The results for the volumetric effectiveness of the two cases show that they compare well except for the second fan where the difference between the ducted-and-free-inlet case was 6%. During testing, it was noted that the second fan, especially at the no-wind scenario, suffered transient surging effects. The exact reason for this is unknown but there is a possibility that it is due to the second fan's air intake being non-symmetrical which would cause the majority of the inflow to come from a single side (either the first fan or the third fan), but if the dominant side switches, the flow rate of the second fan would experience a sudden change which could account for the surging. The surging effect could not be addressed and as a result, the slight performance difference had to be accepted. The windward fan, which was the primary focus of the study, performed on target compared to the free-inlet case.

Determining the system volumetric effectiveness from the above-given data and comparing it with the predicted system performance, using Equation 2, is given in Table 4.

Table 4: System volumetric effectiveness

Free-inlet	**Ducted-inlet**	**Equation 2**
0.958	0.933	0.949

The difference between the free-inlet and ducted-inlet, in terms of total fan system performance, was a mere 2.6%, this difference is mostly a result of the surging experienced by the second fan as discussed above, and the difference between that predicted by Equation 2 (for 3 fans) and the ducted-inlet was only 1.7%.

The pitot tube traverse of the free-inlet compared to the ducted-inlet is given in Figure 37.

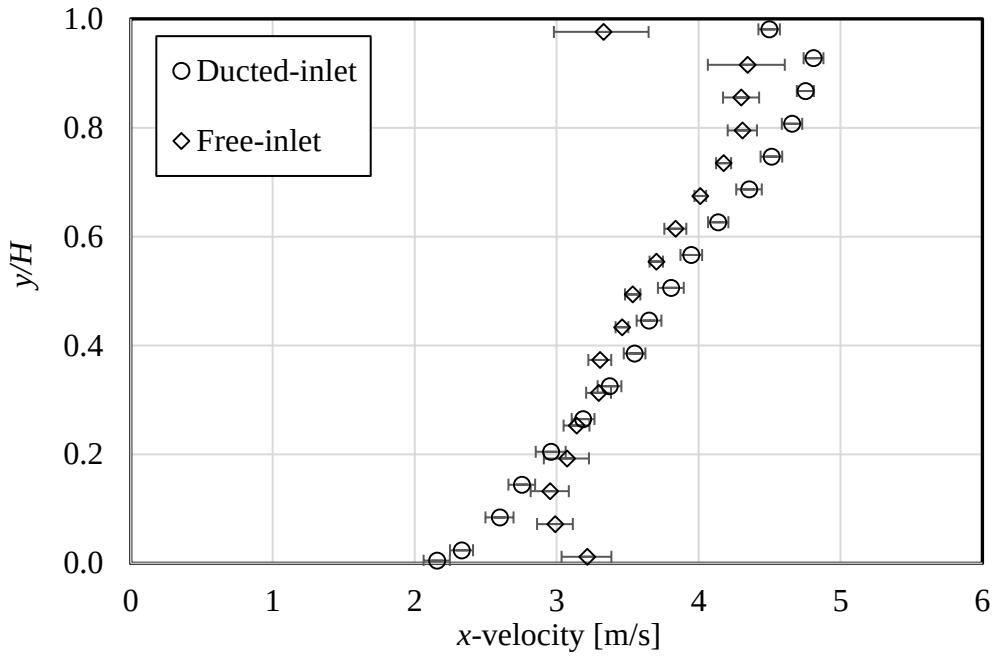

Figure 37: Pitot tube traverse of the free-inlet and ducted-inlet

The two profiles compare well for the majority of the inlet domain except at the extremes of the fan platform at the top and the floor at the bottom. The difference at the fan platform could be due to the flow not being aligned with the pitot tube resulting in some measurement uncertainty. In the free-inlet case, the floor board was not infinite in the flow direction and the fans were able to draw flow from below the floor resulting in the difference in profiles at this location. Determining the average *x*-velocity from the measured profiles (shown in Figure 37), by means of trapezoidal numerical integration, yields a value of v_x = 3.5 m/s for the free-inlet and v_x = 3.7 m/s for the ducted-inlet which is a difference of 5.4%. Although the free-inlet and ducted-inlet fan performance and inlet profiles were not perfect the similarity in the flow conditions upstream of the fans between the two cases is deemed sufficient to allow for continuation of the study with the ducted-inlet.

5.2.2 Fan performance with increasing cross-flow

The performance of each of the three fans is given in terms of volumetric effectivesness under increasing average cross-flow. The average cross-flow velocity (v_x) is nondimensionalised with respect to the fan tip speed (v_{tip}). This dimensionless parameter is denoted as β, as given in Equation 12.

$$\beta = \frac{v_x}{v_{tip}} \tag{12}$$

The dimensionless parameter was selected to avoid misinterpretation of average cross-flow velocity with that of wind speed. The average cross-flow velocity measured in the scaled facility is effectively a combination of induced draft, caused by the fans, and the simulated wind (as described in Section 3.2).

An approximation for the simulated wind speed at platform height (v_w) is given by Equation 13. This was derived by calculating the difference in the volumetric cross-flow rate of each test point (V_x) with that recorded at the no-wind scenario (V_{nw}) and adding the differential change in fan volumetric flow rate, between the two cases, $V_{f\,(nw)}$ and V_f, the numerical subscript denotes the fan number. To calculate the wind speed at platform height the equation must be divided by inlet cross-sectional area (A_x) and multiplied with an integrational constant (see Appendix B.2 for the derivation of this constant).

$$v_w = \frac{8 \cdot \left[(V_x - V_{nw}) + \sum_{i=1}^{3}(V_{f\,i(nw)} - V_{f\,i})\right]}{7 \cdot A_x} \tag{13}$$

Figure 38 shows the correlation between the estimated wind speed calculated using Equation 13 and the dimensionless cross-flow velocity. This is however only valid when no windscreens are used, as the addition of a windscreen adds additional flow resistance and thus effects the performance of each of the three fans.

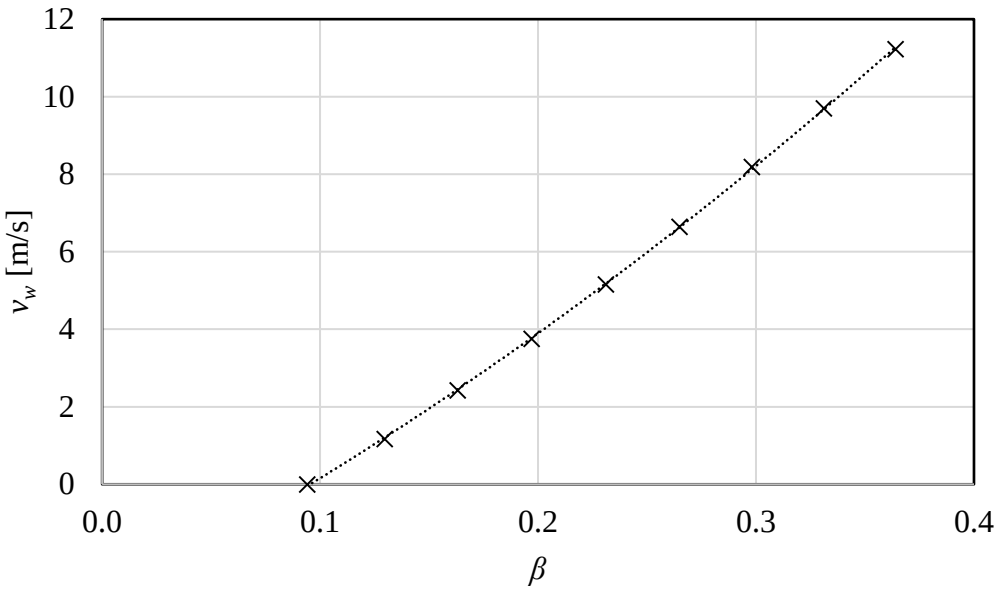

Figure 38: Estimated wind speed at platform height

Equation 14 gives a correlation between the wind speed at platform height and the dimensionless cross-flow velocity. The correlation was determined by curve fitting a second order polynomial equation to the data presented in Figure 38.

$$v_w = 28.86\beta^2 + 28.73\beta - 3 \quad (14)$$

Figure 39 shows the fan performance in terms of volumetric effectiveness, under increasing cross-flow, for each of the three fans. The results given are that of the average of four tests, the maximum standard deviation between these four tests for all three fans in terms of volumetric effectiveness was $\sigma_{max} = 0.013$ and thus too small to be indicated on the plots (data and standard deviations are given in Appendix D.1). Only the performance of the perimeter fan is negatively affected by the increasing cross-flow, whereas the performance of the second and third fan sees a slight improvement.

Figure 40 shows a comparison between the recorded experimental results and Equation 7 for the total system volumetric effectiveness at different average cross-flow velocity.

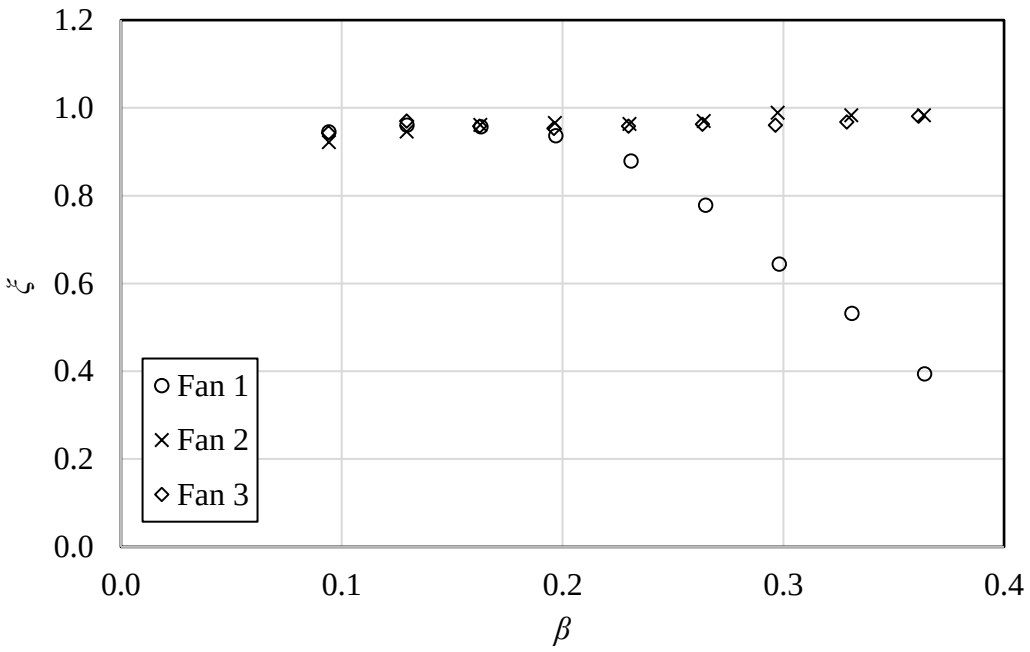

Figure 39: Volumetric effectiveness under cross-flow conditions

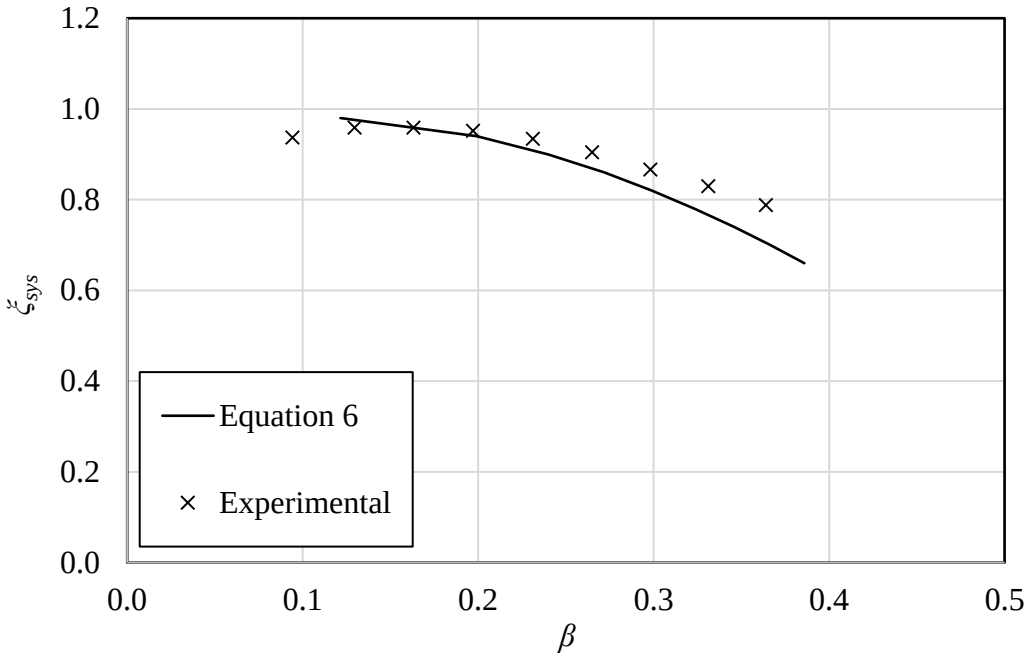

Figure 40: System volumetric effectiveness

The discrepancy between the experimental results and Equation 7 could be attributed to the fact that Equation 7 does not take into account different fan blade types and as a result, under predicts the performance of fans that are less influenced by inlet flow distortions. This was seen by Fourie (2014) and van der Spuy (2011) as blades with steeper fan static pressure curves perform better under increasing cross-flow.

From the PIV vector fields given in Figure 42, the increasing cross-flow can easily be visualized with the addition of a contour plot giving the velocity magnitude. At $\beta = 0.1$ the volumetric effectiveness of the first fan equals $\xi_{f1} = 0.95$ and this decreases to $\xi_{f1} = 0.5$ at $\beta = 0.33$. The reason for this seems to be due to a separation occurring at the bellmouth of the perimeter fan and as the cross-flow increases, this separation region increases in size, until it eventually stretches across the entire first half of the fan blade at $\beta = 0.33$. This would drastically affect the performance of the perimeter fan as the flow can only be re-entrained into this fan beyond the separation region. The separation region that has formed in front of the windward fan does seem to help entrain flow into the second fan and combined with the increasing cross-flow, helps boost the performance of the second fan. Figure 41 shows the dimensions for the PIV plots given in Figure 42 and throughout the rest of this section.

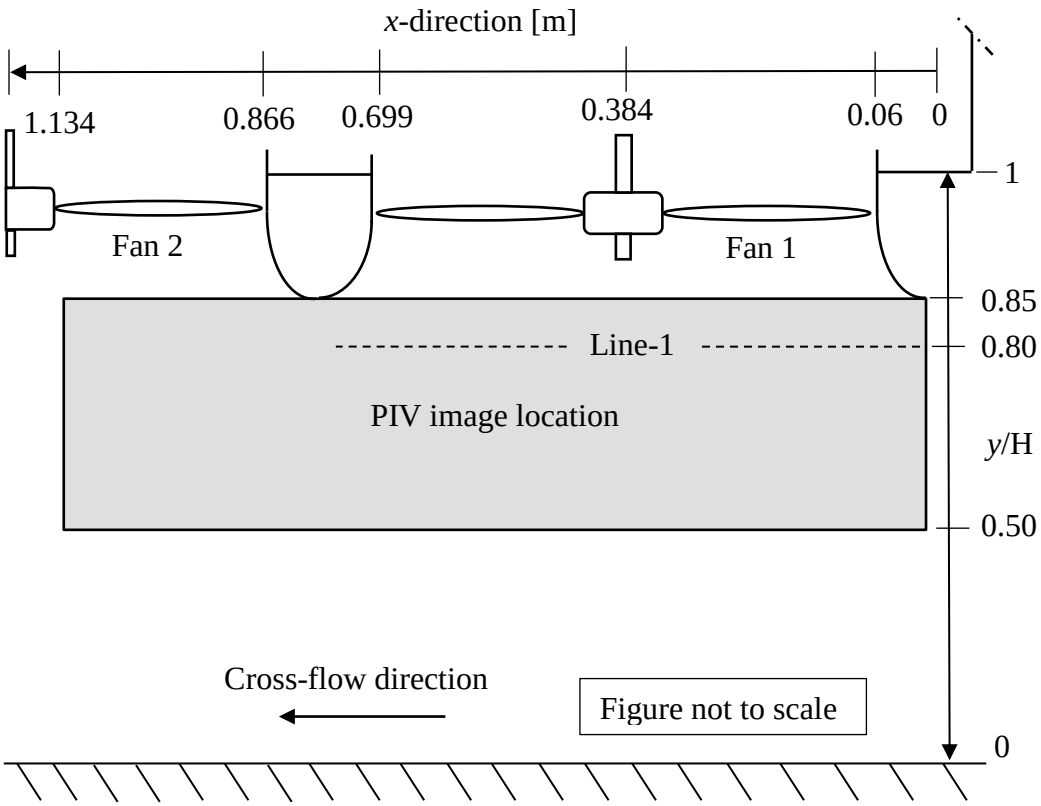

Figure 41: PIV image location

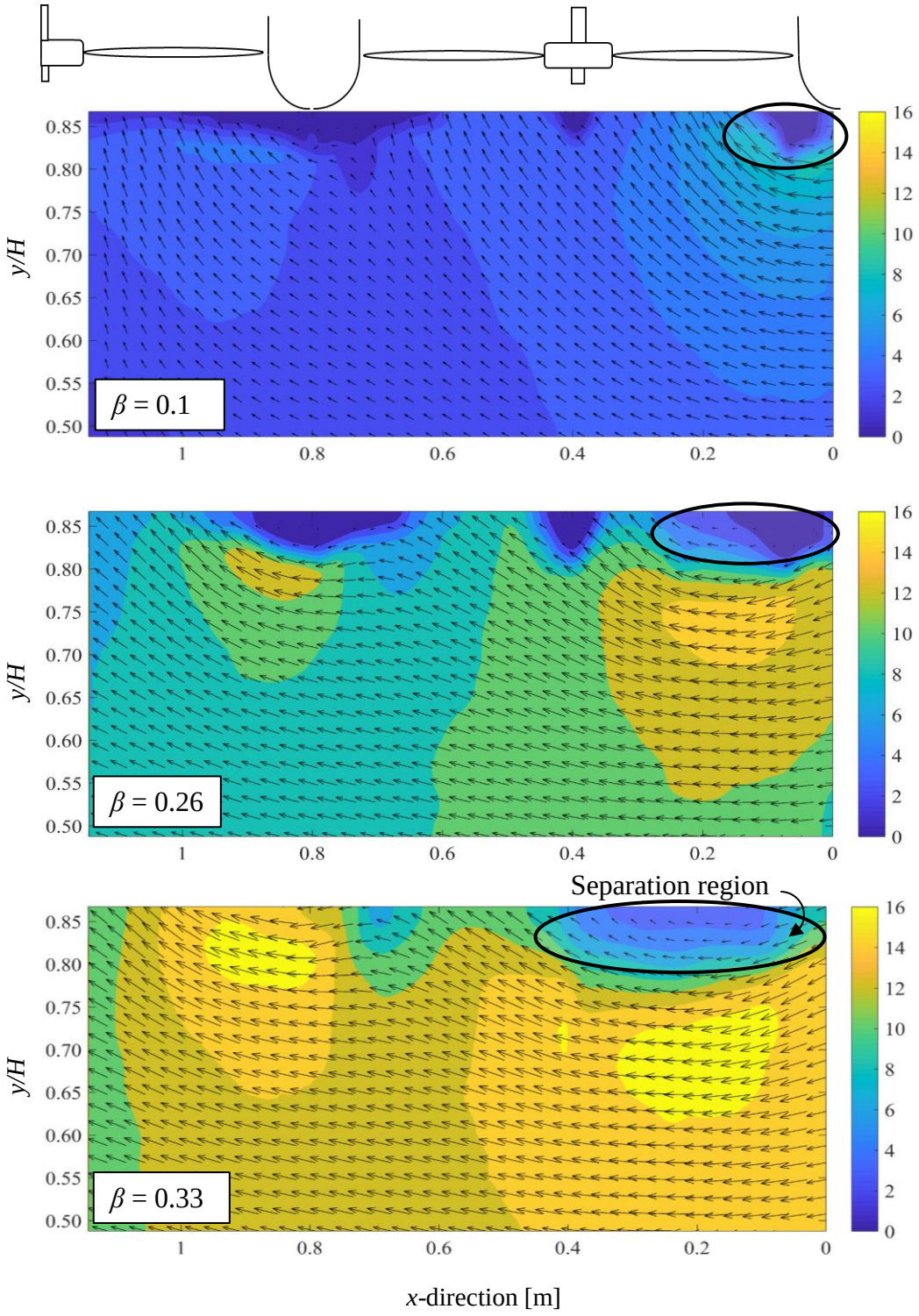

Figure 42: PIV flow visualization for the no-windscreen case for β = 0.1, β = 0.26 and β = 0.33

The separation region, indicated by an oval within Figure 42, causes a low-pressure zone that would effectively act as an additional flow resistance for the first fan to overcome and thus negatively affects the volumetric flow rate produced by the fan. The low-pressure zone would also increase the pressure gradient between the upstream and downstream of the fan and this could potentially cause impedance stall that would account for the increase in fan power consumption of the perimeter fan as shown in Figure 43. Fan power was only measured at the perimeter fan, as this was the only fan test section fitted with a torque transducer. Impedance stall occurs if there are very high-pressure gradients present across an aerofoil, this high-pressure gradient causes flow separation which leads to stalling. The combination of increasing fan power consumption combined with the reduction in fan static pressure rise results in a reduced fan efficiency.

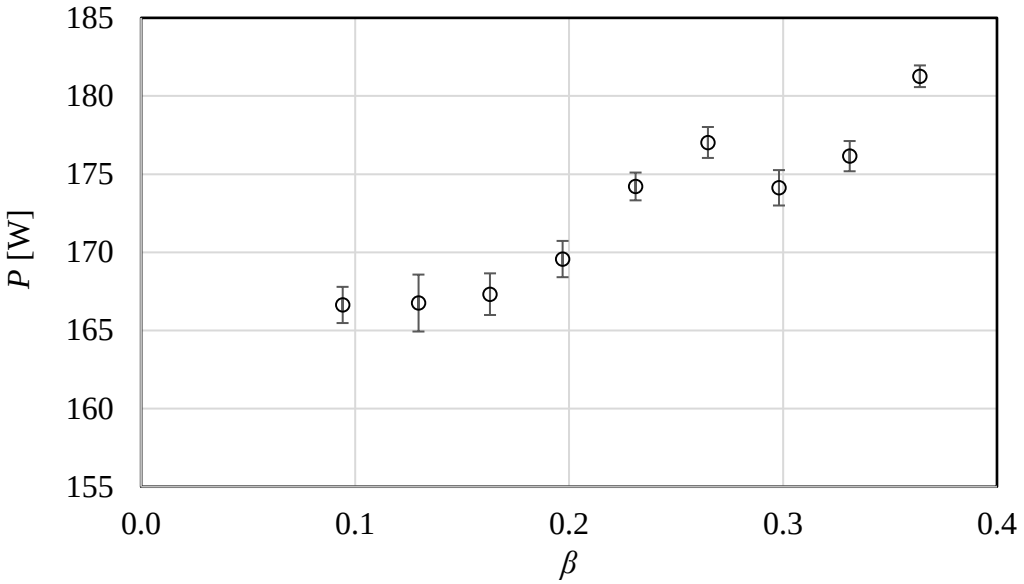

Figure 43: Fan power under cross-flow of fan 1

Increasing power consumption combined with the reduction in flow rate, as the cross-flow is increased, is uncharacteristic based on the individual fan performance tests.

5.2.3 Full-scale comparison

Due to the scaled facility having a similar dimensionality to that of Caithness Energy Center's ACC it was possible to compare test data for the volumetric effectiveness of the perimeter fan and the second fan to full scale data from Caithness facilities' fan 3.4 and fan 2.4 (refer to Section 2.2) as recorded by Maulbetsch and DiFilippo (2016). The volumetric effectiveness for fan 3.4 and 2.4 was calculated from the average air inlet velocity into the fan shroud (at a diameter of 11.66 m), the ideal volumetric flow rate was taken as 750 m^3/s as this was the

approximate recorded average flow rate through the fan over a year. This was used because Maulbetsch and DiFillipo (2016) stated that the fans at Caithness had performed off curve and as a result, the operating point did not match the actual performance of the fans.

The volumetric effectiveness of the scaled facility is plotted against the predicted wind speed at platform height (v_w) calculated using Equation 13. To account for the dimensional difference the wind speed was nondimensionalised with respect to the blade tip speed (v_{tip}). This method was taken from Fourie (2014).

Figure 44 shows the comparison between the full scale and scaled facilities perimeter and second fan's volumetric effectiveness.

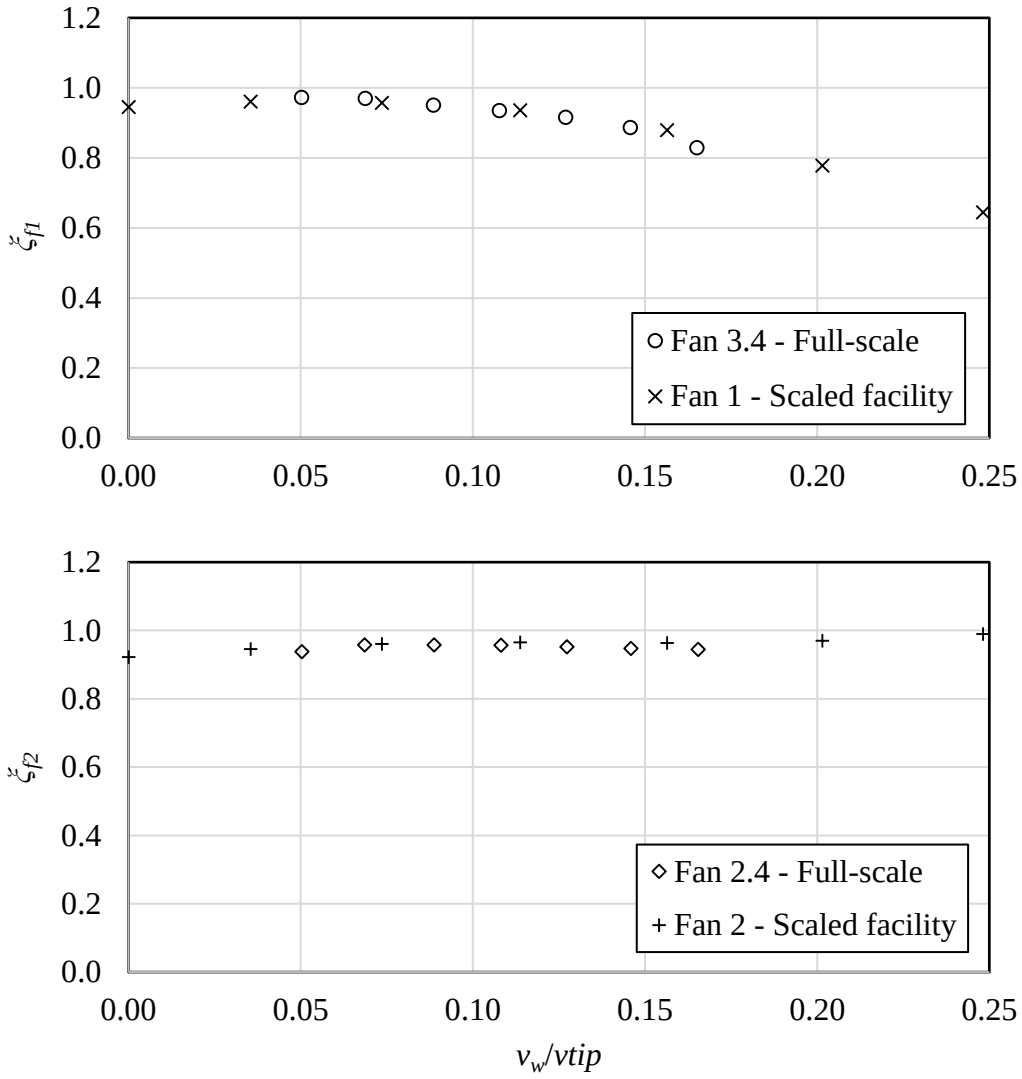

Figure 44: Comparison between experimental and full-scale volumetric effectiveness

Although the full-scale data was only available for a limited wind range, such are the limitation of full-scale experimental testing, the available data had a very good correlation with that of the scaled facility based on volumetric effectiveness. The two data sets correlate well, but there are obvious factors that differentiate the two, such as the wind direction of the full-scale data not being purely westerly, the scaled facility only consisting of a single fan row, the full-scale facility having adjacent buildings influencing the in-flow and of course the uncertainty with regards to the method used to estimate the wind speed at platform height for the scaled model. Aside from these obvious differences between the full-scale and the scaled model, the good correlation between the two models gave confidence in the technique used to simulate the wind effects on an ACC fan row and countered the uncertainty regarding the differences in dynamic similarity between the full-scale and scaled facility, as similar performance was observed in the scaled facility as was measured at the full-scale facility.

5.2.4 Dynamic blade loading of the perimeter fan with increasing cross-flow

For the vibrational analysis of the perimeter fan blade, it is important to know the blades natural frequency as this indicates which excitation frequency would cause resonance. The natural frequency was determined by exciting a single fan blade, with a low impact force in the flapwise direction, across a range of frequencies and then allowing the blade to vibrate freely until the vibration was naturally dampened out. The bending strain data that was captured from this response was then analyzed using a fast Fourier transform (FFT). Figure 45 shows the time response and the FFT response.

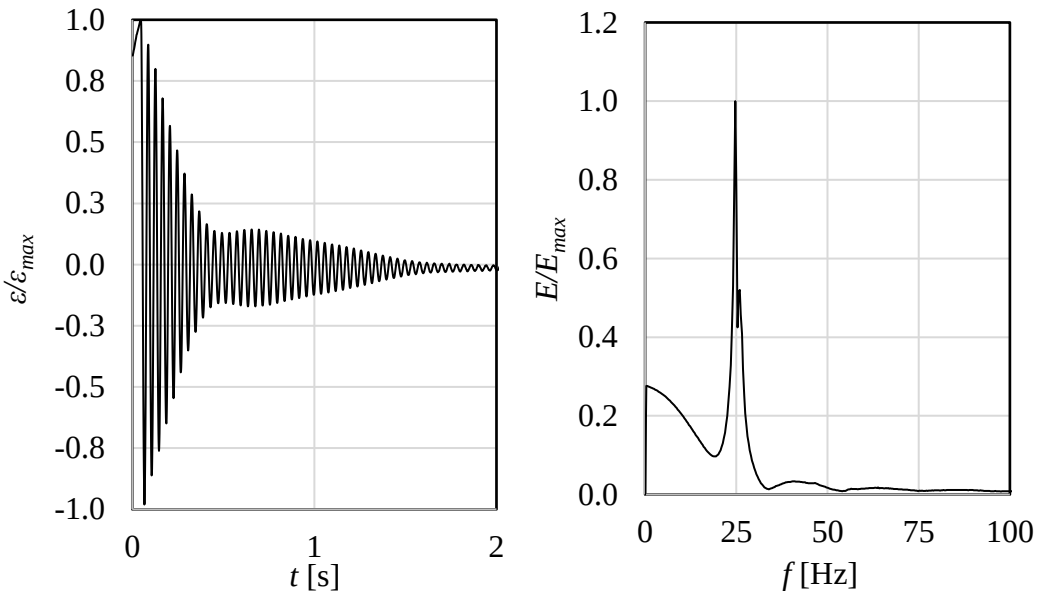

Figure 45: Fan blades time response (left) and FFT (right) after a single disturbance

The dominant peak in the FFT represents the blades first natural frequency in the flapwise direction, which is at $f_n = 24.7$ Hz. Interestingly there is a small peak directly after the dominant peak, this is not the second natural frequency of the fan blade but is likely a representation of the whole system's natural frequency (where the system is the hub with each of the 8 fan blades attached). Both plots' amplitudes have been normalized with respect to the maximum value, the bending strain data was normalized as the strain value itself was of little meaning because of the material of the blade and the FFT was normalized also due to the values itself being of little meaning.

To quantify the effect that increasing cross-flow has on the blade vibration, the root mean square (rms) value was calculated from the cyclic blade bending strain data. For the calculation of the rms value the mean had been subtracted from the data set in order to analyse only the dynamic strain component. Figure 46 shows the normalized bending strain over a range of cross-flows, the data showed has been normalized with respect to the average rms value at the no-wind scenario across four tests with the error bars representing the standard deviation between the four tests. The average rms value at the no-wind scenario was selected to normalize the data as this then indicates to what extent the rms strain value has increased above the no-wind scenario.

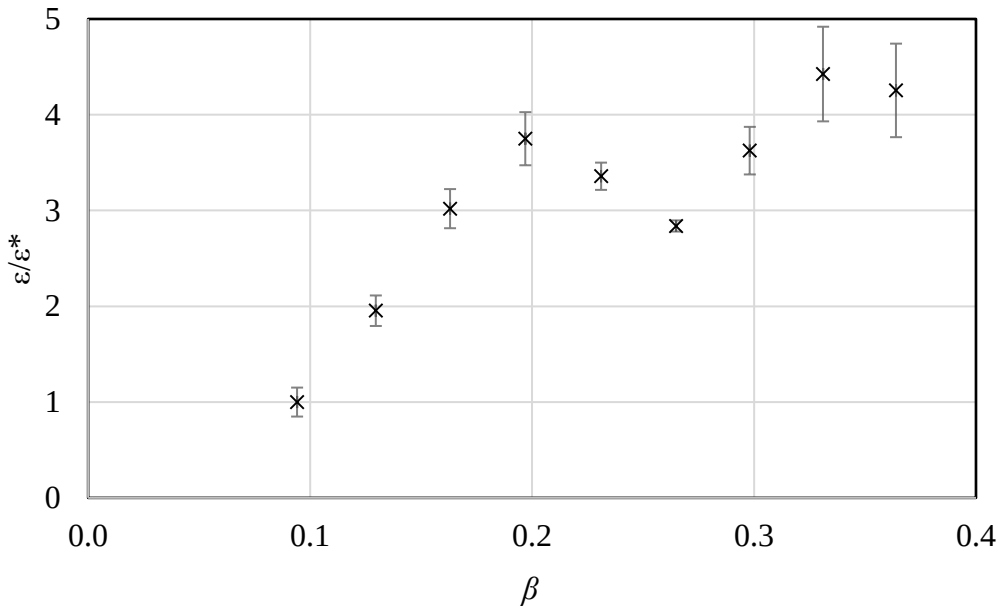

Figure 46: Normalized blade bending strain

There was a linear increase in the blade bending strain until $\beta = 0.2$ and at this point there was an unexpected reduction in the measured bending strain between $0.2 \leq \beta \leq 0.33$. The increase in bending strain was expected as the cross-flow was incrementally increased and corresponds to what was reported by Muiyser *et al*.

(2016). With the help of flow field visualization obtained through the PIV testing the bending strain data could be analysed better. Figure 47 shows the vector plots of the velocity fields at the inlet of the perimeter fan, with a colour contour overlay of the velocity magnitude.

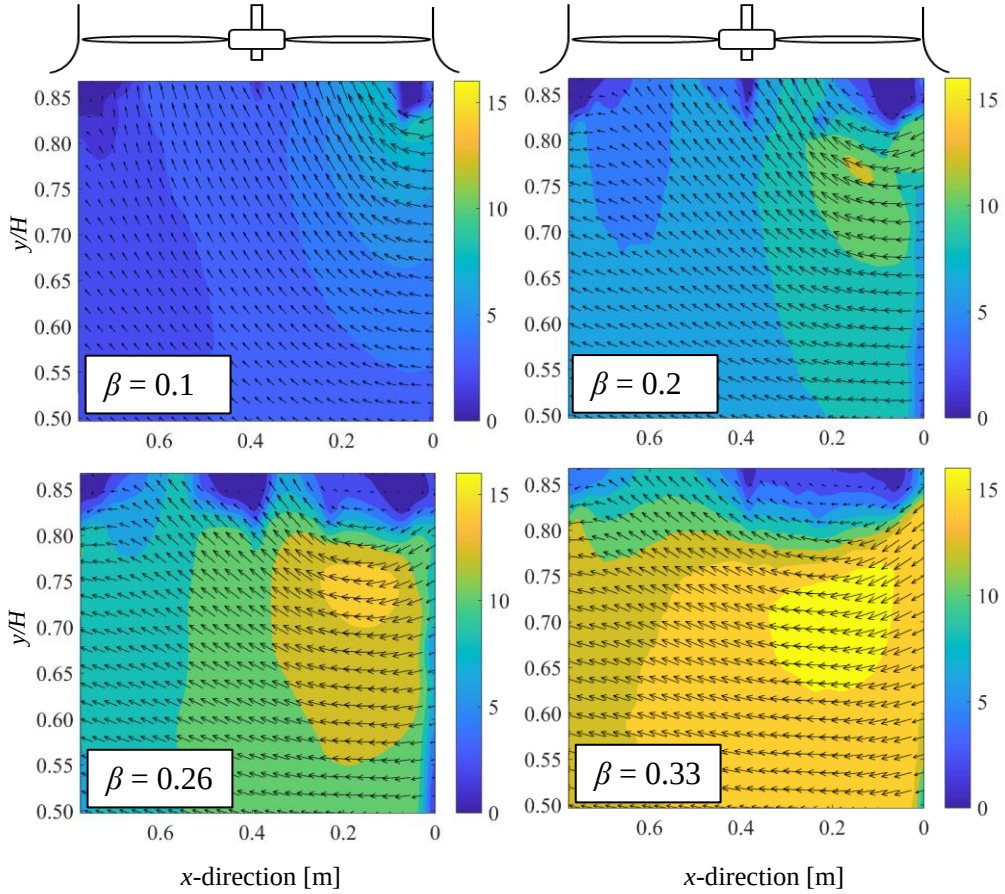

Figure 47: PIV of fan 1 for the no-screen case at β = 0.1, β = 0.2, β = 0.26 and β = 0.33

The PIV vector field stretches along the center plane as this is the region where the *y*-velocity into the fan is expected to have the most variability. The variation in approach velocity along the length of the blade is believed to be a contributing factor to increasing the dynamic blade loading under cross-flow. From the PIV vector field, it is obvious that as the cross-flow increases the separation region increases in size, starting at the tip of the bell-mouth and extending across the inlet of the fan. This causes the region with the highest *y*-velocity (v_y) to shift away from the edge (windward side) towards the interior of the fan and results in an increased difference in *y*-velocity profiles of the upstream and downstream half of the fan.

The presence of a separation region causes a low-pressure zone, where within recirculating flow or even back flow may be expected (this is confirmed in Figure

48). When the fan blade rotates through this region, very limited lift is expected to be generated by the blade's aerofoil. This would cause a variation in the aero-dynamic loading experienced by the blade within one rotation. Figure 48 shows the *y*-velocity into the perimeter fan along line-1 (as depicted in Figure 41, see Section 5.2.2), the data from the hub region has been neglected.

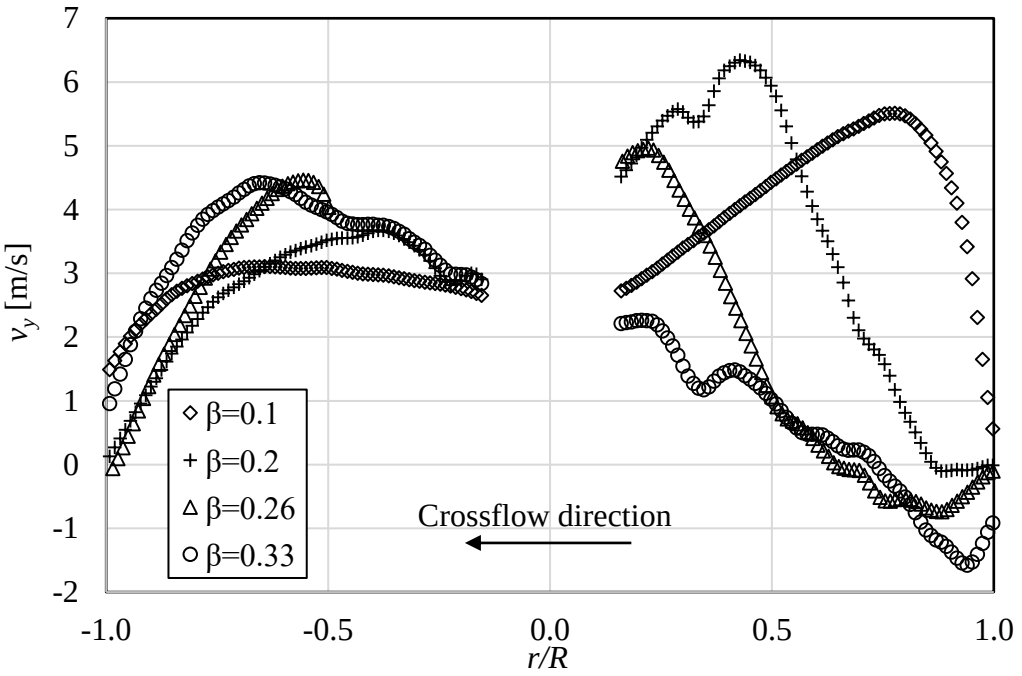

Figure 48: *y*-velocity into fan 1 along line-1

From Figure 48 the reduction in fan performance can be observed as there is a reduced amount of inflow (defined by the *y*-velocity into the fan) into the upstream half of the perimeter fan, as the cross-flow increases. Both the shift in the high *y*-velocity region as well as the formation of the separation region can be observed, with backflow being measured within the separation region. The significant differences in *y*-velocity profiles of the up-and downstream halves of the fan can be observed in Figure 48, especially for $\beta = 0.2$ and $\beta = 0.33$ where for both of these cases the fan blade was subjected to high dynamic blade loading.

The reduction in dynamic blade loading between $0.2 \leq \beta \leq 0.33$ was however unexpected. This does indicate a possible change in the excitation mechanism within that range and beyond. To further investigate this claim, it is worth looking at the Fast Fourier Transform (FFT).

Figure 49 shows the FFT for $\beta = 0.1$, $\beta = 0.2$, $\beta = 0.26$ and $\beta = 0.33$. The amplitude of each of the FFT responses has been normalized with respect to its own maximum value, the dashed line indicates the maximum normalized amplitude of the no-wind case ($\beta = 0.1$). The FFT confirms the suspicion that there is a change in the

excitation mechanism between $\beta = 0.2$ and $\beta = 0.26$. At $\beta = 0.2$ the dominant frequency is at twice the rotational frequency (Ω) while at $\beta = 0.26$ this response diminishes, and the dominant frequency is at the rotational frequency.

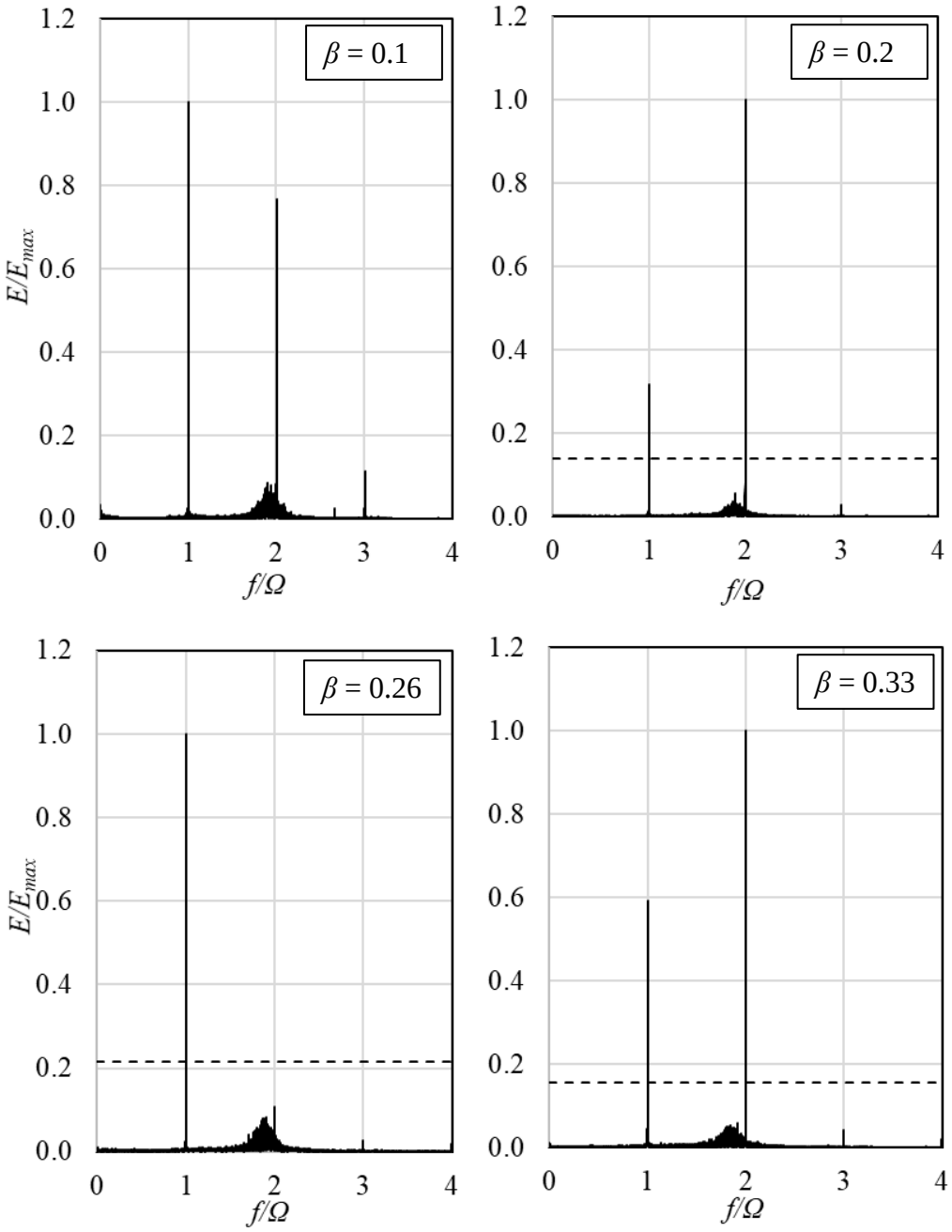

Figure 49: FFT's of the bending strain data for $\beta = 0.1$, $\beta = 0.2$, $\beta = 0.26$ and $\beta = 0.33$

Figure 50 shows the dynamic component of the bending strain normalized with the no-wind rms strain value and indicates the elapsed time (t) starting at an arbitrary

position, with the elapsed time being nondimensionalised by multiplying with the rotational frequency (Ω). The data shown in Figure 50 has been processed by means of time synchronous averaging to reduce the non-synchronous noise (Bechhoefer and Kingsley, 2009).

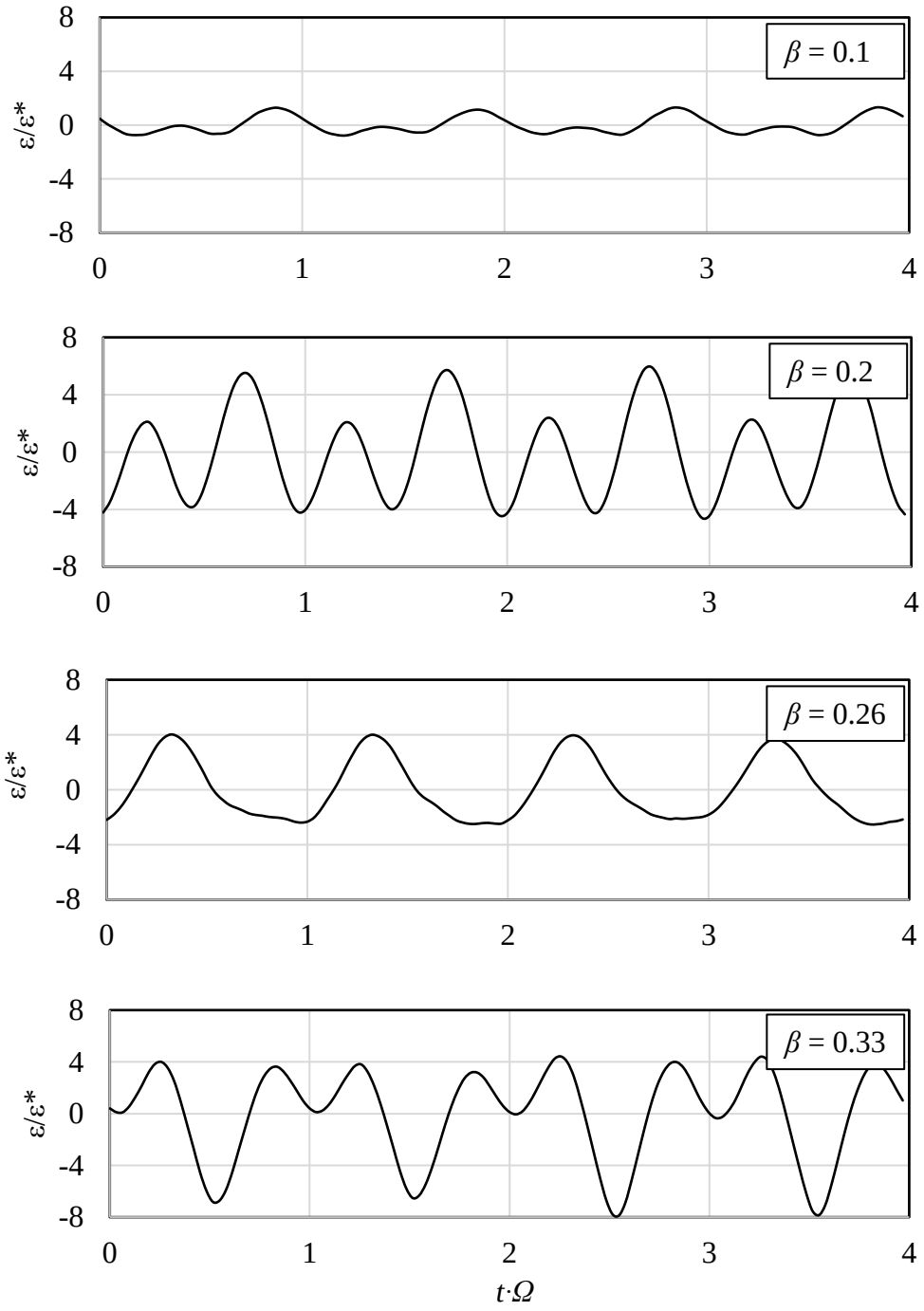

Figure 50: Time response of the normalised bending strain at β = 0.1, β = 0.2, β = 0.26 and β = 0.33

It is interesting to note that twice the rotational speed was the dominant frequency in two of the four cases (β = 0.2 and β = 0.33). This means the blade had two peak strain measurements within one rotation, as may clearly be seen in the time response for both of these cases as given in Figure 50, for β = 0.2 and β = 0.33.The inlet distortion should only affect the blade loading once per rotation and if there is only one excitation per revolution the FFT's dominant frequency is expected to be the rotational speed. The reason for this is thought to be related to the fact that when the blade (with the attached strain gauges) is aligned with the cross-flow direction the *y*-velocity along the length of the blade varies substantially, but when the blade is perpendicularly aligned with the cross-flow direction there is less of a variation in the *y*-velocity along the length of the blade. From the time response of the bending strain data, given in Figure 50, two troughs/peaks with approximately the same amplitude appear at 0.5 $t{\cdot}\Omega$ apart (where 1 $t{\cdot}\Omega$ represents 1 full rotation). These responses should correspond to the moment when the blade is perpendicularly aligned with the cross-flow direction as the loading at these two locations should be similar.

From Figure 50, the time response, the change of the excitation mechanism is visible as the response undergoes a significant change between β = 0.2 and β = 0.33. It would seem that the change in excitation mechanism between β = 0.2 and β = 0.33 corresponds to the point when the separation region has grown substantially in size causing the difference in mean *y*-velocity into the up-and downstream half of the perimeter fan (δv_y) to have a sign change from positive to negative. Figure 51 shows the difference in mean *y*-velocity into the up-and downstream half of the perimeter fan compared to the normalized bending strain as well as the β value (given by the figure labels).

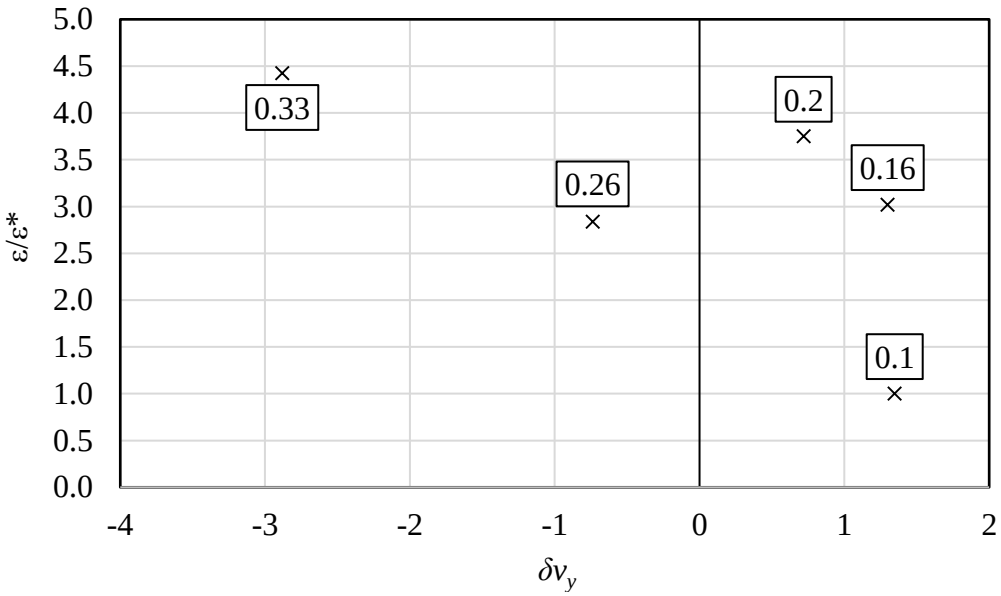

Figure 51: The normalized dynamic bending strain compared to the differential *y*-velocity into fan 1.

Figure 51 indicates that while the mean differential *y*-velocity (δv_y) is positive (between $0.1 \leq \beta \leq 0.2$) the magnitude of this differential velocity cannot be used as an indicator of the dynamic blade loading experienced by the blade. But once the mean differential *y*-velocity is negative the magnitude of this difference in the mean *y*-velocity into the up-and downstream halves of the perimeter fan can be an indicator of dynamic blade loading as there seems to be a linear relation (refer to Section 5.3.2 for additional evidence and a linear correlation).

Although having different excitation mechanisms, the high dynamic blade loading recorded at $\beta = 0.2$ and $\beta = 0.33$ can both be attributed to the significant variation in the *y*-velocity profile along the span of the blade between the up-and downstream halves of the fan (refer to Figure 48). These significant differences in the *y*-velocity profiles cause a variation in the aerodynamic loading experienced by the blade within one rotation and this results in dynamic loading.

5.2.5 Summary

Based on the fan performance, dynamic blade loading and the PIV velocity vector fields, the following observations were made:

1. With the increase in cross-flow a separation region forms at the upstream edge of the perimeter fan's bellmouth. This separation region increases in size, until it eventually stretches across the entire first half of the fan.

2. The separation region causes a dramatic reduction in the perimeter fan's volumetric effectiveness as the flow can only be re-entrained into the fan beyond this region. The increasing cross-flow also results in an increase in fan power consumption, which is thought to be related to the increase in the pressure gradient between the up- and-downstream side of the fan (across the aerofoil) due to the low-pressure zone associated with the separation region.

3. The increasing cross-flow results in a slight increase in the volumetric effectiveness of the second and third fan as it seems that the separation region helps entrain flow into both these fans.

4. With the increasing cross-flow, the formation of the separation region causes a significant variation in the *y*-velocity profiles (aligned with the fan axis) between the up- and downstream portions of the fan (in the cross-flow direction). This results in an increase in the dynamic blade loading measured.

5.3 Fan performance with windscreens

The cross-flow experiments were repeated with the addition of a windscreen covering a portion of the windward inlet of the inlet chamber. The results given in this section mainly focus on the performance of the M50 windscreen as it performs the best out of the 3 solidities. In Section 5.3.3 a comparison is made between the

M50, M60 and M75 windscreens based on the perimeter fan's volumetric effectiveness and dynamic blade loading.

5.3.1 Fan performance with increasing cross-flow

It is important to note that with the installation of the windscreen the performance of the 3 fan sections would be unsymmetrical at the no-wind condition, due to the addition of the upstream flow resistance. As a result Equation 14 that gives a correlation between the β and wind speed can no longer be applied to these results.

Table 5 gives a comparison between the volumetric effectiveness of each of the fans under no-wind conditions (free-inlet) with and without the M50 windscreen attached and for this comparison the inlet duct was disconnected. These results indicate to what extent the installation of the windscreen affects the fan performance of each of the three fans, especially the perimeter fan. This effect is intensified with the increasing solidity of the windscreen due to the flow resistance, caused by the windscreen, being increased. This highlights the fact that the previously determined no-wind case does not apply once the windscreen has been installed, as the presence of the windscreen reduces the volume flow rate entering the fan row from the windscreen's side.

Table 5: Effect of M50 windscreen on no-wind fan performance

	ξ_{f1}	ξ_{f2}	ξ_{f3}
NS	0.94	0.95	0.95
M50 25%	0.92	0.95	0.94
M50 50%	0.90	0.95	0.94
M50 75%	0.88	0.91	0.93

To inspect how the presence of a windscreen influences the performance of the fans as well as the dynamic blade loading experienced by the perimeter fan, the volumetric effectiveness of each of the fans and normalized bending strain, with and without the windscreen, will be compared based on similar dimensionless average cross-flow velocities (β).

The comparison in the volumetric effectiveness of each of the three fans with the M50 windscreen installed (at various percentages of the inlet covered) to that of the results when no windscreen (NS) was installed are given in Figure 52 to Figure 54 (all data and standard deviations between repeated test are given in Appendix D.2).

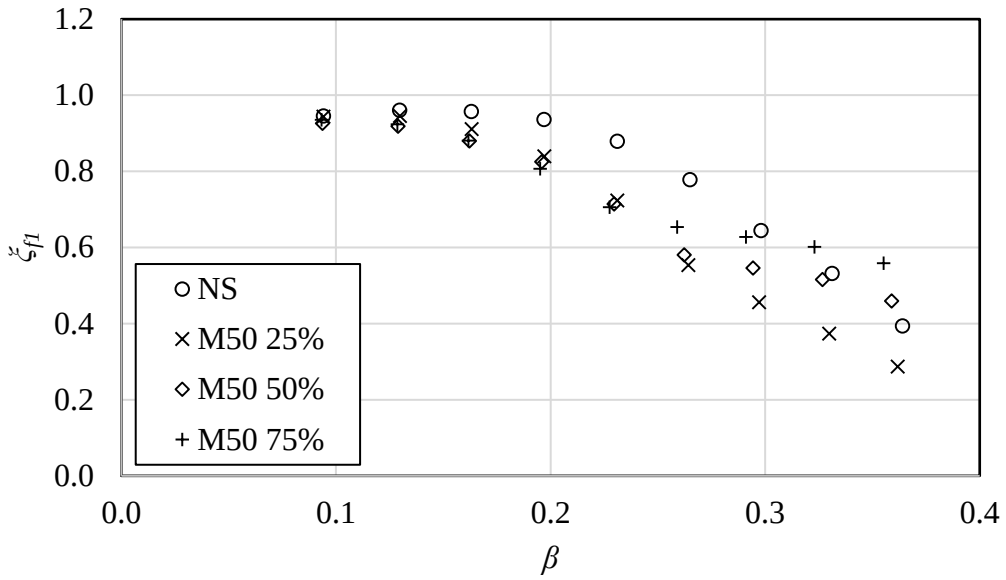

Figure 52: Volumetric effectiveness of fan 1 with M50 windscreen

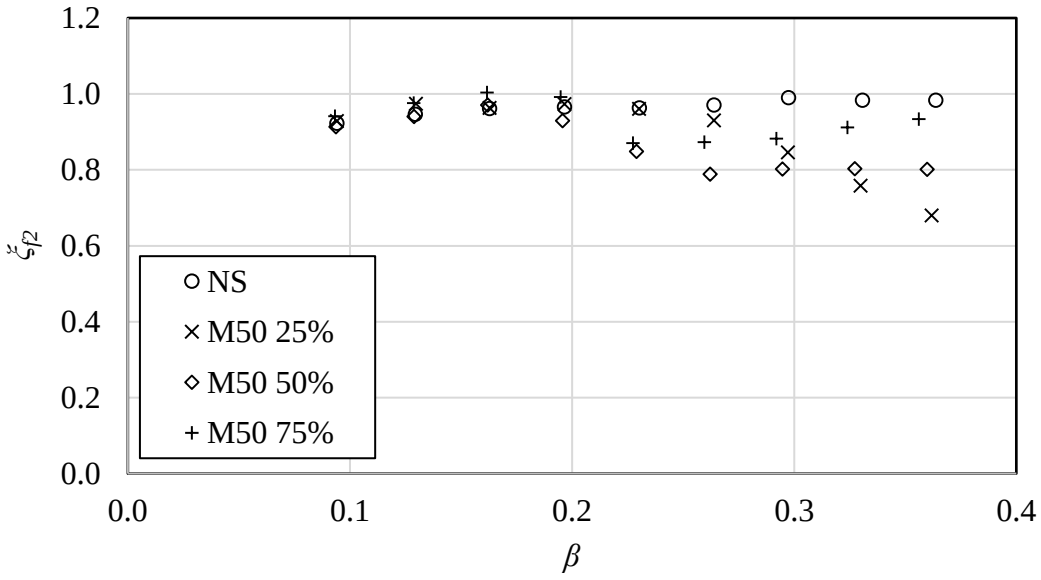

Figure 53: Volumetric effectiveness of fan 2 with M50 windscreen

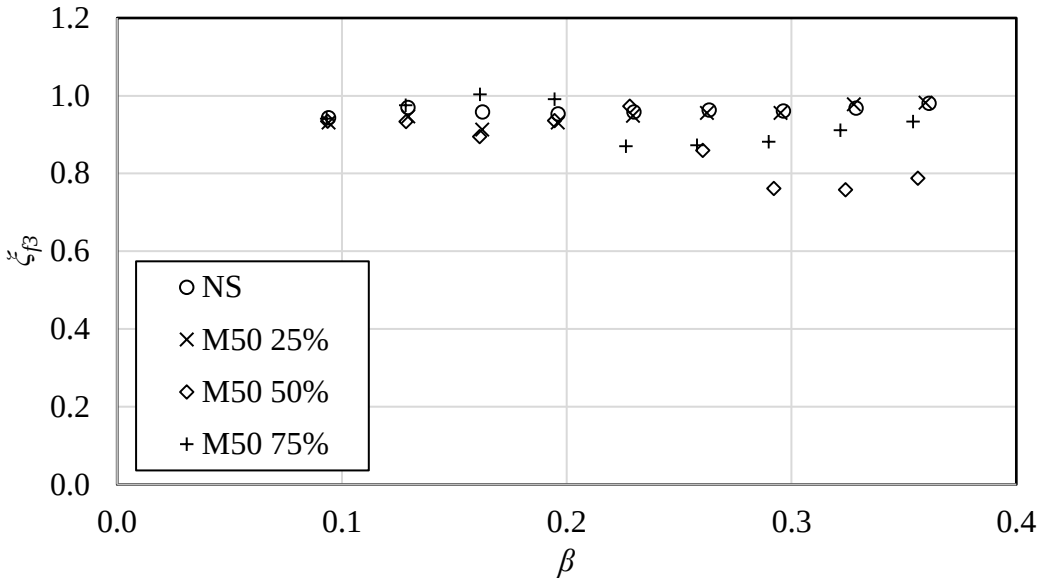

Figure 54: Volumetric effectiveness of fan 3 with M50 windscreen

From Figure 52 it is seen that the addition of the windscreen negatively effects the perimeter fan irrespective of the screen covering percentage, except when a large portion of the inlet is covered and the system is operating at a very high cross-flow rate. At very high cross-flow ($\beta = 0.36$) the addition of the screen, covering a large portion of the inlet, slightly improves the performance of the perimeter fan in terms of volumetric effectiveness.

Intuitively the reason would seem to be that with a small percentage of the inlet covered with a windscreen (25%) the bulk air flow would be deflected away from the inlet of the perimeter fan having a subsequent negative effect on the volumetric effectiveness of the perimeter fan as the fan is effectively being choked. This deflection of the flow helps to slightly improve the volumetric effectiveness of the second -and third fan (shown in Figure 53 and Figure 54), up to certain cross-flow rates. As the cross-flow increases, the bulk air flow that is deflected (by the windscreen) shifts downstream up until a point that even the second fan's performance suffers as observed in Figure 53. Due to the windscreen covering only a small portion of the inlet, the majority of the flow follows the path of least resistance and deflects below the screen.

As the portion of the inlet covered by the screen increases, the amount of flow permeating the windscreen increases due to a combination of the larger screen area and the increasing contraction loss associated with bypassing the screen. With the increasing cross-flow, this benefits the perimeter's fan performance such that at very high cross-flow rates ($\beta = 0.36$) the perimeter fan performance increases relative to the no-windscreen case. This performance increase could be attributed to sufficient flow moving through the windscreen but having a lower x-velocity (cross-flow component) and should therefor result in better fan performance.

Figure 55 shows the PIV vector field of the flow in front of the first fan at $\beta = 0.2$ for the no-screen case as well as the 25%, 50% and 75% covering. Figure 56 is similar but only for a higher cross-flow ($\beta = 0.33$). From Figure 55 (b), the deflection of the flow can be seen as the region with the highest velocity magnitude shifts downward (y-direction) away from the windward side of the fan's inlet, the edge of the screen being at $y/H = 0.75$. For (b) there is a slight discontinuity in the PIV data (indicated with a circle). This was caused by the stitching of the images, but the figure was still included as it gives a good indication of the downward shift of the region with the highest velocity magnitude due to the deflection of the bulk flow by the windscreen. When the screen spreads across 50% of the inlet (c) there is a dramatic decrease in the magnitude of the velocity field to that of 25% covering, as the edge of the screen would be at $y/H = 0.5$, spanning across the entire length of the region captured by the PIV. Here one can also see the flow being deflected by the windscreen (see $x = 0.6$ m and $y/H = 0.5$ in (c)). When the windscreen covers 75% of the inlet the screen's edge is at $y/H = 0.25$. With the larger portion of the inlet covered (50% and 75%) the reduction in the magnitude of the cross-flow (especially the x-velocity component) can be observed.

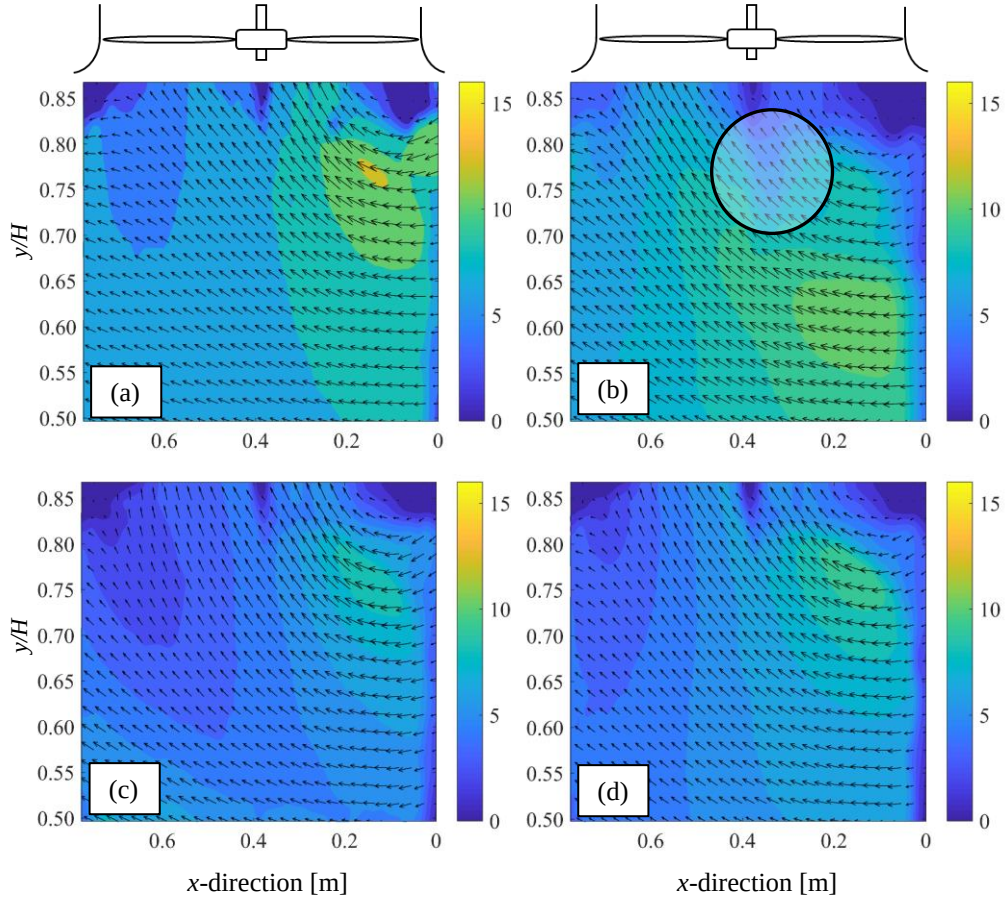

Figure 55: The effect of a windscreen on the inflow of fan 1 at $\beta = 0.2$ with (a) no windscreen, (b) 25%, (c) 50% and (d) 75% covering

For 75% covering (d) and 50% (c) the vector fields are similar as the flow that is deflected by the screen misses the perimeter fan completely (in (c) the flow that is being defected can be observed in the lower right corner of the vector field). As a result the only flow entering the fan had passed through the windscreen, hence the velocity vector plots for 50% and 75% are similar.

Figure 56 shows the PIV at a higher cross-flow of $\beta = 0.33$, here the deflection of the flow is very clear (refer to Figure 56 (b) and indicates the significant reduction in cross-flow velocity once the windscreen covers 50% and more of the inlet (refer to Figure 56 (c) and (d)).

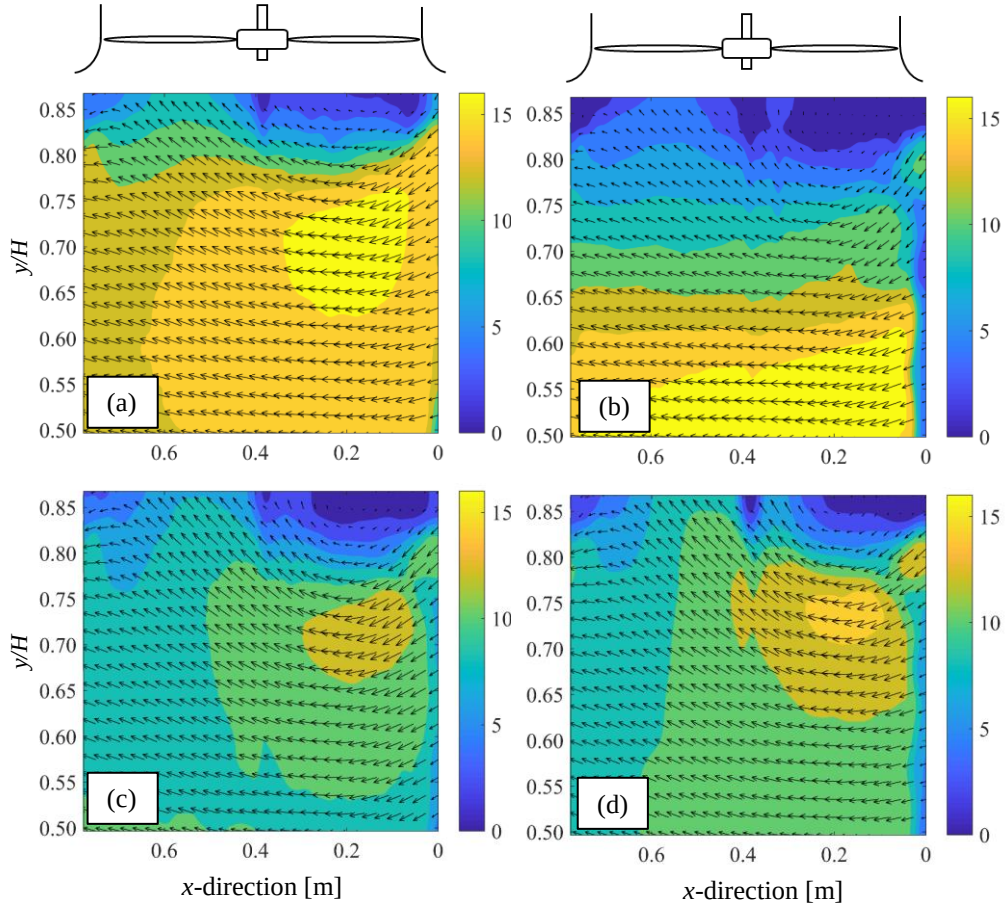

Figure 56: The effect of a windscreen on the inflow of fan 2 at $\beta = 0.33$ with (a) no-screen, (b) 25%, (c) 50% and (d) 75% covering

5.3.2 Dynamic blade loading of perimeter fan with increasing cross-flow

For each of the cross-flow tests conducted with the windscreen installed, the bending strain was measured with a similar procedure as in the no-screen tests. The results for M50 windscreen at 25%, 50% and 75% covering are shown in Figure 57

and these results are compared to the results when no windscreen was installed (all data and standard deviations between repeated tests are given in Appendix D.2).

As reported in section 5.3.1, the windscreen both deflects the flow and throttles the flow through the screen. Both of these effects contribute to lower cross-flow velocities in the proximity of the perimeter fan and as a result, one would expect the blade loading to be less. This is observed in Figure 57 as the windscreen reduces the blade loading for all cases except at $\beta = 0.26$ and $\beta = 0.36$ for both 50% and 75% covering. At very high cross-flows with a large portion of the inlet covered, enough flow seeps through the windscreen in such a way that the cross-flow velocity within the proximity of the perimeter fan is high enough to cause a significant variation in the *y*-velocity profiles of the up-and downstream halves of the fan causing an increase in the dynamic blade loading.

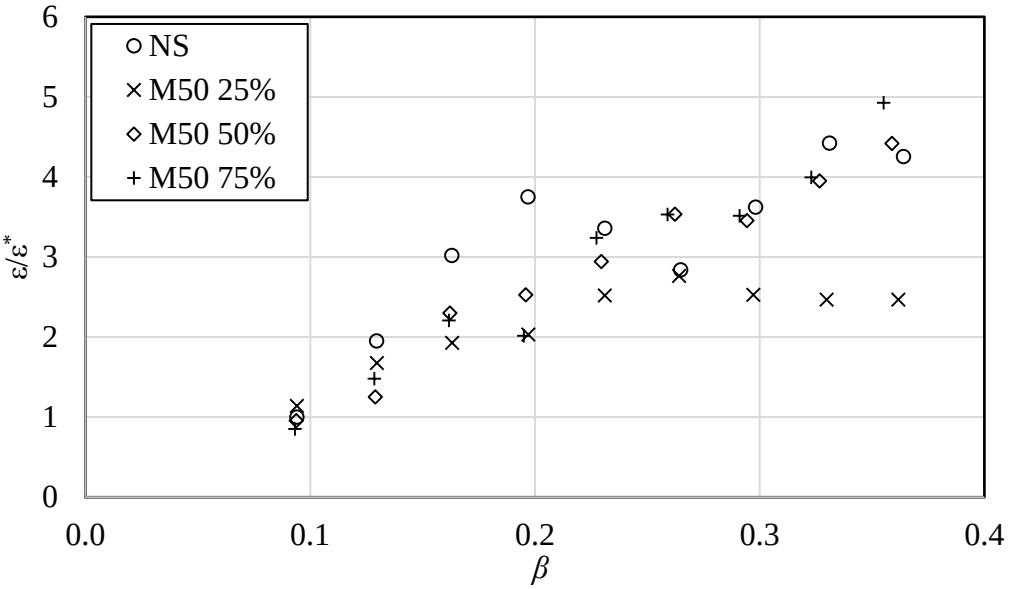

Figure 57: Normalized strain measurement with windscreen installed

Because there were good PIV results for $\beta = 0.2$ and $\beta = 0.33$ for differing screen covering percentages, as shown in Figure 55 and Figure 56, the *y*-velocity into the fan can be analysed in more detail. See Figure 58 and Figure 59 for the *y*-velocity into the perimeter fan along line-1 (as depicted in Figure 41, see Section 5.2.2), neglecting the data from the hub region, for cross-flows of $\beta = 0.2$ and $\beta = 0.33$ respectively.

For the lower cross-flow case of $\beta = 0.2$, it seems that having a windscreen present produces a more even *y*-velocity profile into the fan, with the exception of 25% covering where the flow that is deflected by the windscreen enters the fan at the downstream edge. At a cross-flow of $\beta = 0.2$, the presence of the windscreen, irrespective of the percentage covering, reduces the dynamic component of the

measured strain significantly. This should be attributed to the more even inflow (in terms of *y*-velocity observed in Figure 58) with the exception of 25%, which may be attributed to the slight discontinuity in the PIV data along the stitching line as indicated in Figure 55.

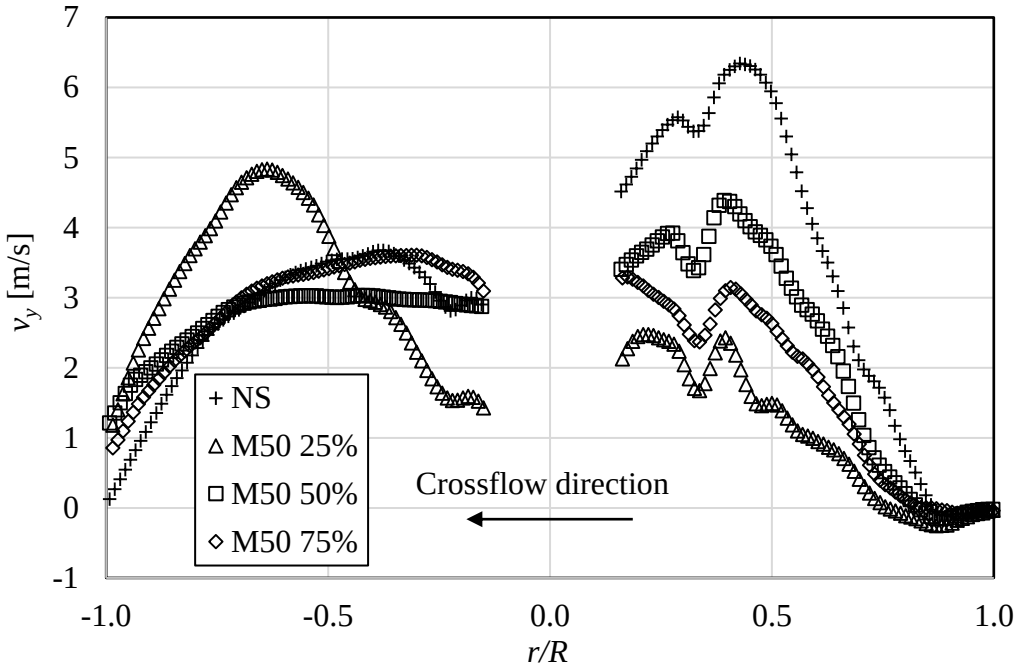

Figure 58: *y*-velocity into the fan 1 along line-1 at β = 0.2 with a windscreen installed

Figure 59 also shows the y velocity into the perimeter fan along line-1 (refer to Figure 41) but now for a higher cross-flow of β = 0.33. From this figure, one can see why the dynamic blade loading for both the 50% and 75% screen covering isn't significantly less than that of the no-screen case as the inlet velocity profiles are very similar. Only 25% covering has a significantly more even inlet profile, and this coincides with a smaller dynamic blade loading value. From these figures, it would seem that a contributing factor to the increase in dynamic blade loading, witnessed with the increase in cross-flow, is the difference in *y*-velocity profile between the upstream and downstream halves of the fan inlet. Using the results obtained from the PIV a comparison can be made between the differences in mean *y*-velocity into the up- and downstream half of the perimeter fan compared to the normalized bending strain (shown in Figure 60).

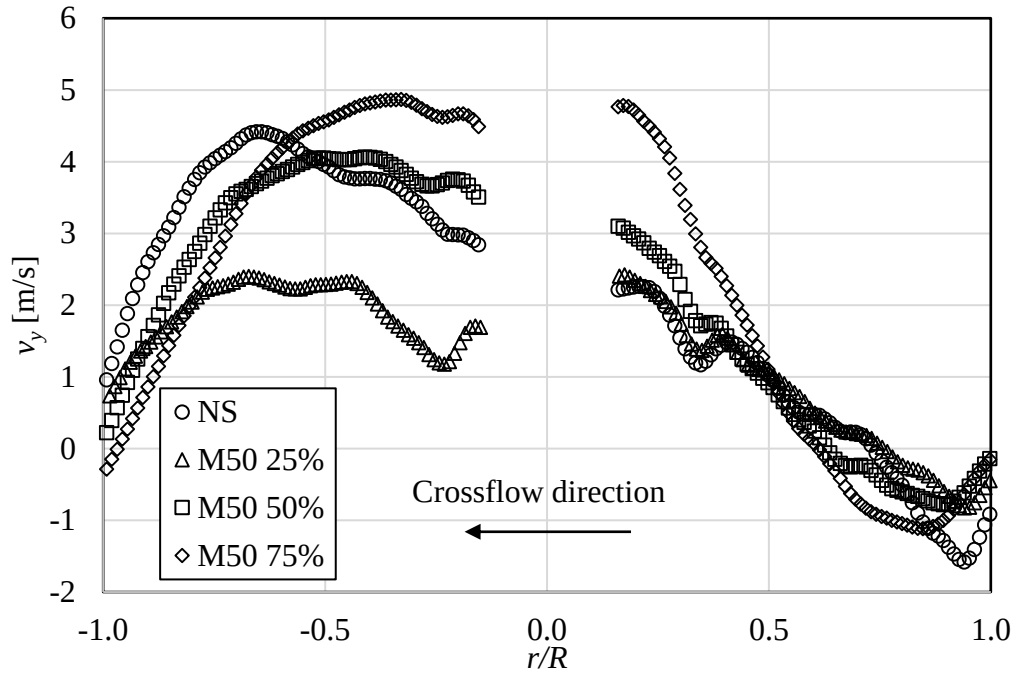

Figure 59: *y*-velocity into fan 1 along line-1 at β = 0.33 with a windscreen installed

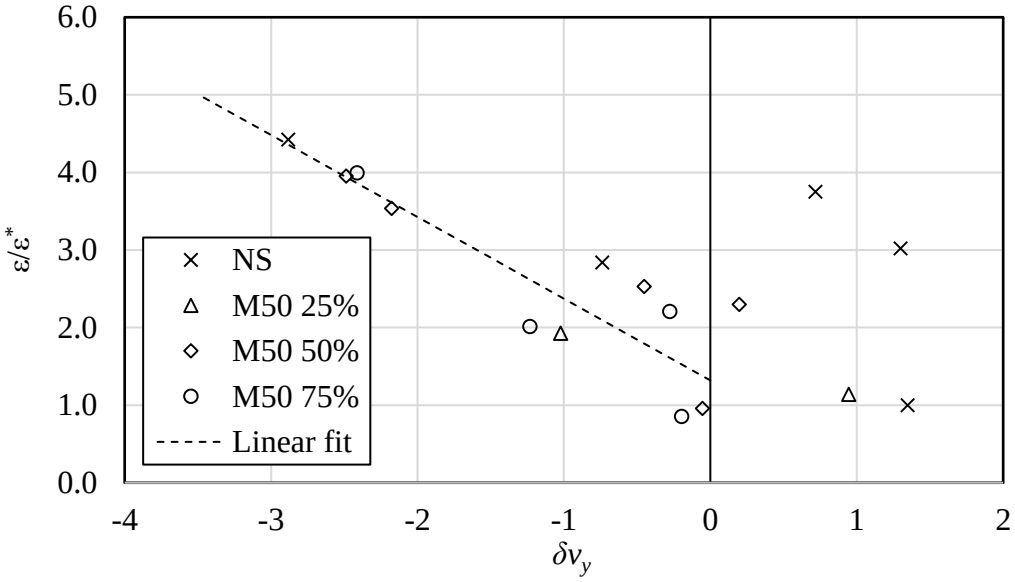

Figure 60: Relation between normalized strain and the differential *y*-velocity into the fan

Figure 60 shows that once the mean differential *y*-velocity is negative, the magnitude of this mean differential *y*-velocity exhibits a linear relation (given in Equation 15 with the normalized bending strain.

$$\varepsilon/\varepsilon^* = -1.05\delta\bar{v}_y + 1.32 \quad (15)$$

5.3.3 Perimeter fan performance and dynamic blade loading with M50, M60 and M75 windscreens

The perimeter fan's volumetric effectiveness with the installation of windscreens with differing solidity at 25%, 50% and 75% covering is shown in Figure 61, Figure 62 and Figure 63. All the data and standard deviations between repeated test are given in Appendix D.2 to Appendix D.4.

With the increasing solidity of the windscreen, the perimeter fan's performance suffers increasingly, although the downward performance trends on the perimeter fan are very similar for each of the three solidities. The reduction in the perimeter's fan performance with increasing solidities is due to the higher solidity windscreen (e.g. M75) offering more flow resistance and therefore more flow will be deflected below the screen and less will permeate through the screen than for the lower solidity screen (e.g. M50). This confirms then the reasoning behind the downward trends discussed in Section 5.3.1, on the fan performance with a M50 windscreen installed.

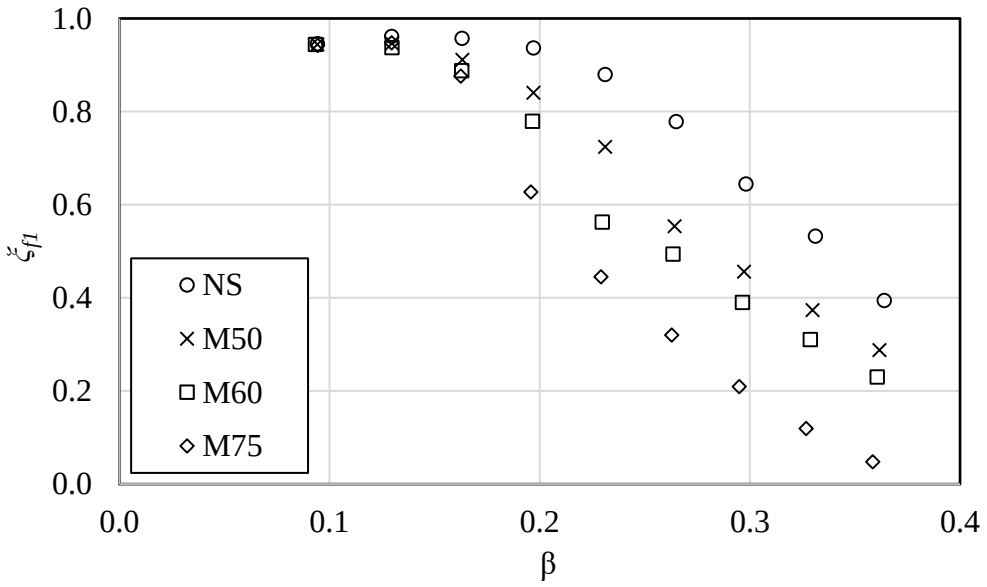

Figure 61: Fan 1 volumetric effectiveness with 25% of the inlet covered with screen

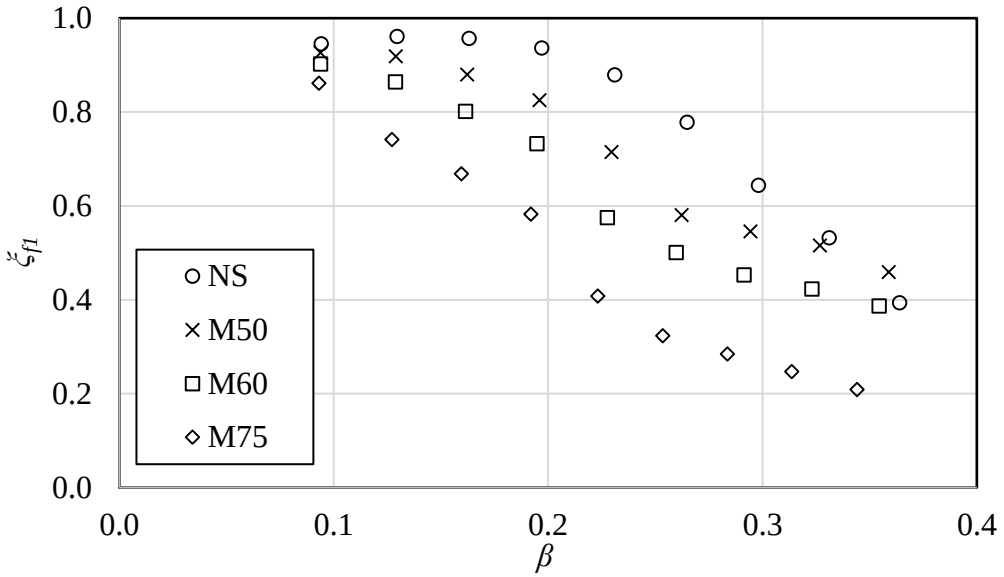

Figure 62: Fan 1 volumetric effectiveness with 50% of the inlet covered with screen

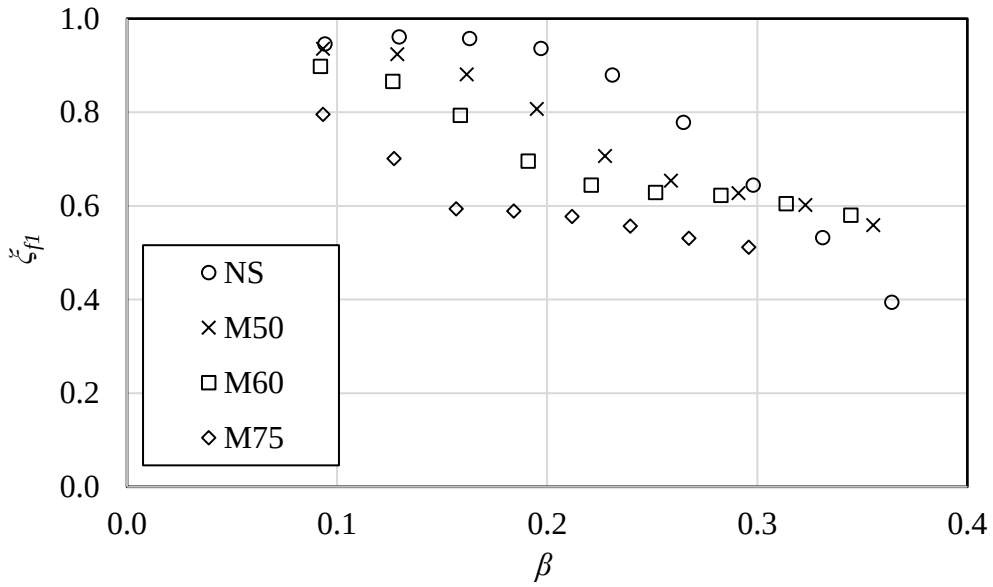

Figure 63: Fan 1 volumetric effectiveness with 75% of the inlet covered with screen

The dynamic blade loading of the perimeter fan with the installation of windscreens with differing solidity at 25%, 50% and 75% covering is given in Figure 64, Figure 65 and Figure 66.

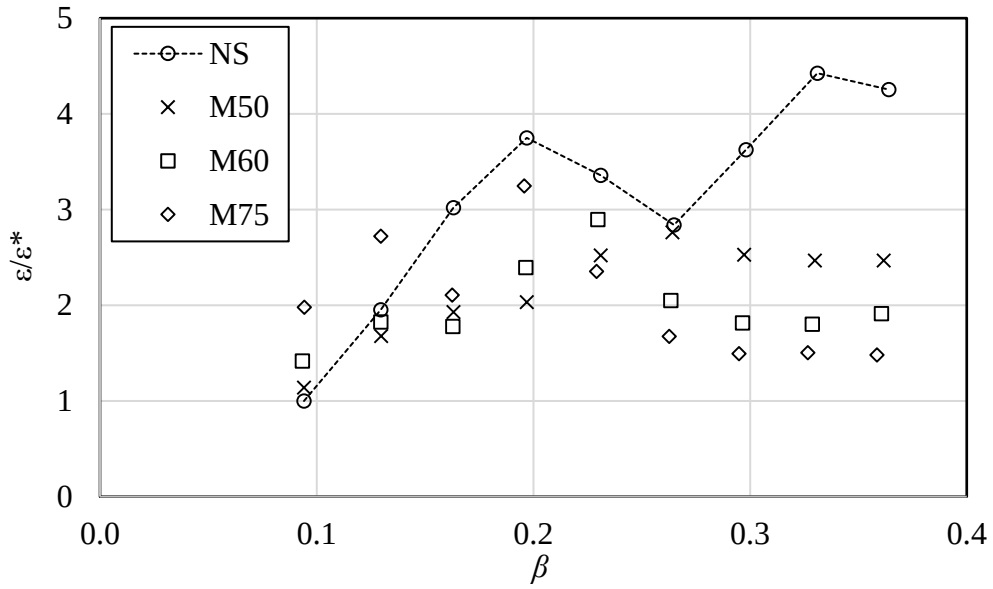

Figure 64: Fan1 normalized strain with 25% of the inlet covered with screen

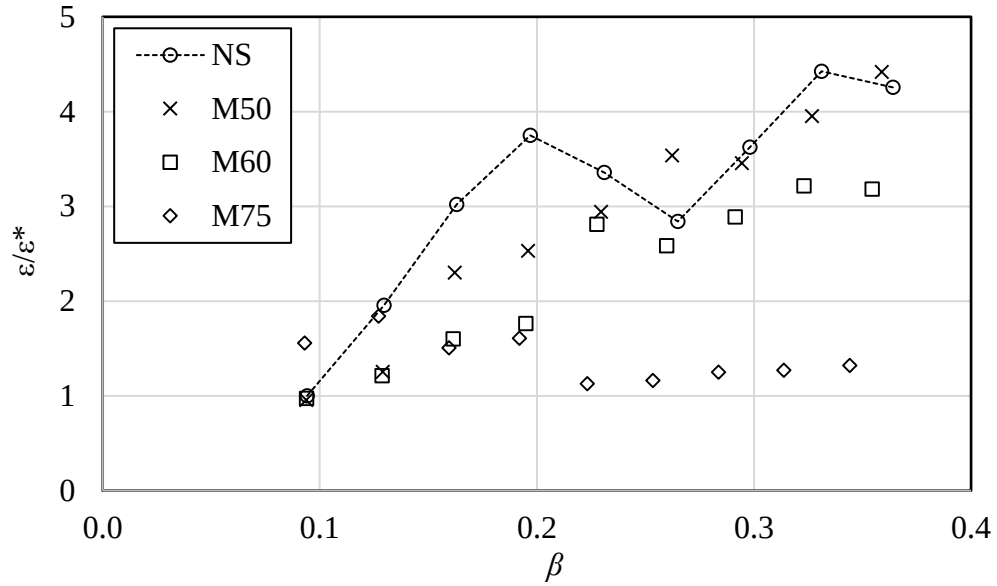

Figure 65: Fan 1 normalized strain with 50% of the inlet covered with screen

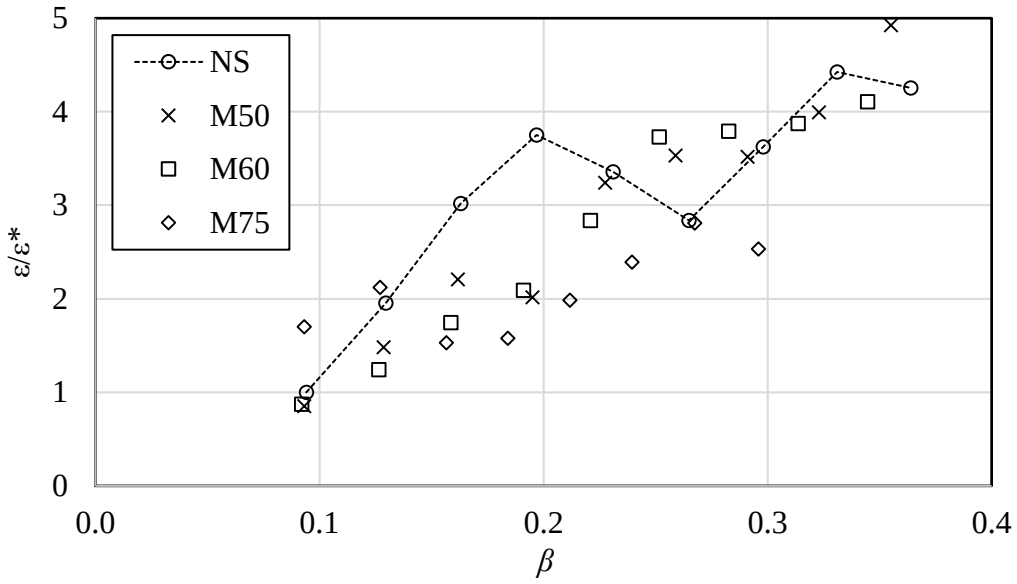

Figure 66: Fan 1 normalized strain with 75% of the inlet covered with screen

Decreasing the windscreen solidity seems to have a slight benefit in terms of reducing the dynamic blade loading. This statement however is not valid across the entire cross-flow range that was tested as can be seen in Figure 64 to Figure 66. No further comments can be made on these results as there are no PIV data available.

5.3.4 Full-scale comparison

As there is available data from Caithness Energy Center on the fan performance with M60 windscreens deployed at 25%, 50% and 75% of the inlet cover (Maulbetsch and DiFilippo, 2016), it was possible to make a comparison between the full-scale data and the data recorded using the scaled multiple fan test facility. Due to the presence of the windscreen at the upstream inlet adding an additional flow resistance and causing the fan row to be unsymmetrical the previously determined no-wind conditions do not apply. To determine an approximation for the wind speed in the multiple fan test facility, using Equation 13, it was required to determine the no-wind volume flow rate through each of the fan test sections as well as the no-wind volumetric cross-flow through the inlet where the windscreen was installed. The no-wind volume flow rate through each of the fan tests section was determined by measuring the flow rate through each test section without the inlet ducted connected, these are given in Table 6 as volumetric effectiveness and the no-screen volumetric effectiveness is given as reference.

Table 6: No-wind fan performance with M60 windscreen installed

	ξ_{f1}	ξ_{f2}	ξ_{f3}
NS	0.94	0.95	0.95
M60 25%	0.92	0.93	0.94
M60 50%	0.86	0.96	0.93
M60 75%	0.86	0.88	0.91

With the M60 windscreen installed the no-wind volumetric cross-flow rate through the upstream inlet would be less than when no windscreen was installed as the resistance caused by the windscreen results in more flow coming through the downstream inlet, causing the system to be unsymmetrical. This effect is also exacerbated by increasing the percentage of the inlet covered by the windscreen. The method used to determine the no-wind volumetric cross-flow rate for each of the percentage coverings was by determining the β value at which the volumetric effectiveness of the perimeter fan matched the value given in Table 6. Additional tests were conducted for $\beta < 0.1$ with the M60 screen installed at 25%, 50% and 75% covering. Analysis of these results allowed for the identification of the forced cross-flow magnitude (β) at which the fan volumetric effectiveness matched the no-wind case shown in Table 6. Table 7 presents these values. See Appendix D.7 for the additional test data used to determine the new no-wind β values for the M60 windscreen.

Table 7: No-wind β values with M60 windscreen installed

	NS	**M60 25%**	**M60 50%**	**M 60 75%**
β_{NW}	0.095	0.084	0.054	0.059

By using the data given in Table 6 and Table 7, Equation 13 could once more be used to approximate the wind speed.

Figure 67 and Figure 68 shows the volumetric effectiveness of the perimeter and second fan with a windscreen installed at different percentages of the inlet covered for both full-scale data from Caithness Energy Center (Maulbetsch and DiFilippo, 2016) and the scaled multiple fan test facility with the scaled facility's no-screen case data for reference.

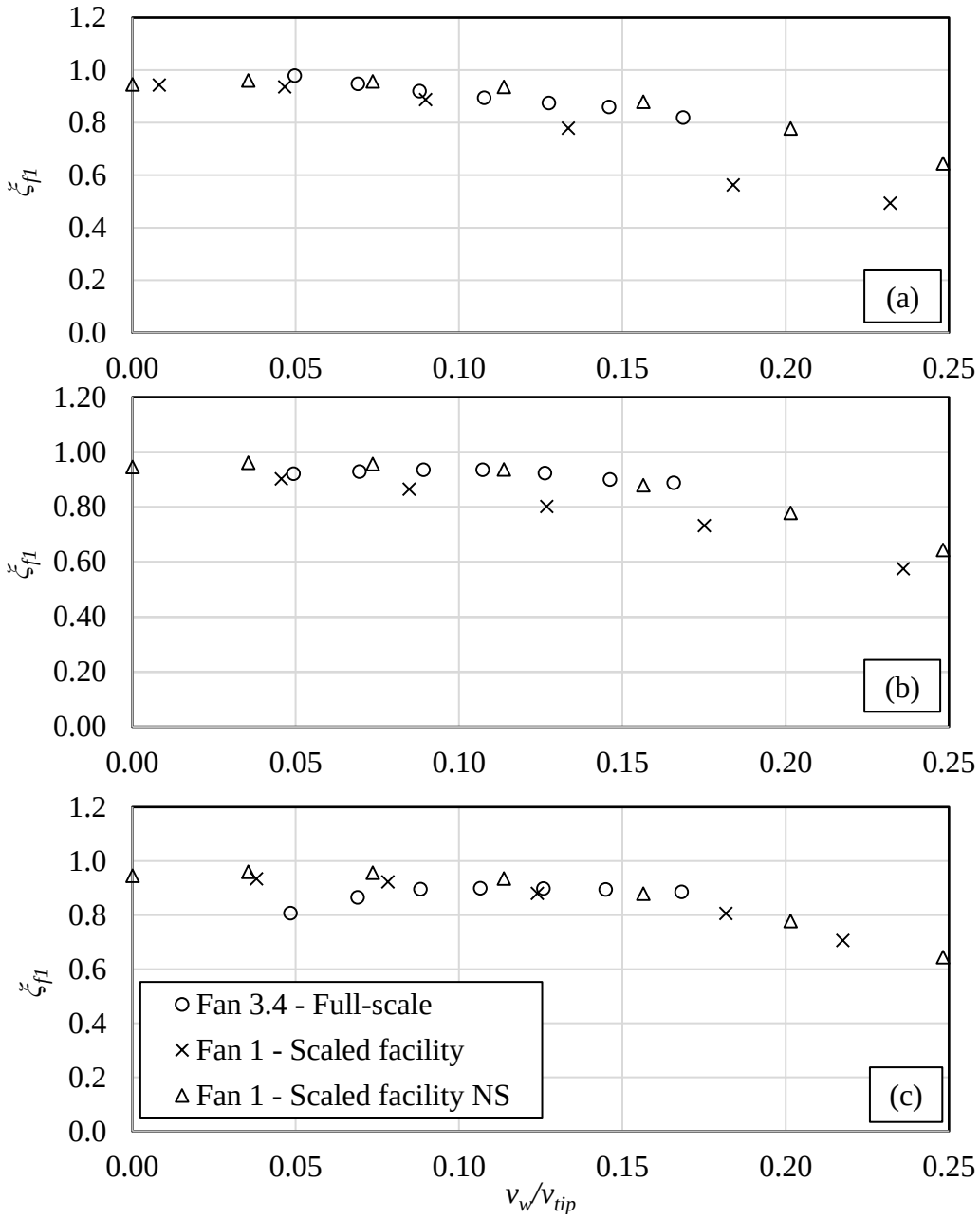

Figure 67: Comparison between scaled and full-scale volumetric effectiveness for the perimeter fan with M60 windscreen installed at (a) 25%, (b) 50% and (c) 75% of the inlet covered

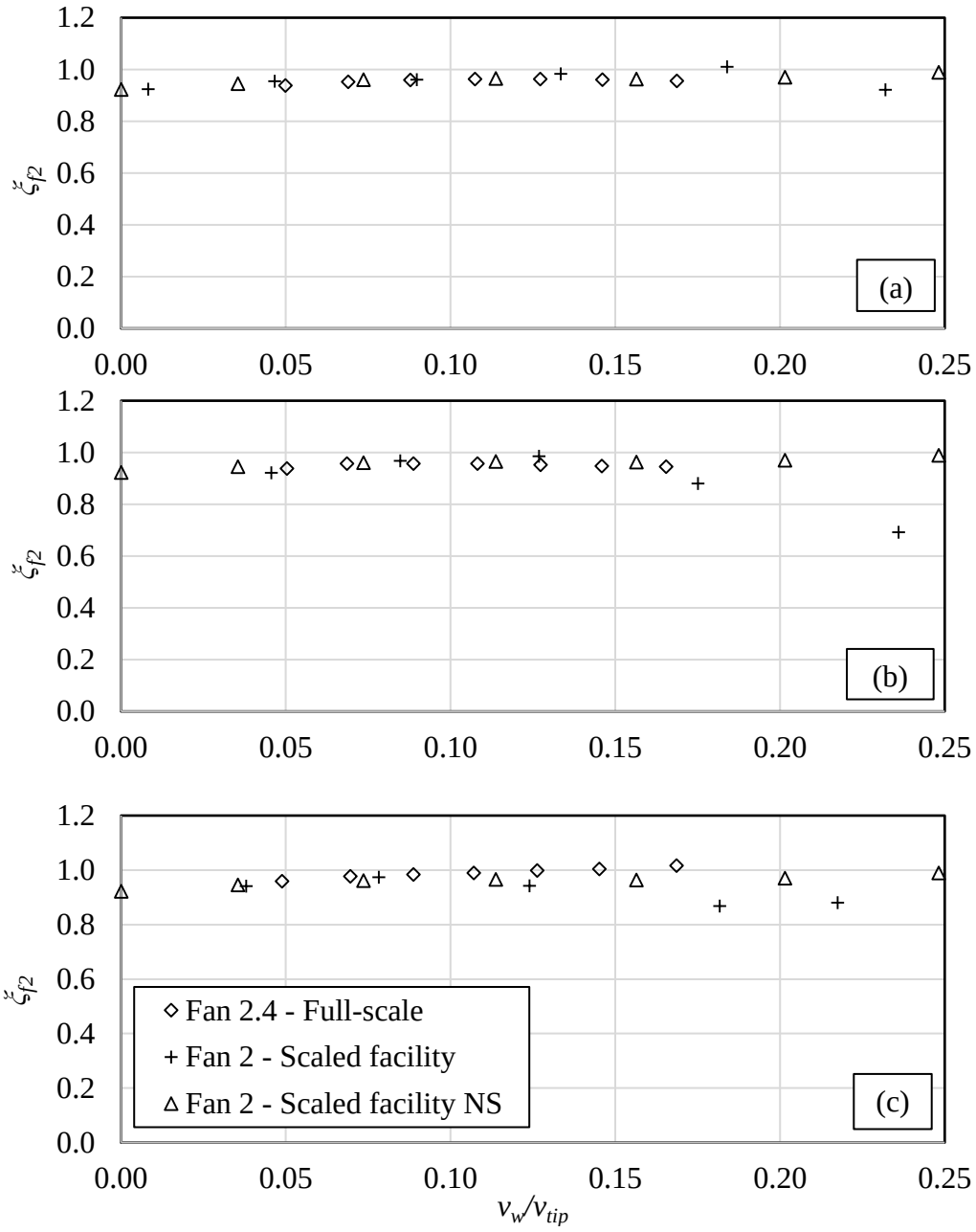

Figure 68: Comparison between scaled and full-scale volumetric effectiveness for the second fan with M60 windscreen installed at (a) 25%, (b) 50% and (c) 75% of the inlet covered

The performance trends of the two fans with a windscreen present do not have as good a correlation as without a windscreen, as given in Section 5.2.3. This is more so in the case of the perimeter fan than in the case of the second fan which is expected, as the perimeter fan would be more influenced by the presence of the windscreen. The scaled facility under predicts the fan performance, with a

windscreen installed, compared to full-scale. There are a number of reasons for this under-prediction, such as the wind direction of the full-scale data not being purely westerly, the full-scale facility having adjacent buildings influencing the in-flow, the scaled facility only consisting of a single fan row (because the scaled facility was designed based on the approximation that the incoming flow would be two-dimensional while in the full scale case the flow would not be two-dimensional due to the influence of adjacent fan rows and varying wind direction), the differences in the Reynolds numbers for the flow moving through the inlet area, the uncertainty with regards to the method used to estimate the scaled facility's wind speed at platform height and the windscreens not being geometrically scaled.

Considering the differences, the full-scale and scaled facility results indicate that the windscreen does not improve the volumetric effectiveness of the perimeter fan, apart from one or two cases where the full-scale data indicates a slight improvement when the windscreen covers a larger area. This same phenomenon was observed in the scaled facility's results where there was a slight improvement in the volumetric effectiveness of the perimeter fan above the no-screen case, once a larger area was covered with windscreen material, but only for very high cross-flow (refer to Section 5.3.3).

5.3.5 Summary

Based on both the recorded data of the fan's performance (in terms of volumetric effectiveness) and the PIV velocity vector field visualization, with a windscreen installed, the following observations were made:

1. The windscreen deflects the bulk of the incoming flow past the perimeter fan's inlet and the volume flow, that does move through the windscreen, is not enough. As a result, the perimeter fan's performance suffers.

2. As the cross-flow is increased the bulk air flow that is deflected by the windscreen shifts downstream away from the perimeter fan. This initially benefits the second and third fans but as the nature of the deflection changes with increasing cross-flow, this becomes reversed, especially so for the second fan.

3. At high cross-flow ($\beta = 0.36$) there is enough permeation through the windscreen so that when a larger percentage of the inlet is covered by screens, the fans receive enough flow through the screens and simultaneously benefit from reduced inlet flow distortions. The result is an increase in fan performance, relative to the no-screen case.

4. The cross-flow that does move through the windscreen has a reduced x-velocity component, this results in a more evenly distributed y-velocity profile, along with the span of the blade, for both the up-and downstream halves of the perimeter fan. This reduces the variation in aerodynamic loading on the up- and downstream halves and therefore the dynamic blade loading is reduced.

6 Conclusion

The objectives set for this study were to modify the existing multiple fan test facility such that the fan row could be exposed to a controllable cross-flow, to simulate a wind, at a fixed platform height. This modified facility was then to be used to investigate the effect that increasing cross-flow has on fan performance and dynamic blade loading of the perimeter fan with and without the installation of a windscreen. Finally, the flow field in the vicinity of the perimeter fan with and without a windscreen under increasing cross-flow conditions was to be visualized to aid in the understanding of the results.

The original multiple fan test facility was modified to allow for a controllable cross-flow at fixed platform height by ducting the outlet flow from an open circuit wind tunnel to the inlet chamber of the three fan test sections. These modifications were deemed valid based on three aspects: firstly, by making use of CFD to investigate how having a ducted-inlet would affect the fan performance and inlet flow profiles compared to a free-inlet. Secondly, by comparing the system volumetric effectiveness of the fan row with that predicted using Equation 7. Lastly, by comparing the perimeter fan and second fan's performance to full-scale experimental results recorded at Caithness Energy Center by Maulbetsch and DiFillipo (2016). The CFD indicated that having a ducted-inlet would cause noticeable differences in the inlet conditions observed at a free-inlet ACC fan row, as the point at which the incoming flow diverges along the wind-wall changes with increasing inlet velocity. These differences could be negated by comparing the fan performance of a free-inlet fan row to a ducted-inlet fan row based on similar average cross-flow velocities. This was again confirmed, as a good correlation between Equation 7 and the experimentally recorded system volumetric effectiveness was achieved when the two were compared based on average cross-flow velocities. Finally using Equation 13 to approximate the wind speed at platform height, a good correlation was achieved between fan performance, recorded at Caithness, for the perimeter fan and second fan to that measured at the scaled multiple fan test facility. As such the modifications were deemed adequate and the problem of not achieving dynamic similarity (between the scaled and the full-scale facility) could be ignored as irrespective of the dynamic differences, similar performance trends, between the scaled and full-scale facility, under cross-flow conditions were observed (refer to section 5.2.3).

The investigation done on fan performance and dynamic blade loading under cross-flow conditions with no windscreen present yielded results that correspond well to those seen in previous studies. The separation region forming on the upstream edge of the bellmouth was identified as the main reason for the dramatic reduction in fan volumetric effectiveness. The presence of the separation region caused a significant difference in the *y*-velocity profiles into the up- and downstream halves of the perimeter fan. This would cause a variation in the aerodynamic loading of the blade within one rotation and was subsequently identified as one of the sources for the increased dynamic blade loading observed as the cross-flow was increased.

With the presence of the windscreen, the perimeter fan's performance in terms of volumetric effectiveness was generally worse, except at very high cross-flows with a large percentage of the inlet covered. This was due to the windscreen deflecting the majority of the flow into the second and third fans, depending on the percentage of the inlet covered, and the flow that did permeate through the screen not being sufficient to support a performance increase. With a large percentage of the inlet covered at very high cross-flow, enough flow moves through the windscreen to account for a slight performance increase in the perimeter fan, above the no-screen case. As mentioned, the windscreen reduces the magnitude of the cross-flow velocity at the inlet of the perimeter fan and this contributes to lowering the dynamic blade loading by creating a more even *y*-velocity inlet profile between the up- and downstream halves of the fan's inlet. Once this cross-flow velocity increases to the point where a significant difference in the *y*-velocity profiles exists, the dynamic blade loading would increase even to the point of exceeding the measurements observed when no windscreen was installed. These conclusions could be made as the PIV yielded good visualizations of the flow near the inlet of the perimeter fan, and subsequently, the measured fan performance and dynamic blade loading could be analysed based on flow phenomena.

The results recorded using the multiple fan test facility indicates that the presence of a windscreen, irrespective of the solidity or percentage of the inlet covered, generally tends to worsen the performance of the perimeter fan. This finding contradicts what was reported in previously observed CFD studies available in the literature (see Section 2.2). The result does however show similar trends to that observed in the full-scale tests done by Maulbetsch and DiFilippo (2016). Their results indicated that the presence of the windscreen tends to negatively affect the perimeter fan's performance except at higher wind speeds with a larger percentage of the inlet covered with a windscreen, and also indicated a slight improvement in the second fans performance (see Section 2.2 and 5.3.4). This is exactly what was observed in the scaled facility although comparing the two, based on an estimated wind speed, the scaled facility does under predict the perimeter fan's performance slightly.

Although this study indicates that windscreens are in fact not beneficial for fan performance under cross-flow in this case, one cannot conclude that windscreens would negatively affect fan performance at all ACC facilities. This study is based on Caithness Energy Center's ACC dimensionality, which has a relatively low dimensionless platform height (H/d_f). Windscreens could potentially be more beneficial for facilities with a larger dimensionless platform height where for the same ratio of windscreen height to fan diameter, a facility like this would have less overall blockage. This could change the nature of the deflection and potentially lead to performance increases. The influence that differing platform heights with various windscreen coverings have on fan and ACC performance, deserves further attention. This is however not suited for an experimental study due to the increasing number of parameters but would be ideally suited for CFD simulation where the results within this study could be used as validation.

References

Augustyn, O. P. H. (2013). *Experimental and numerical analysis of axial flow fans*, Master's thesis, University of Stellenbosch.

Barker, B. (2007). 'Running Dry at the Power Plant', *EPRI Summer Journal*, pp. 26–35.

Bechhoefer, E. and Kingsley, M. (2009). 'A review of time synchronous average algorithms', *Prognostics and Health Mangement Society*, pp. 1–10..

Bredell, J. R., Kröger, D. G. and Thiart, G. D. (2006). 'Numerical investigation of fan performance in a forced draft air-cooled steam condenser', *Applied Thermal Engineering*, vol. 26, pp. 846–852.

Bruneau, P. (1994). *The design of a single rotot axial flow fan for a cooling tower application*. Master's thesis, University of Stellenbosch.

Cengel, Y. A. and Boles, M. A. (2011). *Thermodynamics an engineering approach*. 7th ed. Singapore: McGraw-Hill.

Conradie, P. (2010). *Edge fan performance in air-cooled condensers*. Master's thesis, University of Stellenbosch

DiFilippo, M. (2008). *Reclaiming Water for Cooling at SCE's Mountainview Power Plant.* Presentation: EPRI workshop on Advanced Thermoelectric Cooling Technologies, Charlotte.

Dudgeon, D. *et al.* (2006). 'Freshwater biodiversity: importance, threats, status and conservation challenges', *Biological Reviews*, 81(02), p. 163.

Duvenhage, K. and Kröger, D. G. (1996). 'The influence of wind on the performance of forced draught air-cooled heat exchangers', *Journal of Wind Engineering and Industrial Aerodynamics*, 62(2–3), pp. 259–277

Fluent (2017). 'Ansys Fluent 12.0 User Guide' ANSYS, Inc.

Fourie, N. (2014). *Simulating the effect of wind on the performance of axial flow fans in air-cooled steam condenser systems*. Master's thesis, University of Stellenbosch.

Gadhamshetty, V. *et al.* (2006). 'Improving Air-Cooled Condenser Performance in Combined Cycle Power Plants', *Journal of Engineering Energy*, 132(2), pp. 81–88.

Gao, X. F. *et al.* (2010). 'Performance prediction of an improved air-cooled steam condenser with deflector under strong wind', *Applied Thermal Engineering*, 30(17–18), pp. 2663–2669.

Inman, D. J. (2009). *Engineering vibrations*. 3rd ed. Upper Saddle River: Pearsons Education.

International Standards Office. (2007). ISO 5801 - Industrial fans: Performance testing using standardized airways.

Kröger, D. G. (2004). *Air-cooled Heat Exchangers and Cooling Towers*. Penwell Corporation, Tulsa, USA.

Louw, F. G. (2011). *Performance Trends of a Large Air-Cooled Steam Condenser during Windy Conditions.* Master's thesis, University of Stellenbosch

Maulbetsch, J. S. and DiFilippo, M. N. (2008). *Effect of Wind Speed and Direction on the Performance of Air-Cooled Condensers*. California Energy Commission. Publication Number: CEC-500-2013-065-APB.

Maulbetsch, J. S. and DiFilippo, M. N. (2016). *The Use of Wind Barriers to Mitigate the Effect of Wind on Air-Cooled Condensers*. California Energy Commission. Publication number: CEC-500-2016-047.

Muiyser, J. *et al.* (2016). 'Analysis of vibration inducing sources of a large-scale cooling system fan blade'. Conference: 10th South African Conference on Computational and Applied Mechanics, Potchefstroom

Owen, M. T. F. and Kröger, D. G. (2010). 'An Investigation of Air-Cooled Steam Windy Conditions Using Computational Fluid Dynamics', 133(June 2011), pp. 1–4.

Salta, C. A. and Kröger, D. G. (1995). 'Effect of inlet flow distortions on fan performance in forced draught air-cooled heat exchangers', *Heat Recovery Systems and CHP*, 15(6), pp. 555–561.

Touma, J. S. (1977). 'Dependence of the wind profile power law on stability for various locations', *Journal of the Air Pollution Control Association*, 27(9), pp. 863–866.

Turner, J. T. (1975). The aerodynamics of forced-draught air-cooled heat exchangers. International Symp. on Cooling Systems, BHRA Fluid.

van der Spuy, S. J. (2011). *Perimeter fan performance in forced draught air-cooled steam condensers.* Ph.D. thesis, University of Stellenbosch.

van Rooyen, J. A. (2007). *Performance trends of an air-cooled steam condenser under windy conditions*. Master's thesis, University of Stellenbosch.

Visser, J. G. J. (1990). *Die invloed van versteurde inlaatvloeipatrone op aksiaalwaaiers*. Master's thesis, University of Stellenbosch.

Zhang, X. and Chen, H. (2015). 'Effects of windbreak mesh on thermo-flow characteristics of air-cooled steam condenser under windy conditions', *Applied Thermal Engineering*. Elsevier Ltd, 85, pp. 21–32.

Appendix A Calibration

All measurement equipment used was calibrated beforehand, each calibration procedure and curve are given in this Appendix.

A.1 Reference anemometer

Each of the anemometers of the fan test facility was calibrated using a reference anemometer that had been calibrated in an atmospheric open loop induced draft wind tunnel, shown in Figure A.1. The reference anemometer was clamped to the intake of the wind tunnel. The mass flow rate through the wind tunnel was calculated from the pressure drop across the epileptic nozzles (indicated by number 7). The mass flow rate through the wind tunnel can be adjusted by either increasing the speed of the radial fan (indicated by number 8) or changing the diameter of the nozzle.

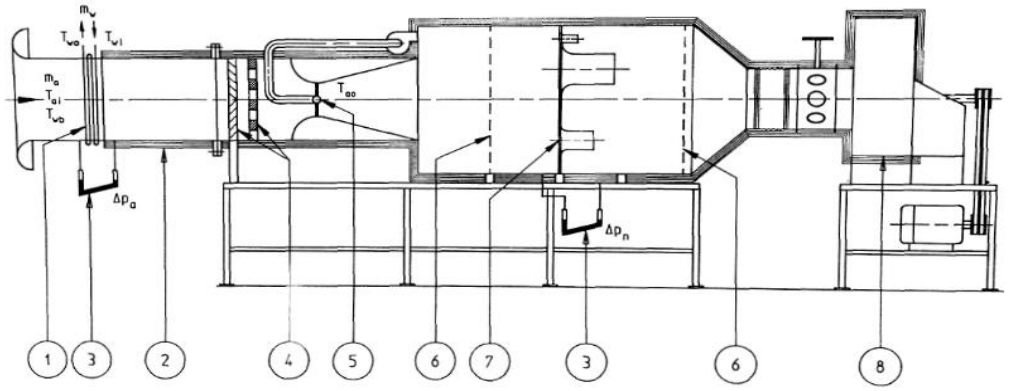

Figure A.1: Induced draft wind tunnel (Kröger, 2004)

The mass flow rate through the wind tunnel is calculated using Equation A.1.

$$\dot{m} = C_n \phi_g Y A_n \sqrt{2\rho_n \Delta p_n} \tag{A.1}$$

where C_n is the nozzle discharge coefficient and can be calculated using the following correlations:

For $30000 < Re < 100000$

$$C_n = 0.954803 + 6.37817 \times 10^{-7} Re_n - 4.65394 \times 10^{-12} Re_n^2 + 1.33514 \times 10^{-17} Re_n^3 \tag{A.2}$$

for $100000 < Re < 350000$

$$C_n = 0.9758 + 1.08 \times 10^{-7} Re_n - 1.6 \times^{-13} Re_n^2 \tag{A.3}$$

and for $R_n > 350000$, $C_n = 0.994$

where R_n is the Reynolds of the flow moving through the nozzle.

The gas expansion factor (ϕ_g) is approximated by

$$\phi_g = 1 - 3\Delta p_n / \left(4 p_{up}\, c_p / c_v\right) \qquad \text{(A.4)}$$

where p_{up} is the upstream pressure and Δp_n is the pressure drop across the nozzle and c_p/c_v = 1.4 for air.

Because the nozzle discharge coefficient is dependent on the Reynolds number Equation A.1 must be iteratively solved. The pressure difference across the nozzle as well as the upstream pressure were measured using Endress and Hauser pressure transducers and were calibrated beforehand using Betz Manometer. The calibration curves are given in Figure A.2, where Ch18 is for the upstream pressure measurement and Ch19 for the pressure drop across the nozzle.

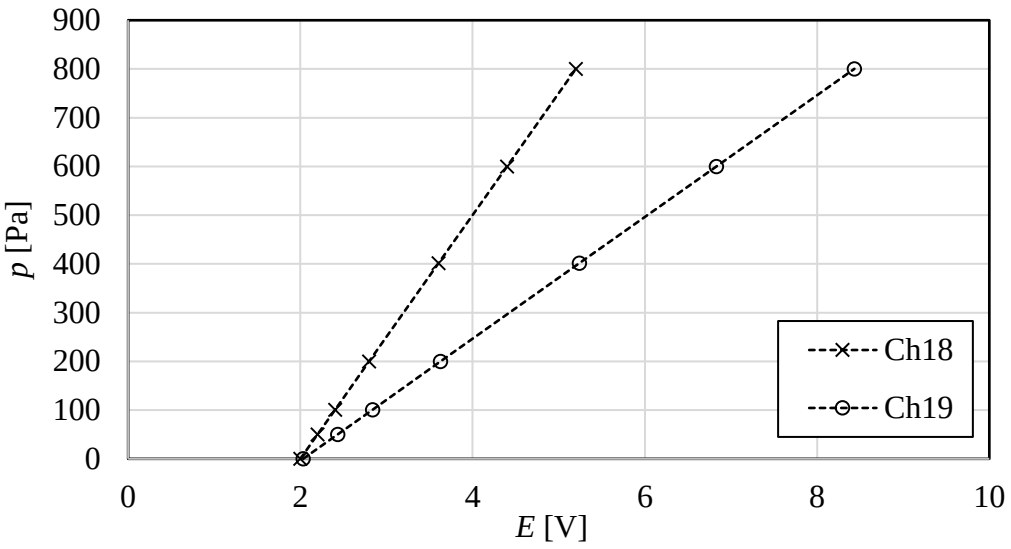

Figure A.2: Calibration curve for wind tunnel pressure transducers

The linear calibration curves are given by the following equations:

$$p_{18} = 250E_{18} - 499.9 \qquad R^2 = 1 \qquad \text{(A.5)}$$

$$p_{19} = 125E_{19} - 253.8 \qquad R^2 = 1 \qquad \text{(A.6)}$$

The output from the two pressure transducers as well as the output from a thermocouple measuring the atmospheric temperature were logged on Schlumberger data logger. The output of each of these measurement devices can then be used to calculate the flow rate through the wind tunnel as well as the

reference anemometer. The voltage output from the reference anemometer was measured on a multimeter with an averaging function, the average voltage output across one minute was recorded, this data was used to draw up the calibration curve given in Figure A.3.

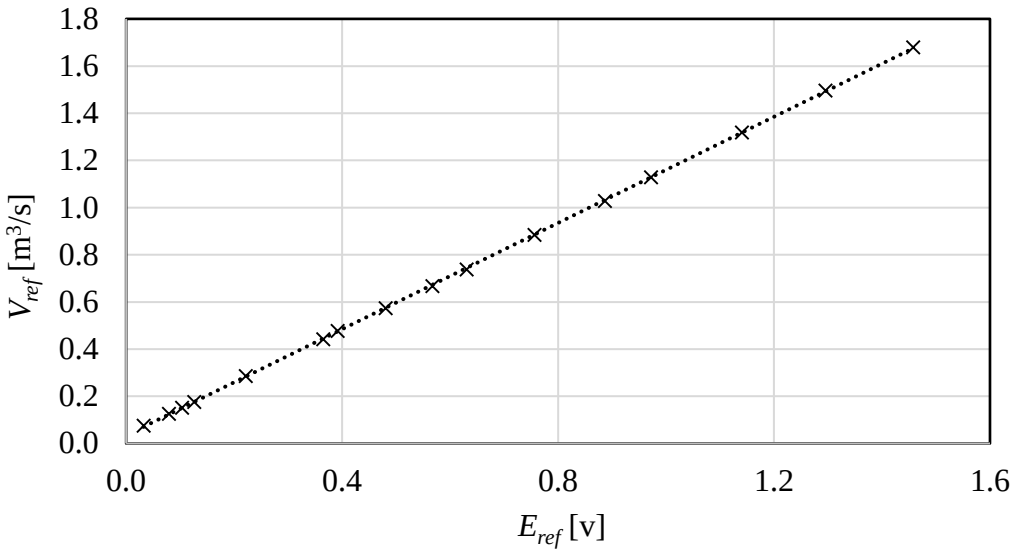

Figure A.3: Reference anemometer calibration curve

The linear calibration curve for the reference anemometer is given by:

$$V_{ref} = 1.126E_{ref} + 0.034 \qquad R^2 = 1 \tag{A.7}$$

A.2 Anemometer calibration

With the reference anemometer calibrated each of the test sections' anemometers could be calibrated by clamping the reference anemometer section to the outlet of each of the fan test section and running the fan at different rotational speeds. The addition of the reference anemometer adds an extra flow resistance to the system. To overcome this a booster fan was attach to the outlet of the reference anemometer. For each calibration point, the system was left to stabilize for two minutes before the voltage output from the anemometers was logged on the National Instrument data logger. To determine the standard deviation of the calibration procedure, 4 calibration points were repeated 3 times to determine the standard deviation between the 4, the maximum standard deviation (σ_{max}) across these 4 points for each of the 3 anemometers (a) were σ_{max} = 0.009 m^3/s for a_1, σ_{max} = 0.008 m^3/s, for a_2 and σ_{max} = 0.01 m^3/s for a_3. The calibration curves are given in Figure A.4 (the numeric subscripts refer to fan test section, 1 would be the perimeter fan).

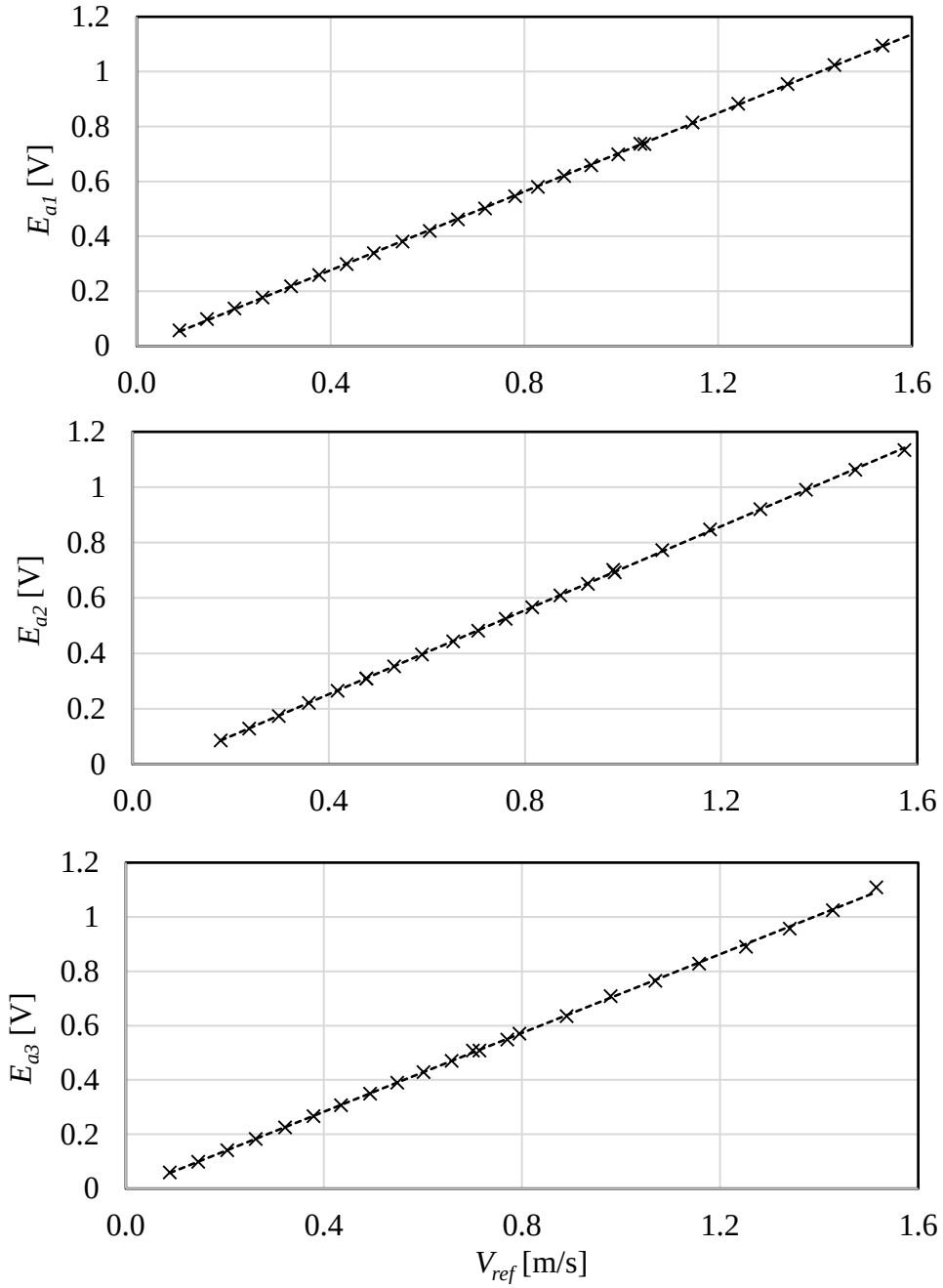

Figure A.4: Anemometer calibration curves

The linear calibration curves are given by:

$$V_1 = 1.396E_{a1} + 0.014 \qquad R^2 = 1 \tag{A.8}$$

$$V_2 = 1.319E_{a2} + 0.067 \qquad R^2 = 1 \tag{A.9}$$

$$V_3 = 1.379E_{a3} + 0.009 \qquad R^2 = 1 \tag{A.10}$$

A.3 Pressure transducers

The pressure transducers used to measure the static pressure in each of the plenum chambers were AutoTran Model 860, each of these transducers had to be calibrated. The operating range for these transducers are 0-1000 Pa (with an accuracy of ± 1 Pa) with a voltage output of 1-10 VDC. The calibration was done using a Betz manometer for reference, at each calibration point the output voltage was logged using the DAQ and compared with the manometer's value. The maximum standard deviation (σ_{max}) across the 4 calibration points for the AutoTran pressure transducers were σ_{max} = 1.7 Pa for p_1, σ_{max} = 2.2 Pa for p_2 and σ_{max} = 1.4 Pa for p_3. The calibrations curves are given in Figure A.5.

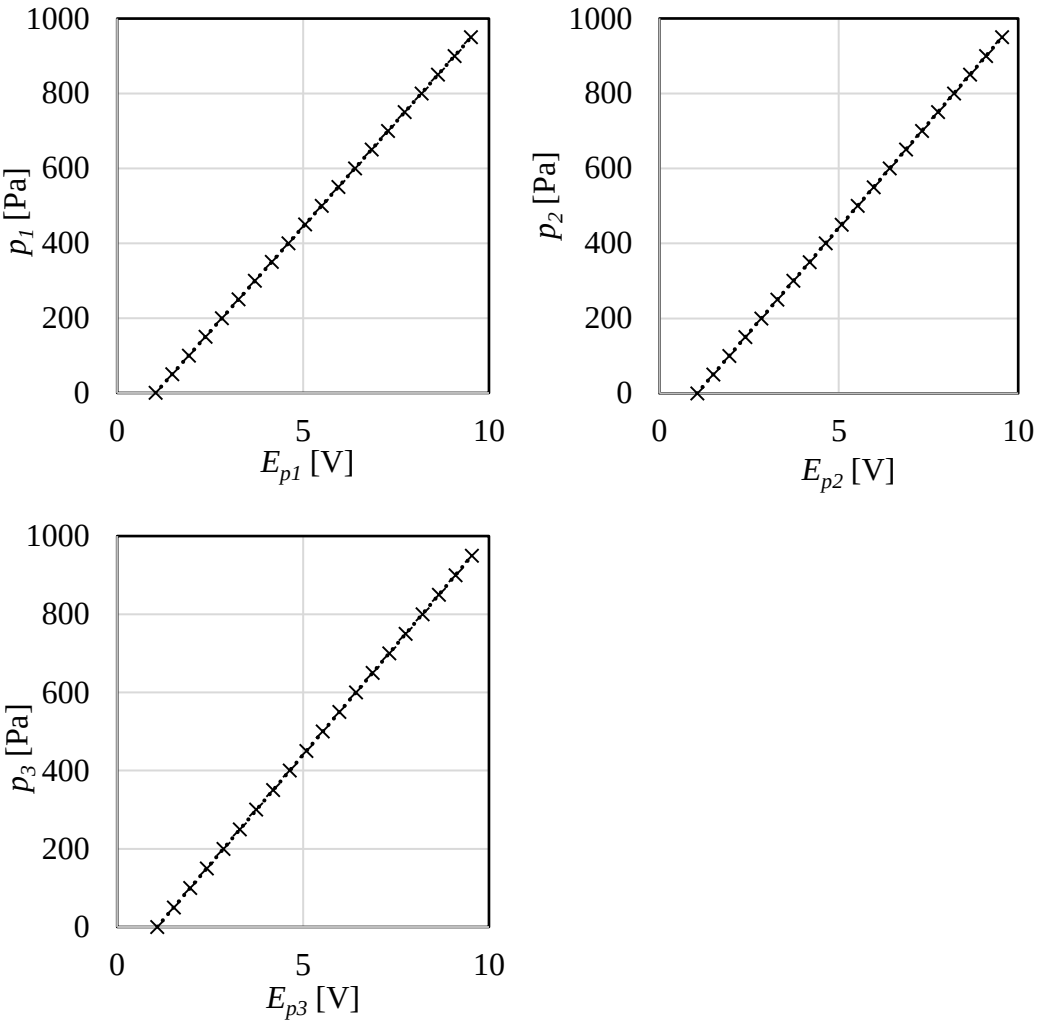

Figure A.5: AutoTran Model 860 pressure transducer calibration curves

The linear calibration curves are given by:

$$P_1 = 111.91E_{p1} - 115.52 \qquad R^2 = 1 \qquad \text{(A.11)}$$

$$P_2 = 111.71E_{p2} - 116.96 \qquad R^2 = 1 \qquad \text{(A.12)}$$

$$P_3 = 112.15E_{p3} - 120.46 \qquad R^2 = 1 \qquad \text{(A.13)}$$

The pitot tube differential pressure was measured using Endress & Hauser Deltabar S pressure transducer. Endress & Hauser transducer was used as the measuring range on this transducer is adjustable. The calibration procedure was the same as for the AutoTran Model 860. The pitot tube that was used in the wind tunnel's test section's pressure transducer's calibration curve is given in Figure A.6, the transducer's range was set to 0-1000 Pa with an accuracy of 1% across that range (p_W is the pressure reading for this transducer). While the pitot tube's pressure transducer that was used for the traverse of the inlet area is also given in Figure A.6, this transducer's range was set to 0-200 Pa with an accuracy of 1% across that range, this was required as the velocities at the inlet chamber was substantially lower than that in the wind tunnel test section (larger area) as such the differential pressure measurement were smaller as well (p_T is the pressure reading for this transducer). The maximum standard deviation across the 4 repeated calibration points were σ_{max} = 1.9 Pa for p_W and σ_{max} = 3.1 Pa for p_T

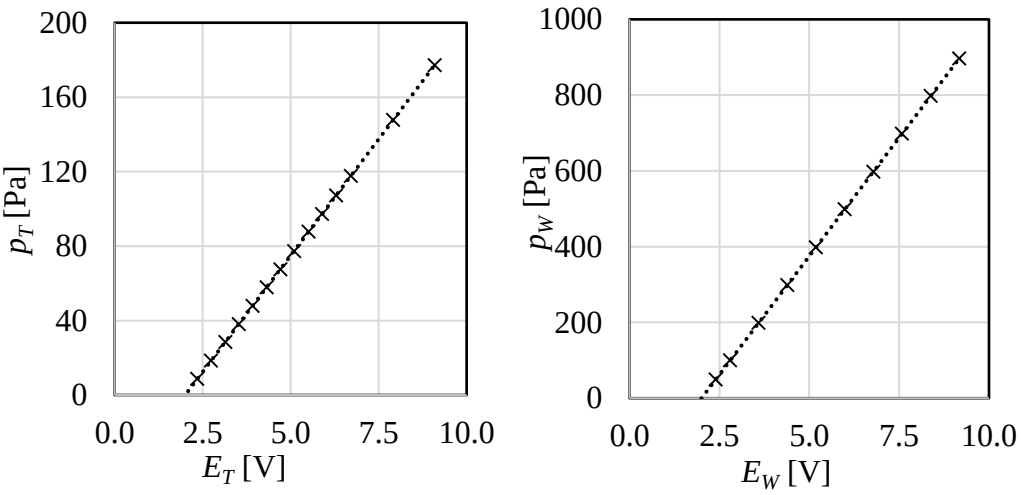

Figure A.6: Endress & Hauser pressure transducer calibration

The linear calibration curves are given by:

$$p_T = 25E_T - 50.1 \qquad R^2 = 1 \qquad \text{(A.14)}$$

$$p_W = 125.05E_W - 250.42 \qquad R^2 = 1 \qquad \text{(A.15)}$$

A.4 Speed sensor

The rotational speed of the fans was measured using a magnetic pickup sensor. The stationary magnetic pickup generates an electrical output as the ferrous cog teeth, that is fixed to the shaft, move through the magnetic field. The pickup device was calibrated using a stroboscope, the actual rotational speed was determined using the stroboscope whereas the voltage output from the speed sensor was logged using the National instrument DAQ. Figure A.7 shows the calibration curves for each of the 3 speed sensors, the calibration for the speed sensor was only started at 300rpm as at low rotational speeds the sensors did not exhibit a linear relationship between rpm and voltage. The third sensor's calibration could only be done from 800 rpm as at lower rotational speeds the sensor did not have a linear relation. The maximum standard deviation across the 4 repeated calibration points were σ_{max} = 1.8 rpm for N_1, σ_{max} = 2.4 rpm for N_2 and σ_{max} = 2.4 rpm for N_3. The calibration curves are given in Figure A.7.

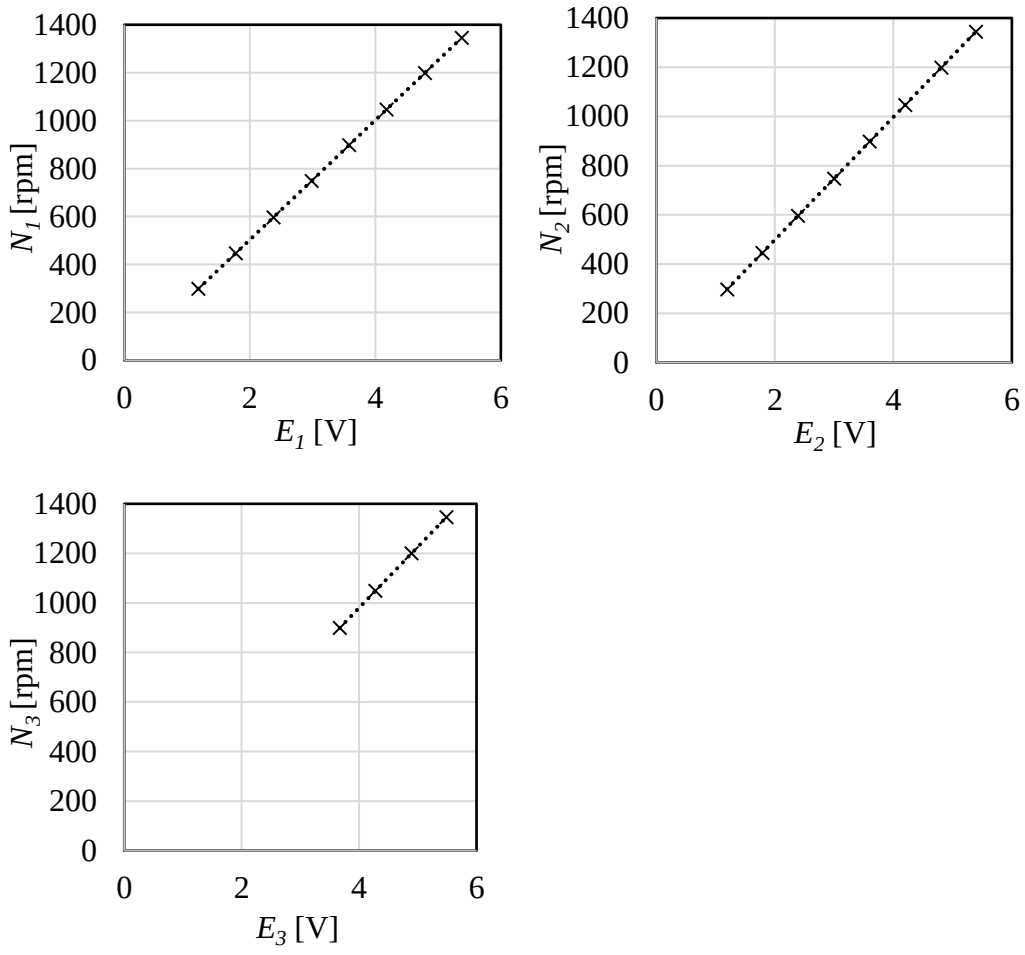

Figure A.7: Speed sensors calibration

The linear calibration curves are given by:

$$N_1 = 249.6E_1 + 3.63 \qquad R^2 = 1 \qquad \text{(A.16)}$$

$$N_2 = 249.23E_2 + 0.45 \qquad R^2 = 1 \qquad \text{(A.17)}$$

$$N_3 = 245.95E_3 - 3.69 \qquad R^2 = 1 \qquad \text{(A.18)}$$

A.5 Torque transducer

Only the perimeter fan's test section has a torque transducer that was calibrated using a moment arm attached to the fan's axial and placing weights at the end to subject the axis to a torque, as depicted in Figure A.8. The torque subjected to the axis can be calculated using Equation A.19 where the angle (θ) was measured using a digital level. The torque transducer used was an HBM T5 20 N·m, the output of the transducer was amplified using a Spyder-8 bridge amplifier and the data was recorded on Catman Easy software. The maximum standard deviation across the 4 repeated calibration points was σ_{max} = 0.07 N.m. The calibration curve is given in Figure A.9.

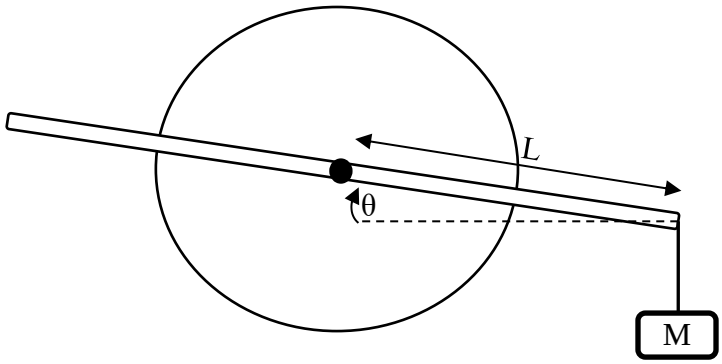

Figure A.8: Torque measurement

$$T_R = g \cdot M \cdot L \cdot \cos(\theta) \qquad \text{(A.19)}$$

where g is the gravitational constant, M is the mass applied to the moment arm, L is the length of the moment arm and θ is the angle of the moment arm relative to a horizontal axis as indicated in Figure A.8.

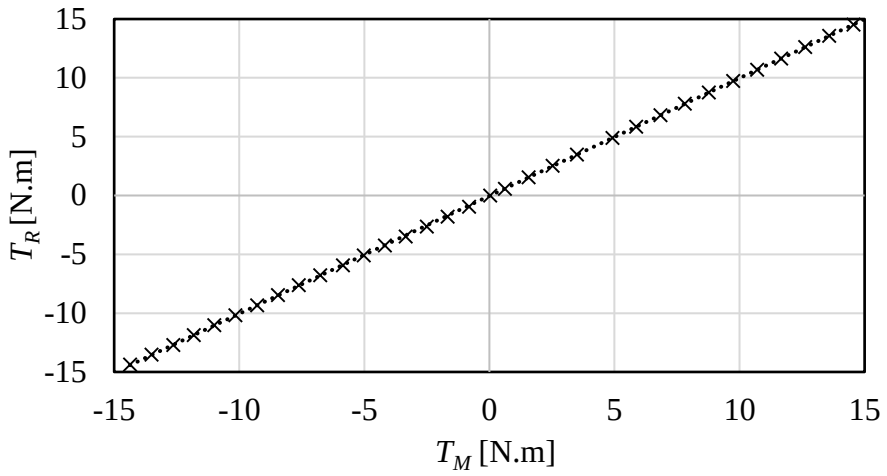

Figure A.9: Torque calibration curve

The linear calibration curve is given by:

$$T_R = 1.001T_m - 0.035 \qquad R^2 = 1 \tag{A.20}$$

A.6 Pitot tubes

To ensure that the 2 pitot tubes used in the experimental process measured accurately, a test was conducted to compare the measured speed of the 2 with one another, this comparison is given in Figure A.10.

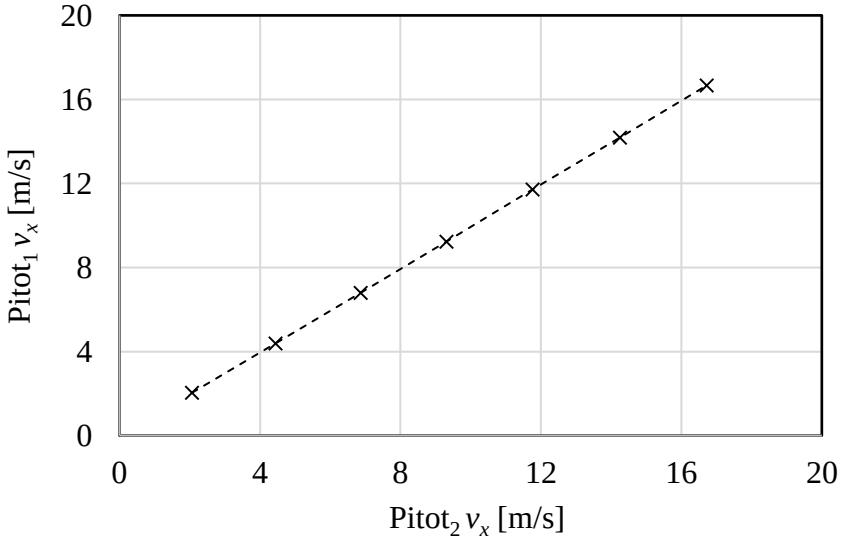

Figure A.10: Pitot velocity measurement comparison

Appendix B Sample calculations and derivations

B.1 Derivation of Equation 7

To determine the required cross-flow rate needed to affect the modified facility's fan row's performance Equation 7 was derived from Equation 2.

Equation 2 was rearranged to make the dimensionless platform height the subject:

$$\frac{H}{d_F} = \left[6.35 \cdot Ln\left[0.985 - \xi_{sys}\right] \cdot \left(\frac{n_f}{n_f+45}\right)\right] \quad \text{(B.1)}$$

The average cross-flow velocity into the inlet area can be calculated using:

$$v_x = \frac{V_{Isys} \cdot \xi_{sys}}{H \cdot W} \quad \text{(B.2)}$$

Using Equation B.1 and B.2 the average cross-flow velocity into the inlet chamber of the original multiple fan test facility could be determined and is given by Equation B.3.

$$v_x = V_{Isys} \cdot \xi_{sys} \cdot \left[6.35 \cdot Ln\left[0.985 - \xi_{sys}\right] \cdot \left(\frac{n_f}{n_f+45}\right)\right]^{-1} \cdot \frac{1}{d_f \cdot W} \quad \text{(B.3)}$$

Based on the assumption that having similar average cross-flow velocities beneath the platform (analogous to the inlet area of the multiple fan test facility), would have the same effect on the fan rows performance irrespective of the inlet dimension or the physical design, Equation B.3 thus gives the required average cross-flow velocity needed for the modified multiple fan test facility. This can be used to determine a required cross-flow rate using Equation B.4.

$$V_c = v_x \cdot H \cdot W \quad \text{(B.4)}$$

The final equation is then given by:

$$V_c = V_{Isys} \cdot \xi_{sys} \cdot \left[6.35 \cdot Ln\left[0.985 - \xi_{sys}\right] \cdot \left(\frac{n_f}{n_f+45}\right)\right]^{-1} \cdot \frac{H}{d_F} \quad \text{(B.5)}$$

B.2 Integration of the wind profile

To determine the average wind velocity, the wind profile as given by Equation B.6 had to be integrated over an area.

$$v_{wp}(y) = v_w \cdot \left(\frac{y}{H}\right)^{\frac{1}{7}} \quad \text{(B.6)}$$

The average wind velocity (v_{wa}) is thus given by the following equation:

$$v_{wa} = \frac{\int_0^H v_{wp}(y) \cdot W dy}{W \cdot H} \tag{B.7}$$

This reduces to:

$$v_{wa} = \frac{\int_0^H v_w \cdot \left(\frac{y}{H}\right)^{\frac{1}{7}} dy}{\mathrm{H}} \tag{B.8}$$

Determining the integral, the average wind velocity is given by (v_w is the wind speed at platform height):

$$v_{wa} = \frac{7}{8} \cdot v_w \tag{B.9}$$

Rearranging to make the wind speed at platform height the subject, this equation gives the integrational constant needed to determine wind speed at platform height from the average wind speed.

$$v_w = \frac{8}{7} \cdot v_{avg} \tag{B.10}$$

B.3 Calculating fan static pressure

Firstly, as the static pressure measurement is taken before the hex-core mesh (refer to Figure B.1) a formula had to be derived to manipulate this measurement as to give the static pressure rise across the fan.

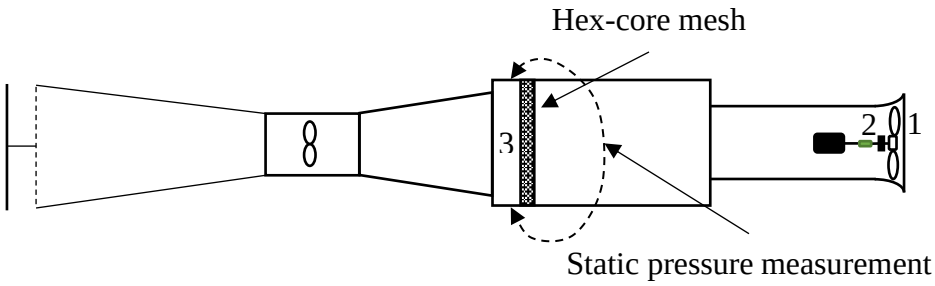

Figure B.1: Pressure measurement

The total pressure at point 3 can be written in terms of the total pressure at point 2 by taking into account the pressure loss between point 2 and 3:

$$p_{t3} = p_{t2} - \Delta p_{loss} - \Delta p_{hex} \tag{B.11}$$

Where this can be written in terms of static and dynamic pressures:

$$p_{s3} + p_{dyn3} = p_{s2} + p_{dyn2} - \Delta p_{loss} - \Delta p_{hex} \quad \text{(B.12)}$$

This can be rearranged to make the static pressure at point 2 the subject:

$$p_{s2} = p_{s3} + p_{dyn3} + \Delta p_{loss} + \Delta p_{hex} - p_{dyn2} \quad \text{(B.13)}$$

The fan static pressure rise between point 1 (where point 1 is atmospheric conditions) and 2 would then be equal to the gauge pressure measured at point 2 as the pressure at point 1 is simply the atmospheric pressure.

$$p_{fs} = p_{s2} \quad \text{(B.14)}$$

The fan static pressure can thus be calculated by:

$$p_{fs} = p_{s3} + \frac{1}{2}\rho v_3^2 + \Delta p_{loss} + \Delta p_{hex} - \frac{1}{2}\rho v_2^2 \quad \text{(B.15)}$$

Where both v_2 and v_3 can be determined from the measured volume flow rate. Where the pressure loss across the hex-core mesh can be determined using Equation B.16 as given by van der Spuy (2011):

$$\Delta p_{hex} = 0.0981 v_3^2 + 1.4782 v_3 \quad \text{(B.16)}$$

The pressure loss across the ducting can be calculated using a correlation for the loss coefficient caused by a straight duct section as given by the ISO 5801 standard (ISO, 2007):

$$K_{duct} = 0.005 + 0.42(Re)^{-0.3} \quad \text{(B.17)}$$

and to account for the sudden expansion caused by the plenum chamber (Cengel and Boles, 2011):

$$K_L = \left(1 - \frac{d^2}{D^2}\right)^2 \approx 0.1 \quad \text{(B.18)}$$

Then the total pressure loss from after the hex-core mess to point 2 can be given by:

$$\Delta p_{loss} = [0.1 + 0.005 + 0.42(Re_2)^{-0.3}] \cdot \frac{v_2^2}{2\rho} + [0.005 + 0.42(Re_3)^{-0.3}] \cdot \frac{v_3^2}{2\rho} \quad \text{(B.19)}$$

B.4 Post-processing of recorded data

The following sample calculation shows how the fan static pressure and power was calculated as well as how the data was scaled to a density of ρ = 1.2 kg/m^3 using

the fan scaling laws. The fan static pressure and power was calculated to determine the performance characteristics as to compare with Fourie (2014).

The ambient conditions for a specific test point's data is given in Table B.1.

Table B.1: Ambient condition

T_a [K]	T_{wb} [K]	P_a [Pa]
297.15	293.15	97688.69

To calculate the density of the air, considering the humidity, it was first required to calculate the humidity ratio (all fluid property correlations used are from Kröger (2004)):

$$w = \left[\frac{2501.6-2.3263(T_{wb}-273.15)}{2501.6+1.8577(T_a-273.15)-4.184(T_a-273.15)}\right]\left[\frac{0.62509p_{vwb}}{p_a-1.005p_{vwb}}\right] - \left[\frac{1.00416(T_a-T_{wb})}{2501.6+1.8577(T_a-273.15)-4.184(T_a-273.15)}\right] \quad \text{(B.20)}$$

The vapor pressure at wet bulb temperature (p_{vwb}) can be calculated by:

$$p_v = 10^z \quad \text{(B.21)}$$

$$z = 10.79586\left(1-\frac{273.16}{T}\right) + 5.02808\log_{10}\left(\frac{273.16}{T}\right) + 1.50474 \times 10^{-4}\left[1-10^{-8.29692\left\{\left(\frac{T}{273.16}\right)-1\right\}}\right] + 4.2873 \times 10^{-4}\left[10^{4.76955\left(1-\frac{273.16}{T}\right)}-1\right] + 2.786118312 \quad \text{(B.22)}$$

Substituting the wet bulb temperature into Equation B.21 gives p_{vwb} = 2336.994 Pa. Now substituting the vapor pressure at wet bulb temperature, ambient temperature (dry bulb) and atmospheric pressure into Equation B.20 gives w = 0.013645.

Calculating the density of an air vapor mixture as given by Equation B.23:

$$\rho_{av} = \frac{(1+w)\left[1-\frac{w}{w+0.62198}\right]p_a}{287.08\,T_a} \quad \text{(B.23)}$$

and this results in a density of ρ_{av} = 1.1359 kg/m^3.

Calculating the dynamic viscosity at the given ambient dry bulb temperature using the following correlation:

$$\mu = 2.287973 \times 10^{-6} + 6.259793 \times 10^{-8}T_a - 3.131956 \times 10^{-11}T_a^2 + 8.15038 \times 10^{-15}T_a^3 \quad \text{(B.24)}$$

where this equates to $\mu = 1.83373 \times 10^{-5}$ m^2/s.

The zero readings were taken before and after the test for both the torque transducer and the pressure transducer and are given in Table B.2. The zero reading for only these two transducers were subtracted from the measured values, as these transducers where calibrated form zero and both these transducers were more susceptible to ambient changes effecting their zero readings.

Table B.2: Zero-readings for torque and pressure transducers

	Zero at start	**Zero at end**	**Zero average**
T_m **[N·m]**	0.025	0.007	0.016
p_{s3} **[Pa]**	0.47	0.97	0.72

The mechanical friction caused by the bearing was measured by removing the fan an taking a torque measurement then running the motor at 1000 rpm for 10 minutes and again taking a torque measurement, the difference between these two measurements would then be the torque loss (T_{loss}) and was equal to $T_{loss} = 0.097$ N·m.

The measured values for the L630 blade are given in Table B.3 and these values have already been converted from a voltage reading using the calibration curves given in Appendix A. The zero-reading given in Table B.2, and the torque loss has already been subtracted.

Table B.3: Measured values

V **[m^3/s]**	p_{s3} **[Pa]**	T_M **[N·m]**	N **[rpm]**
1.499	55.96	1.457	1000.95

Determining the fan static pressure using Equation B.15:

$$p_{fs} = p_{s3} + \frac{1}{2}\rho v_3^2 + \Delta p_{loss} + \Delta p_{hex} - \frac{1}{2}\rho v_2^2$$

The average velocity in the fan duct can be calculated:

$$v_2 = \frac{V}{A_2} = \frac{4V}{\pi d^2} = 4.81\ \mathrm{m/s} \qquad \text{(B.25)}$$

where the diameter of the duct is $d = 0.63$ m.

The average velocity through the Plenum chamber:

$$v_3 = \frac{V}{A_3} = \frac{V}{a^2} = 2.4 \frac{\text{m}}{\text{s}} \tag{B.26}$$

Where the Plenum chamber has a square cross-section with a dimension of a = 0.79 m.

Both the pressure loss coefficients have to be calculated, firstly the pressure loss through the hex-core mesh, using Equation B.16:

$$\Delta p_{hex} = 0.0981 v_3^2 + 1.4782 v_3 = 4.116 \text{ Pa}$$

Then the pressure loss as a result of the ducting using Equation B.19:

$$\Delta p_{loss} = [0.1 + 0.005 + 0.42(Re_2)^{-0.3}] \cdot \frac{v_2^2}{2\rho} + [0.005 + 0.42(Re_3)^{-0.3}] \cdot \frac{v_3^2}{2\rho}$$

Calculating the Reynolds numbers:

$$Re_2 = \frac{\rho_{av} d_2 v_2}{\mu} = 187655.6 \tag{B.27}$$

$$Re_3 = \frac{\rho_{av} d_{H3} v_3}{\mu} = 117534.4 \tag{B.28}$$

Substituting into Equation B.19 results in a pressure loss of Δp_{loss} = 1.581 Pa. substituting the pressure losses and velocities into Equation B.15 to calculate the fan static pressure rise:

$$p_{fs} = 51.8 \text{ Pa}$$

The fan shaft power can be calculated as follows:

$$P_f = \frac{2\pi}{60} N_f T_M = 152.74 \text{ W} \tag{B.29}$$

All the measured values can be scaled to the reference density of ρ = 1.2 kg/m^{3}and to the exact rotational speed of N = 1000 rpm using the following equations.

$$p'_{fs} = \left(\frac{N'}{N}\right)^2 \left(\frac{\rho'}{\rho}\right) = 54.57 \text{ Pa} \tag{B.30}$$

$$V' = V \frac{N'}{N} = 1.498 \text{ m}^3/s \tag{B.31}$$

$$P'_f = P_f \left(\frac{N'}{N}\right)^3 \left(\frac{\rho'}{\rho}\right) = 160.9 \text{ W} \tag{B.32}$$

Appendix C CFD

This section will give a brief overview of the CFD models used to help with the designing process of the inlet duct. All CFD simulation were performed using *ANSYS Fluent* version 18.1.

C.1 2D ACC fan row

The two-dimensional ACC fan row simulation was used to investigate the effect of having a fixed ducted-inlet on both fan performance and the *x*-velocity profile of the approaching flow. The geometry was based on the dimensions of the original multiple fan test facility but each of the three fan units were simplified as square units with a bellmouth inlets. The bellmouth dimensions used are the actual dimensions of the bellmouths on the multiple fan test facility as given by Visser (1990), the geometry is given in Figure C.1,

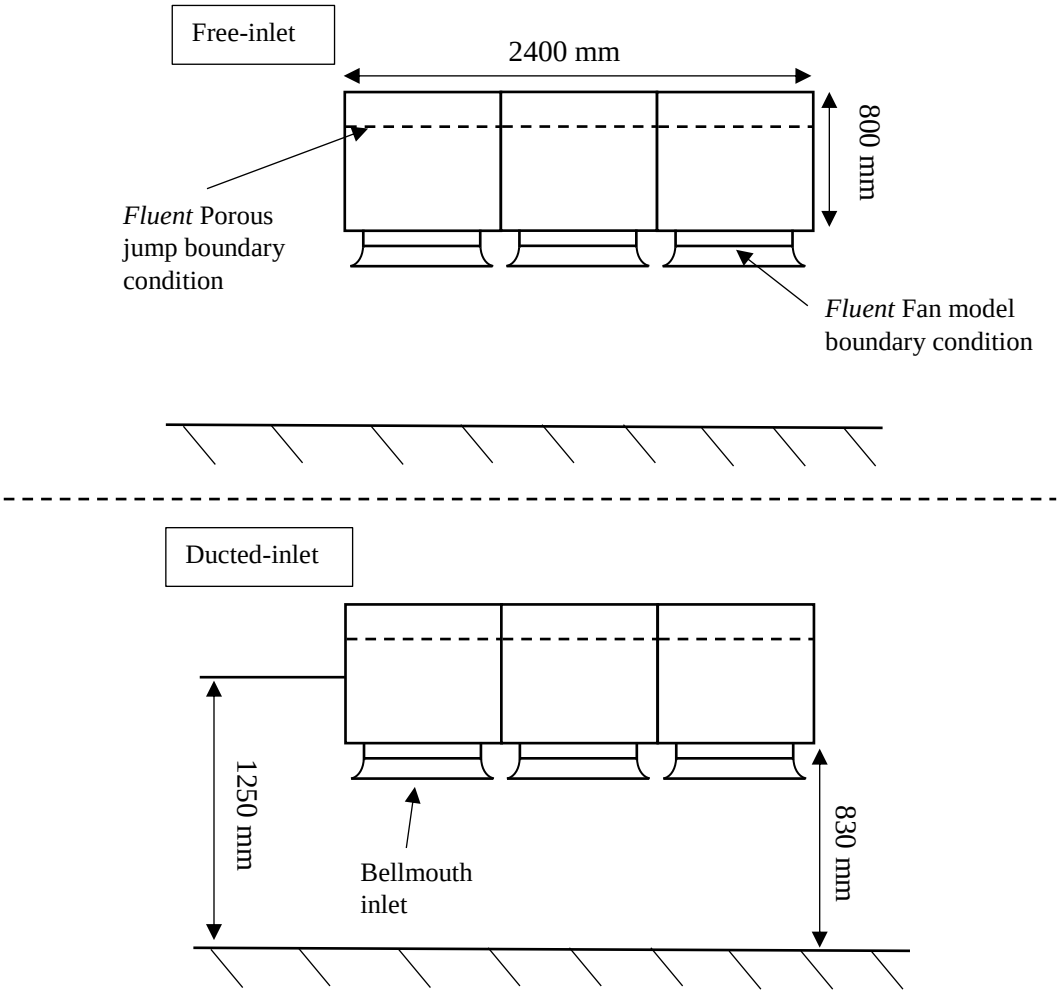

Figure C.1: Model Geometry of fan unit

Each of the fans were modeled using *fluent's* fan boundary condition, which requires the fan's static-to-static pressure rise as a function of the velocity normal to the fan (Fluent, 2017). The static-to-static pressure jump polynomial for the L630 fan that was used is given by Equation C.1, this polynomial was obtained from Fourie (2014).

$$p_{sf} = -0.762v^3 + 7.072v^2 - 31.649v + 151.6 \quad \text{(C.1)}$$

Due to the fan unit being approximated as a square unit the system resistance consisting of the hex-core mesh and porous outlet had to be combined into a single system resistance. This system resistance was implemented using a one-dimensional porous jump boundary conditions which is a one-dimensional simplification of the porous media model (Fluent, 2017), the pressure drop across the boundary is given by Equation C.2.

$$\Delta p = -\left(\frac{\mu}{\alpha}v + C_2\frac{1}{2}\rho v^2\right)\Delta m \quad \text{(C.2)}$$

where α is the permeability of the medium, C_2 the pressure jump coefficient, v the velocity normal to the face and Δm the thickness of the medium.

The system resistance which includes both the hex-core mesh and the porous outlet was given by Equation C.3 and each of the coefficients are listed in Table C.1.

$$p_{sys} = \Delta m_{hex}\left(\frac{\mu}{\alpha}v + C_2\frac{1}{2}\rho v^2\right) + \frac{k_o\rho}{2}v^2 \quad \text{(C.3)}$$

where k_o is outlet loss coefficient.

Table C.1: The coefficients for Equation

α	C_2	Δm_{hex}	k_o
5.524×10^{-7}	2.442	0.1	3.55

The coefficient for the hex-core mesh was based on experimental measurements done by van der Spuy (2011) while the outlet loss coefficient was approximated based on a correlation given by Fourie (2014).

Equation C.3 was used to determine the coefficients required for the porous jump boundary condition as given by Equation C.2, these coefficients are listed in Table C.2.

Table C.2: The coefficients for Equation

α	C_2	Δm_{hex}
8.5239×10^{-7}	37.942	0.1

The fan curve and system resistance are shown in Figure C.2.

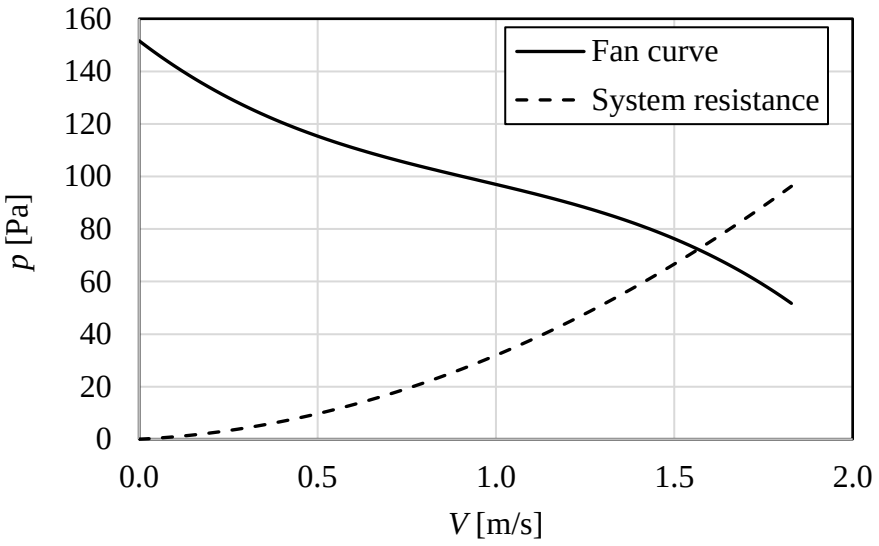

Figure C.2: Fan curve and system resistance

The far-field geometry boundary conditions are given in Figure C.3 for both the free-inlet and duct-inlet.

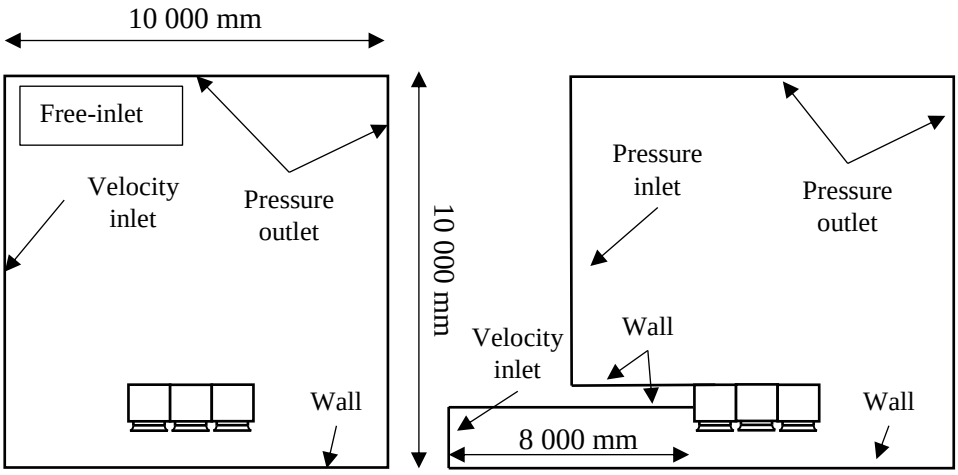

Figure C.3: Far-field geometry and boundary conditions

Figure C.4 shows the meshing used for the free-inlet case, triangular meshing method was used with inflation along the walls of the fan units. The inflation consisted of 8 layers with a growth rate of 1.6 where the first layer thickness was t = 0.4 mm. The total number of cells for the mesh was 96 532 cells.

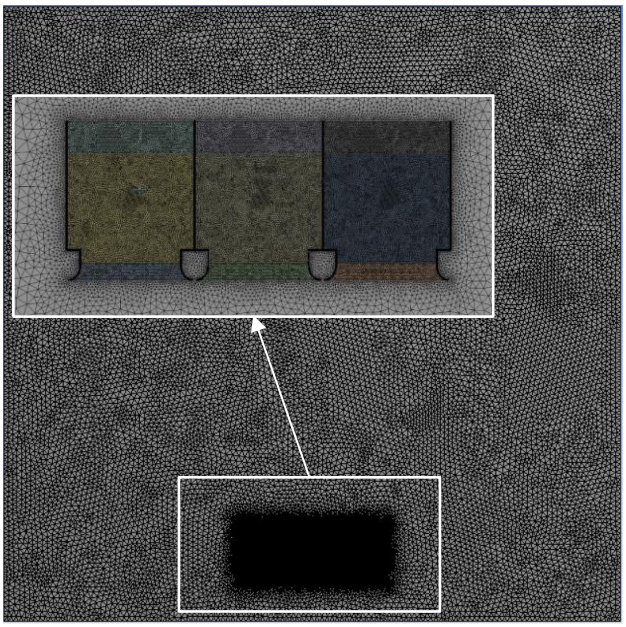

Figure C.4: Free-inlet mesh with a closeup of fan units

Figure C.5 shows the meshing used for the duct-inlet case.

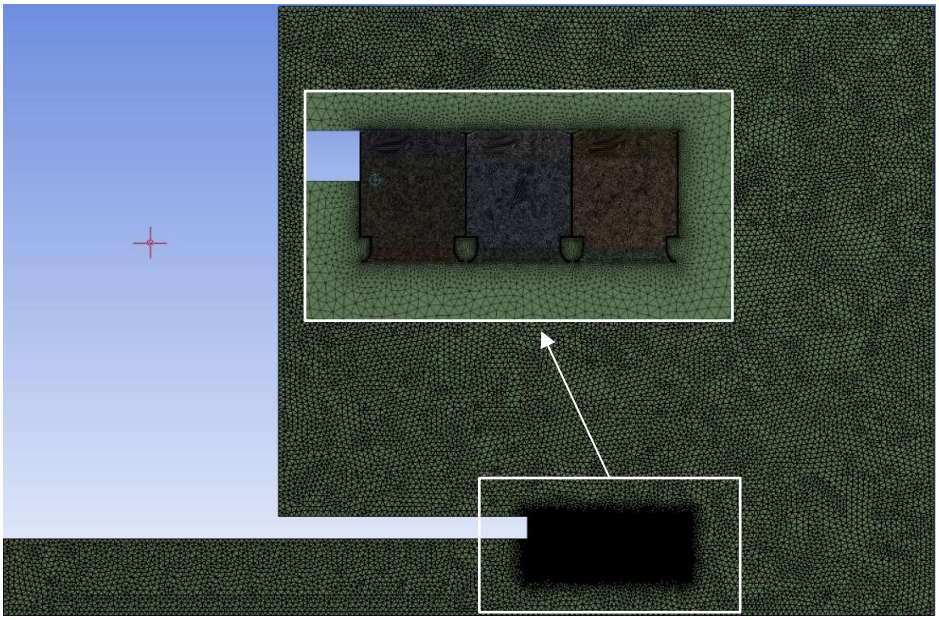

Figure C.5: Duct-inlet mesh with a closeup of fan units

The meshing method used for the duct-inlet case was similar to that of the free-inlet, where a triangular meshing method was used with inflation on the walls of the fan units. The inflation specifications were the same as for the free-inlet case. The total number of cells for the mesh was 96 093cells. Mesh independence study was conducted on the free-inlet case subject to a 3 m/s wind with the parameter of interest being the average cross-flow velocity, this was selected as the magnitude of the cross-flow velocity influenced the performance of all 3 fans, the result for this study are given in Figure C.6

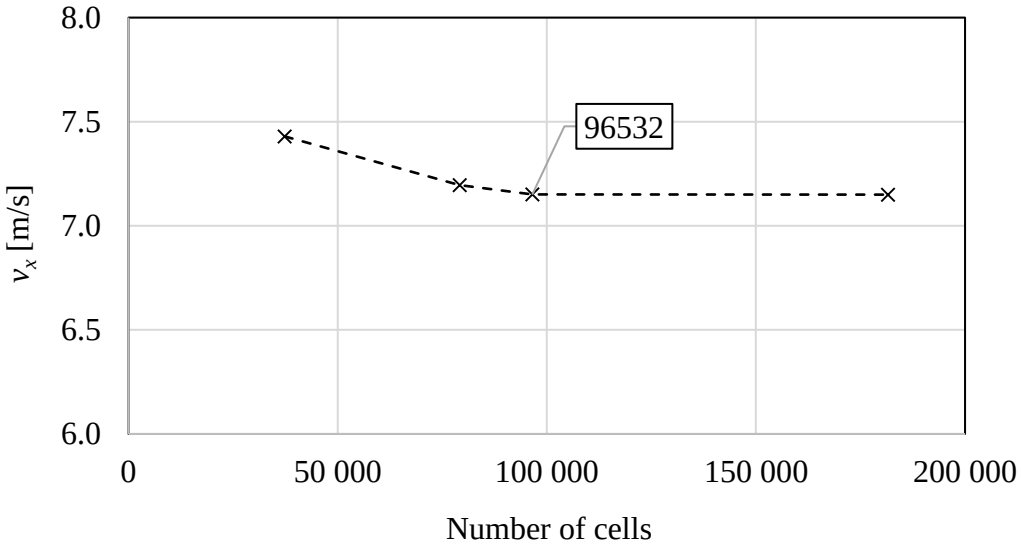

Figure C.6: Free-inlet's mesh independence study

The turbulence model that was selected was *k-ε* with standard wall functions, as to help speed up convergence. The CFD was only used to help with the design process and therefore simplicity within the model was important.

C.2 3D inlet duct

CFD model was used to help with the design process of both the diffusing and straightening duct sections. Here a brief overview of the mesh and the turbulence model used will be given.

Triangular meshing method used with an inflation layer along the walls, the inflation consisted of 5 layers with a growth rate of 1.6 where the first layer thickness was t = 1 mm, the mesh consisted of a number of 1 313 917 cells.

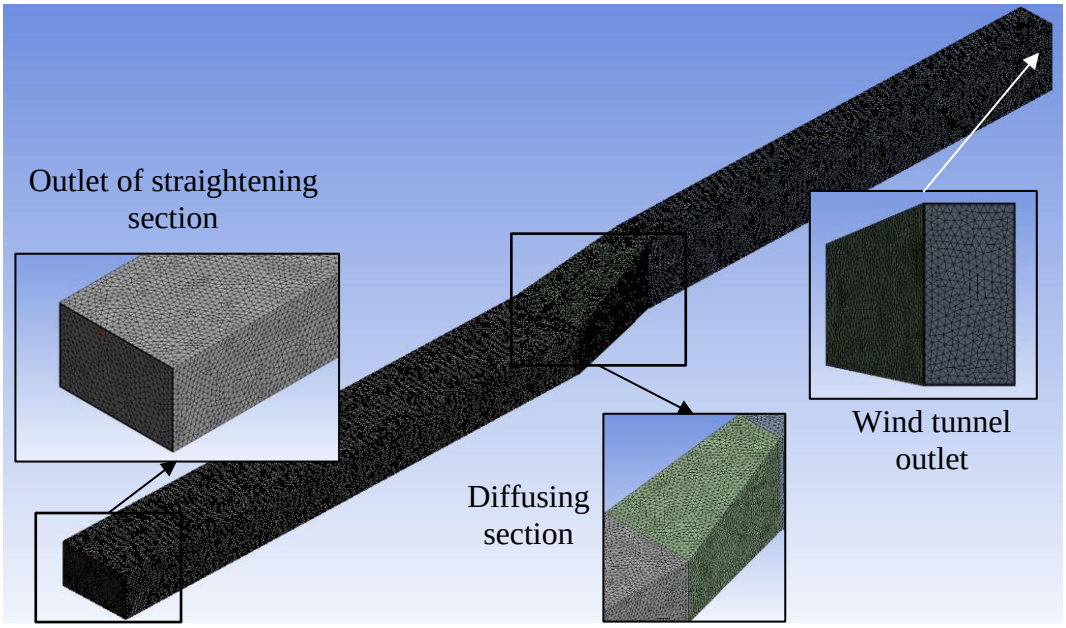

Figure C.7: The mesh used for modeling the duct

The mesh independence study done was based on the outlet velocity profile for the diffusing section. Three different meshes were used, each one from a fine to a coarse mesh was used to determine the outlet velocity profile of the diffusing section. The results for each of these meshes are given in Figure C.8, an inlet velocity of 6 m/s was used for the mesh independence study.

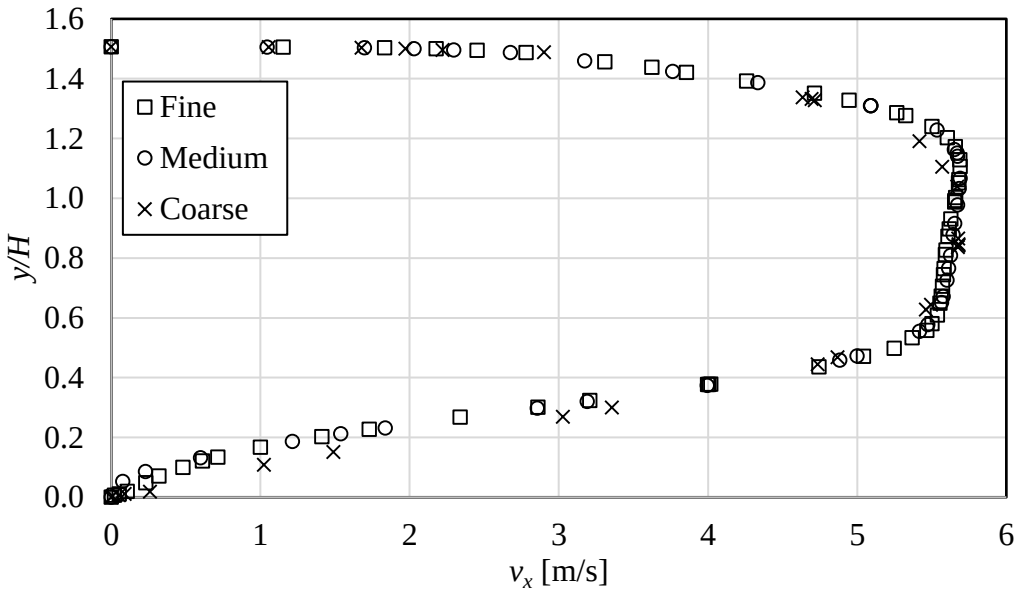

Figure C.8: Inlet duct's mesh independence study

Table C.3 gives the number of cells in each of the meshes, the fine mesh was used as the final mesh.

Table C.3: The number of cells

Fine	Medium	Coarse
1 313 917	449 716	73 696

The turbulence model that was used was k-ω SST turbulence model. This model was selected specifically to improve the modeling of separation.

Appendix D Experimental results

This appendix gives the average data from the repeated tests for the no-screen case, M50, M60 and M75 tests as well as the standard deviation between these repeated tests. The given data can thus be used for the purpose of future validation.

D.1 No-screen data

The average relevant data from 4 conducted test with no windscreen installed is given in Table D.1.

Table D.1: Average values for NS

β	ξ_{f1}	ξ_{f2}	ξ_{f3}	ξ_{sys}	P_w	$\varepsilon/\varepsilon^*$
0.094	0.946	0.923	0.944	0.937	166.6	1.000
0.130	0.961	0.946	0.970	0.959	166.8	1.954
0.163	0.957	0.961	0.959	0.959	167.3	3.020
0.197	0.936	0.966	0.953	0.952	169.6	3.750
0.231	0.880	0.963	0.959	0.934	174.2	3.358
0.265	0.778	0.970	0.963	0.905	177.0	2.839
0.298	0.644	0.990	0.961	0.866	174.1	3.625
0.331	0.532	0.984	0.968	0.830	176.2	4.425
0.364	0.394	0.983	0.981	0.788	181.3	4.254

The standard deviation (σ) between these 4 tests is listed in Table D.2.

Table D.2: The standard deviation for NS

β	$\sigma(\xi_{f1})$	$\sigma(\xi_{f2})$	$\sigma(\xi_{f3})$	$\sigma(\xi_{sys})$	$\sigma(P_w)$	$\sigma(\varepsilon/\varepsilon^*)$
0.094	0.004	0.011	0.008	0.006	1.158	0.151
0.130	0.002	0.013	0.012	0.008	1.822	0.159
0.163	0.001	0.005	0.010	0.005	1.332	0.204
0.197	0.001	0.000	0.002	0.001	1.161	0.277
0.231	0.001	0.001	0.005	0.001	0.889	0.142
0.265	0.000	0.001	0.001	0.000	0.990	0.058
0.298	0.002	0.001	0.001	0.001	1.132	0.248
0.331	0.004	0.001	0.002	0.000	0.968	0.494
0.364	0.004	0.001	0.001	0.001	0.694	0.488

D.2 Windscreen data for M50

The average values of the relevant data from 3 conducted test with the M50 windscreen installed at 25% covering are given in Table D.3.

Table D.3: The average values for M50 25%

β	ξ_{f1}	ξ_{f2}	ξ_{f3}	ξ_{sys}	P_w	$\varepsilon/\varepsilon^*$
0.094	0.944	0.928	0.932	0.934	171.0	1.141
0.130	0.946	0.974	0.947	0.956	170.8	1.678
0.163	0.911	0.963	0.913	0.929	170.4	1.929
0.197	0.840	0.973	0.931	0.915	172.0	2.032
0.230	0.724	0.960	0.948	0.878	180.1	2.521
0.264	0.554	0.930	0.956	0.815	176.6	2.763
0.297	0.456	0.845	0.956	0.754	178.5	2.528
0.330	0.373	0.758	0.978	0.705	179.5	2.468
0.362	0.287	0.680	0.983	0.652	179.7	2.467

The standard deviation (σ) between these 3 tests is listed in Table D.4.

Table D.4: The standard deviation for M50 25%

β	$\sigma(\xi_{f1})$	$\sigma(\xi_{f2})$	$\sigma(\xi_{f3})$	$\sigma(\xi_{sys})$	$\sigma(P_w)$	$\sigma(\varepsilon/\varepsilon^*)$
0.094	0.004	0.016	0.009	0.004	0.159	0.052
0.130	0.001	0.024	0.007	0.010	0.380	0.101
0.163	0.001	0.002	0.004	0.001	0.325	0.118
0.197	0.001	0.002	0.001	0.001	0.035	0.108
0.230	0.001	0.004	0.002	0.002	0.409	0.163
0.264	0.002	0.003	0.002	0.002	0.337	0.016
0.297	0.002	0.002	0.002	0.001	0.741	0.013
0.330	0.001	0.003	0.003	0.002	0.069	0.024
0.362	0.005	0.000	0.003	0.001	0.069	0.062

The average values of the relevant data from 3 conducted test with the M50 windscreen installed at 50% covering are given in Table D.5.

Table D.5: The average values for M50 50%

β	ξ_{f1}	ξ_{f2}	ξ_{f3}	ξ_{sys}	P_w	$\varepsilon/\varepsilon^*$
0.094	0.926	0.913	0.935	0.925	167.6	0.956
0.129	0.919	0.941	0.934	0.931	169.9	1.251
0.162	0.880	0.971	0.895	0.916	171.5	2.299
0.196	0.825	0.929	0.937	0.898	177.1	2.530
0.229	0.715	0.849	0.973	0.846	184.2	2.943
0.262	0.581	0.788	0.860	0.744	178.7	3.537
0.295	0.546	0.802	0.762	0.704	179.4	3.455
0.327	0.516	0.803	0.758	0.693	181.0	3.952
0.360	0.460	0.801	0.788	0.684	182.1	4.419

The standard deviation (σ) between these 3 tests is listed in Table D.6.

Table D.6: The standard deviation for M50 50%

β	$\sigma(\xi_{f1})$	$\sigma(\xi_{f2})$	$\sigma(\xi_{f3})$	$\sigma(\xi_{sys})$	$\sigma(P_w)$	$\sigma(\varepsilon/\varepsilon^*)$
0.094	0.002	0.009	0.006	0.003	0.646	0.031
0.129	0.001	0.010	0.015	0.008	1.081	0.049
0.162	0.001	0.002	0.007	0.003	0.895	0.152
0.196	0.000	0.001	0.004	0.001	0.995	0.220
0.229	0.001	0.001	0.002	0.000	1.180	0.192
0.262	0.001	0.002	0.000	0.001	0.903	0.077
0.295	0.001	0.001	0.001	0.001	0.714	0.064
0.327	0.001	0.001	0.005	0.001	0.945	0.246
0.360	0.002	0.001	0.002	0.001	0.000	0.070

The average values of the relevant data from 3 conducted test with the M50 windscreen installed at 75% covering are given in Table D.7.

Table D.7: The average values for M50 75%

β	ξ_{f1}	ξ_{f2}	ξ_{f3}	ξ_{sys}	P_w	$\varepsilon/\varepsilon^*$
0.093	0.935	0.941	0.941	0.939	169.5	0.853
0.129	0.924	0.974	0.975	0.958	171.9	1.482
0.162	0.881	0.943	1.003	0.943	174.1	2.209
0.195	0.807	0.869	0.992	0.889	177.9	2.015
0.227	0.706	0.881	0.870	0.820	178.9	3.241
0.259	0.653	0.915	0.873	0.815	174.3	3.533
0.292	0.627	0.922	0.882	0.812	174.3	3.517
0.324	0.602	0.917	0.911	0.811	176.7	3.993
0.356	0.559	0.903	0.933	0.800	179.5	4.926

The standard deviation (σ) between these 3 tests is listed in Table D.8.

Table D.8: The standard deviation for M50 75%

β	$\sigma(\xi_{f1})$	$\sigma(\xi_{f2})$	$\sigma(\xi_{f3})$	$\sigma(\xi_{sys})$	$\sigma(P_w)$	$\sigma(\varepsilon/\varepsilon^*)$
0.093	0.007	0.017	0.008	0.006	1.018	0.038
0.129	0.002	0.007	0.006	0.005	1.241	0.138
0.162	0.000	0.002	0.021	0.007	0.798	0.154
0.195	0.003	0.002	0.004	0.002	0.141	0.098
0.227	0.001	0.002	0.003	0.001	1.292	0.280
0.259	0.003	0.001	0.003	0.002	0.862	0.265
0.292	0.002	0.001	0.004	0.002	0.938	0.196
0.324	0.001	0.000	0.003	0.001	1.035	0.129
0.356	0.001	0.001	0.002	0.000	0.000	0.855

D.3 Windscreen data for M60

The average values of the relevant data from 3 conducted test with the M60 windscreen installed at 25% covering are given in Table D.9.

Table D.9: The average values for M60 25%

β	ξ_{f1}	ξ_{f2}	ξ_{f3}	ξ_{sys}	P_w	$\varepsilon/\varepsilon^*$
0.093	0.944	0.924	0.937	0.935	164.6	1.417
0.130	0.937	0.955	0.952	0.948	164.4	1.826
0.163	0.887	0.961	0.926	0.925	162.8	1.779
0.196	0.779	0.983	0.940	0.901	164.7	2.393
0.230	0.563	1.010	0.958	0.845	167.7	2.898
0.263	0.494	0.922	0.983	0.801	173.0	2.049
0.296	0.390	0.747	0.991	0.711	172.7	1.817
0.329	0.310	0.613	0.980	0.636	171.9	1.802
0.361	0.229	0.515	0.947	0.565	172.8	1.912

The standard deviation (σ) between these 3 tests is listed in Table D.10.

Table D.10: The standard deviation (σ) for M60 25%

β	$\sigma(\xi_{f1})$	$\sigma(\xi_{f2})$	$\sigma(\xi_{f3})$	$\sigma(\xi_{sys})$	$\sigma(P_w)$	$\sigma(\varepsilon/\varepsilon^*)$
0.093	0.002	0.009	0.001	0.003	1.609	0.046
0.130	0.001	0.020	0.008	0.009	1.418	0.076
0.163	0.001	0.003	0.001	0.001	1.647	0.041
0.196	0.001	0.001	0.004	0.001	1.793	0.038
0.230	0.002	0.000	0.002	0.001	0.702	0.070
0.263	0.000	0.002	0.000	0.001	0.636	0.028
0.296	0.001	0.003	0.001	0.000	0.727	0.020
0.329	0.001	0.001	0.001	0.001	0.789	0.019
0.361	0.002	0.001	0.002	0.001	0.789	0.047

The average values of the relevant data from 3 conducted test with the M60 windscreen installed at 50% covering are given in Table D.11.

Table D.11: The average values for M60 50%

β	ξ_{f1}	ξ_{f2}	ξ_{f3}	ξ_{sys}	P_w	$\varepsilon/\varepsilon^*$
0.094	0.903	0.922	0.941	0.922	161.4	0.971
0.129	0.864	0.969	0.941	0.925	163.5	1.211
0.161	0.801	0.986	0.919	0.903	167.0	1.601
0.195	0.733	0.880	0.954	0.856	174.2	1.761
0.228	0.575	0.692	0.988	0.753	171.1	2.811
0.260	0.501	0.620	0.844	0.656	170.1	2.585
0.291	0.453	0.616	0.756	0.609	173.3	2.889
0.323	0.423	0.622	0.718	0.589	176.8	3.217
0.354	0.387	0.628	0.696	0.571	179.0	3.182

The standard deviation (σ) between these 3 tests is listed in Table D.12.

Table D.12: The standard deviation for M60 50%

β	$\sigma(\xi_{f1})$	$\sigma(\xi_{f2})$	$\sigma(\xi_{f3})$	$\sigma(\xi_{sys})$	$\sigma(P_w)$	$\sigma(\varepsilon/\varepsilon^*)$
0.094	0.004	0.013	0.009	0.003	0.883	0.005
0.129	0.002	0.007	0.012	0.003	0.685	0.034
0.161	0.001	0.001	0.006	0.002	0.576	0.020
0.195	0.003	0.003	0.003	0.001	0.452	0.029
0.228	0.003	0.004	0.002	0.002	1.122	0.058
0.260	0.001	0.001	0.003	0.001	0.660	0.053
0.291	0.002	0.000	0.000	0.001	0.540	0.093
0.323	0.002	0.003	0.001	0.001	0.846	0.105
0.354	0.003	0.001	0.002	0.002	0.568	0.095

The average values of the relevant data from 3 conducted test with the M60 windscreen installed at 75% covering are given in Table D.13.

Table D.13: The average values for M60 75%

β	ξ_{f1}	ξ_{f2}	ξ_{f3}	ξ_{sys}	P_w	$\varepsilon/\varepsilon^*$
0.092	0.898	0.930	0.936	0.922	166.2	0.872
0.127	0.866	0.930	0.955	0.917	168.7	1.243
0.159	0.793	0.863	0.971	0.876	171.9	1.744
0.191	0.695	0.747	0.907	0.784	173.9	2.090
0.221	0.644	0.851	0.837	0.778	163.9	2.837
0.252	0.628	0.869	0.812	0.771	163.9	3.732
0.283	0.623	0.865	0.824	0.771	169.5	3.790
0.314	0.605	0.865	0.858	0.777	174.9	3.875
0.345	0.580	0.869	0.884	0.779	179.2	4.108

The standard deviation (σ) between these 3 tests is listed in Table D.14.

Table D.14: The standard deviation for M60 75%

β	$\sigma(\xi_{f1})$	$\sigma(\xi_{f2})$	$\sigma(\xi_{f3})$	$\sigma(\xi_{sys})$	$\sigma(P_w)$	$\sigma(\varepsilon/\varepsilon^*)$
0.092	0.004	0.006	0.002	0.003	1.473	0.004
0.127	0.002	0.001	0.006	0.003	1.427	0.023
0.159	0.002	0.002	0.010	0.003	1.266	0.046
0.191	0.001	0.003	0.002	0.002	1.375	0.051
0.221	0.005	0.004	0.005	0.002	2.039	0.045
0.252	0.002	0.002	0.002	0.001	1.278	0.108
0.283	0.001	0.001	0.001	0.001	1.240	0.120
0.314	0.000	0.002	0.000	0.001	1.091	0.127
0.345	0.000	0.001	0.001	0.000	0.861	0.118

D.4 Windscreen data for M75

The average values of the relevant data from 3 conducted test with the M75 windscreen installed at 25% covering are given in Table D.15.

Table D.15: The average values for M75 25%

β	ξ_{f1}	ξ_{f2}	ξ_{f3}	ξ_{sys}	P_w	$\varepsilon/\varepsilon^*$
0.094	0.942	0.931	0.951	0.941	165.6	1.980
0.129	0.947	0.941	0.963	0.950	165.4	2.722
0.162	0.876	0.968	0.934	0.926	159.8	2.107
0.196	0.627	1.001	0.942	0.858	161.2	3.247
0.229	0.445	1.023	0.974	0.816	165.9	2.355
0.262	0.320	0.826	1.000	0.718	169.8	1.677
0.295	0.209	0.599	0.981	0.598	169.7	1.495
0.327	0.119	0.464	0.935	0.508	170.8	1.505
0.359	0.048	0.365	0.894	0.438	176.2	1.481

The standard deviation (σ) between these 3 tests is listed in Table D.16.

Table D.16: The standard deviation for M75 25%

β	$\sigma(\xi_{f1})$	$\sigma(\xi_{f2})$	$\sigma(\xi_{f3})$	$\sigma(\xi_{sys})$	$\sigma(P_w)$	$\sigma(\varepsilon/\varepsilon^*)$
0.094	0.005	0.009	0.014	0.003	0.309	0.062
0.129	0.001	0.018	0.011	0.003	0.647	0.044
0.162	0.001	0.003	0.009	0.004	1.276	0.006
0.196	0.006	0.001	0.003	0.002	1.446	0.052
0.229	0.001	0.001	0.002	0.001	1.228	0.043
0.262	0.003	0.005	0.002	0.003	1.091	0.031
0.295	0.002	0.002	0.001	0.001	0.825	0.047
0.327	0.001	0.001	0.001	0.000	0.945	0.011
0.359	0.000	0.002	0.002	0.001	0.676	0.020

The average values of the relevant data from 3 conducted test with the M75 windscreen installed at 50% covering are given in Table D.17.

Table D.17: The average values for M75 50%

β	ξ_{f1}	ξ_{f2}	ξ_{f3}	ξ_{sys}	P_w	$\varepsilon/\varepsilon^*$
0.093	0.862	0.944	0.946	0.918	161.2	1.556
0.127	0.742	1.009	0.979	0.911	161.2	1.841
0.159	0.669	0.993	0.981	0.882	173.3	1.505
0.192	0.583	0.743	1.039	0.789	180.3	1.608
0.223	0.408	0.424	0.861	0.565	167.7	1.126
0.253	0.323	0.348	0.716	0.463	165.7	1.162
0.284	0.285	0.322	0.657	0.422	167.2	1.250
0.314	0.247	0.300	0.622	0.390	169.3	1.269
0.344	0.209	0.274	0.588	0.358	173.0	1.320

The standard deviation (σ) between these 3 tests is listed in Table D.18.

Table D.18: The standard deviation for M75 50%

β	$\sigma(\xi_{f1})$	$\sigma(\xi_{f2})$	$\sigma(\xi_{f3})$	$\sigma(\xi_{sys})$	$\sigma(P_w)$	$\sigma(\varepsilon/\varepsilon^*)$
0.093	0.003	0.006	0.006	0.002	3.215	0.040
0.127	0.003	0.002	0.008	0.004	5.163	0.051
0.159	0.003	0.007	0.003	0.003	2.407	0.045
0.192	0.002	0.003	0.002	0.002	6.843	0.084
0.223	0.001	0.001	0.001	0.001	5.034	0.044
0.253	0.001	0.003	0.001	0.001	2.669	0.032
0.284	0.001	0.002	0.001	0.001	1.016	0.005
0.314	0.003	0.004	0.001	0.003	3.943	0.008
0.344	0.001	0.003	0.001	0.002	7.559	0.000

The average values of the relevant data from 3 conducted test with the M75 windscreen installed at 75% covering are given in Table D.19.

Table D.19: The average values for M75 75%

β	ξ_{f1}	ξ_{f2}	ξ_{f3}	ξ_{sys}	P_w	$\varepsilon/\varepsilon^*$
0.093	0.795	0.926	0.891	0.871	171.3	1.701
0.127	0.701	0.790	0.970	0.821	177.1	2.123
0.157	0.594	0.567	0.843	0.668	174.0	1.531
0.184	0.589	0.597	0.751	0.646	172.3	1.579
0.212	0.577	0.634	0.705	0.639	171.1	1.984
0.240	0.557	0.652	0.671	0.627	171.0	2.394
0.267	0.531	0.661	0.641	0.612	171.7	2.809

The standard deviation (σ) between these 3 tests is listed in Table D.20.

Table D.20: The standard deviation for M75 75%

β	$\sigma(\xi_{f1})$	$\sigma(\xi_{f2})$	$\sigma(\xi_{f3})$	$\sigma(\xi_{sys})$	$\sigma(P_w)$	$\sigma(\varepsilon/\varepsilon^*)$
0.093	0.008	0.013	0.005	0.003	2.244	0.483
0.127	0.000	0.002	0.015	0.005	0.831	0.507
0.157	0.002	0.005	0.005	0.003	0.749	0.354
0.184	0.001	0.002	0.001	0.001	0.798	0.377
0.212	0.003	0.002	0.004	0.001	0.636	0.561
0.240	0.003	0.005	0.002	0.001	0.560	0.664
0.267	0.002	0.005	0.009	0.004	0.717	0.847

D.5 Wind tunnel test section profile

Figure D.7. shows the pitot tube traverse of the wind tunnels test section for both the *x*- and *y*-directions at the no-wind volume flow rate.

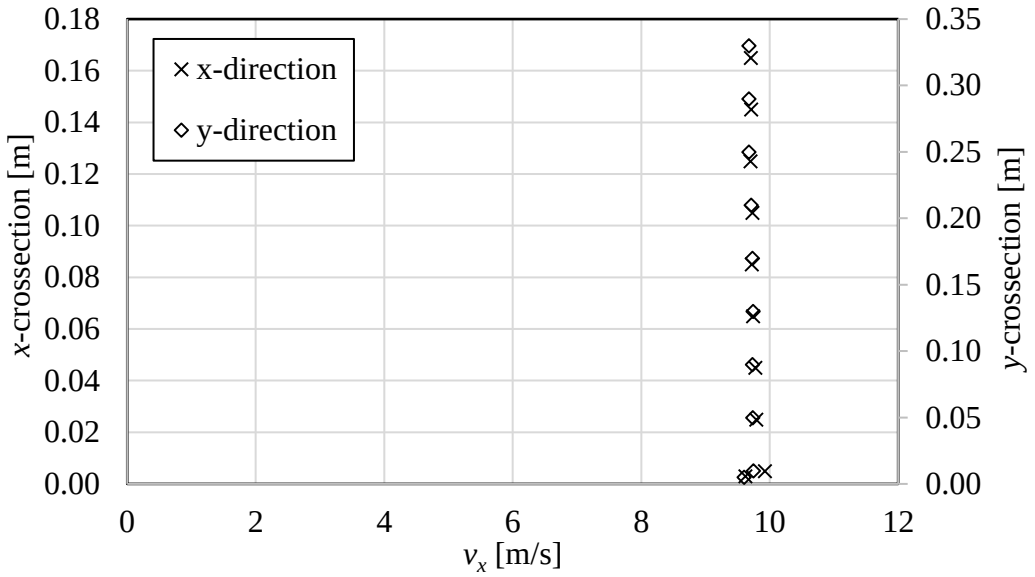

Figure D.1: Pitot tube traverse of the wind tunnel test section

Using trapezoidal numerical integration, to determine the average velocity results in v_x = 9.62 m/s whereas taking the velocity at the center of the wind tunnel's test section to be the average velocity would be v_x = 9.71 m/s. The difference between the two methods is only 0.97% and therefore the average velocity was simply taken as the velocity measured at the center of the wind tunnels test section for all the conducted tests.

D.6 M60 windscreen additional data

Figures D.8 to D.10 shows the additionally recorded data that was used to determine the no-wind β value for the test facility with the M60 windscreen installed at 25%, 50%, and 75%. Each figure also shows the curve for the polynomial fit used to determine the new no-wind β values as given in Table 7, Section 5.3.4.

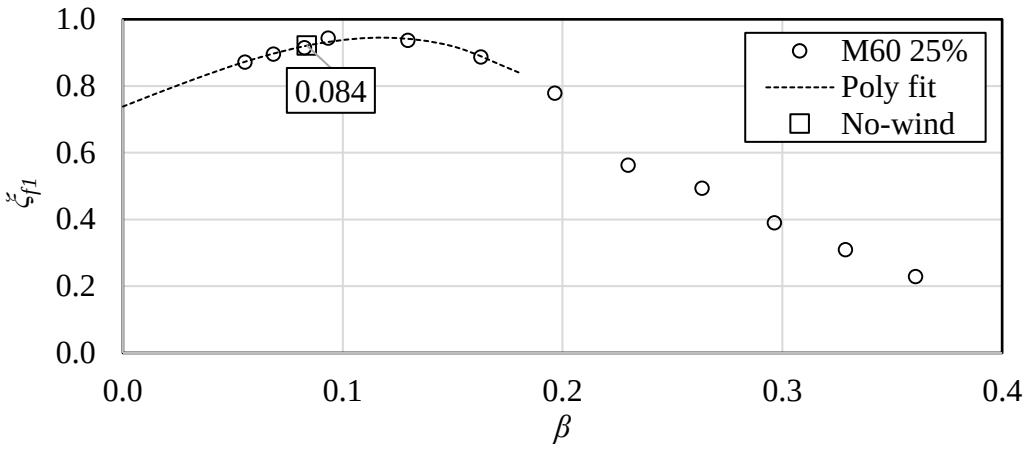

Figure D.2: Additional data for M60 at 25% covering

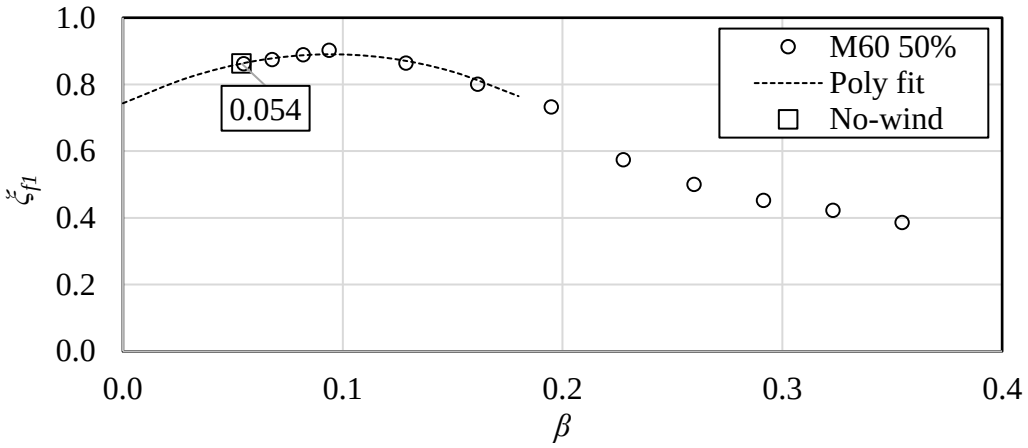

Figure D.3: Additional data for M60 at 50% covering

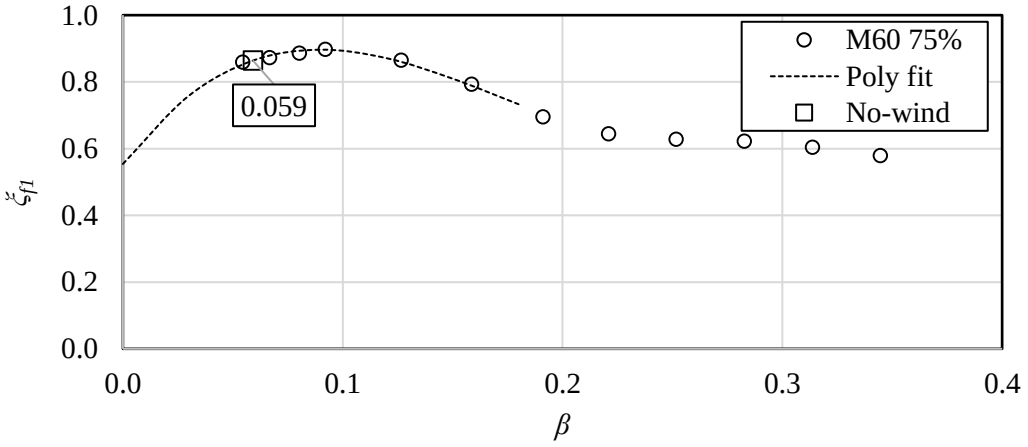

Figure D.4: Additional data for M60 at 75% covering

Appendix E PIV

The PIV system used is manufactured by Dantec Dynamics, the system consists of the following parts:

- Two Flowsense 4M CCD cameras (2048 x 2048 pixel) with 60 mm Nikon lenses.
- Synchroniser unit (80N77), the synchroniser correlates the timing between the cameras and the laser.
- 3µm Seeding generator (10F03)
- Dantec 3-axis traverse system
- Personal computer with Dantec Dynamics software with 3 National Instrument cards. The National Instrument cards are used to control the synchroniser (NI PCI-6602 card) and the two cameras (two NI PCIe-1427 cards).
- Dual-power 200- 15 double-cavity Q-switched Nd: YAG laser

The PIV data capturing and processing was validated by comparing captured data of the *x*-velocity component in the straightening duct section with that of pitot tube measurements. The validation was done for no-wind, $\beta = 0.16$, $\beta = 0.2$, $\beta = 0.26$ and $\beta = 0.33$ and are given in Figure E.1 and Figure E.2.

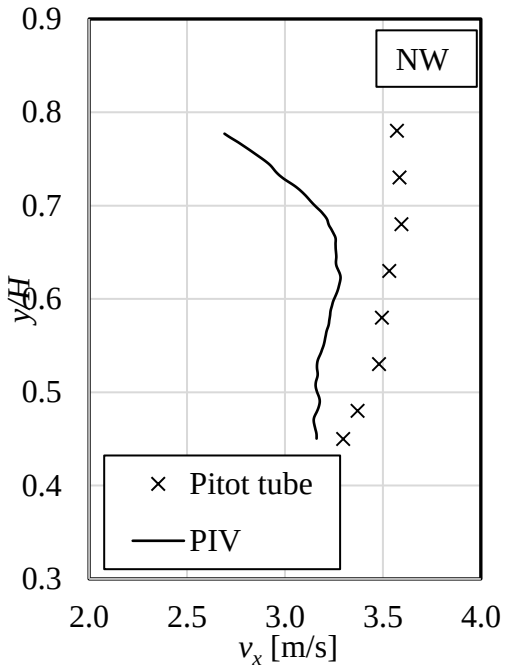

Figure E.1: PIV validation for no-wind case

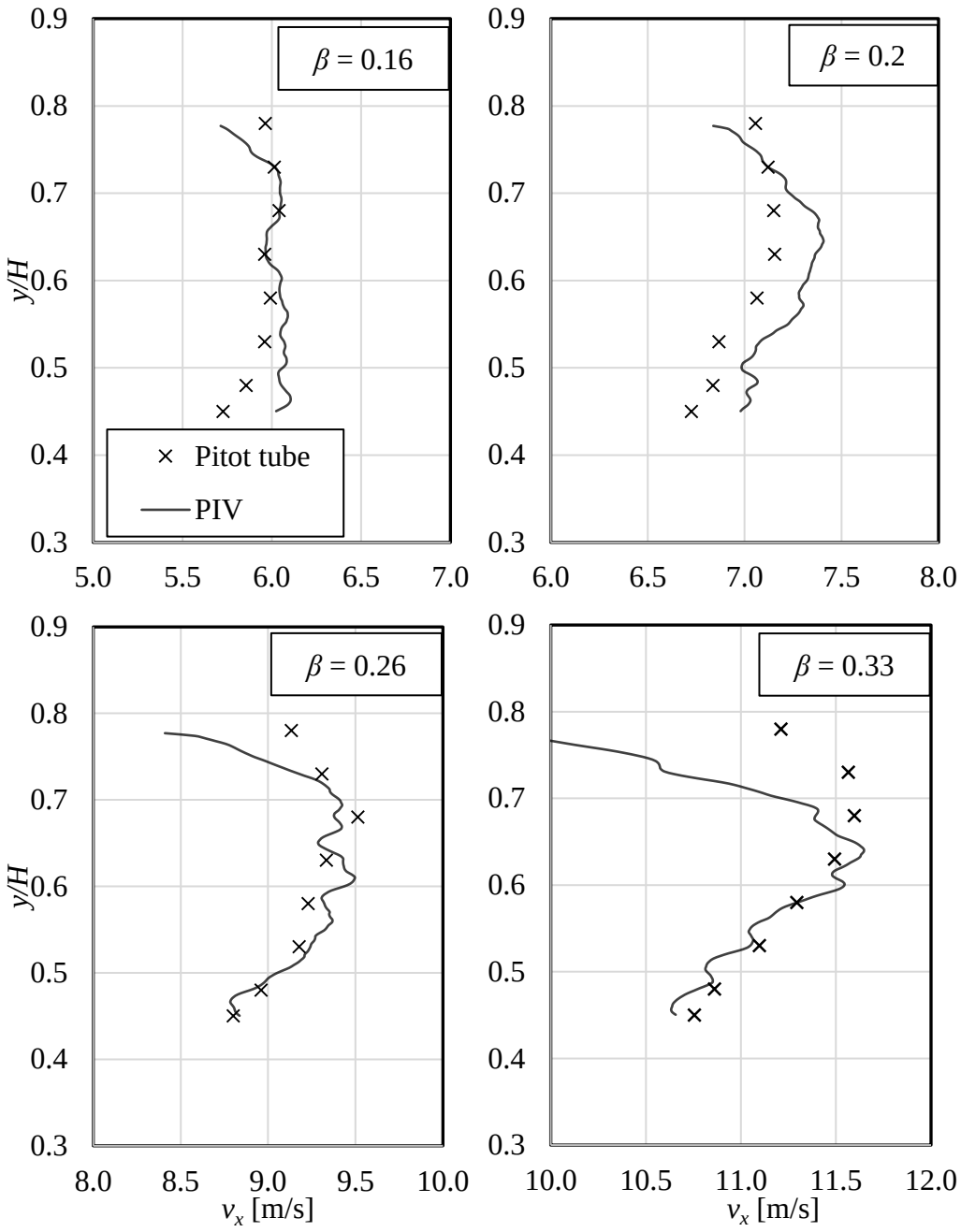

Figure E.2: PIV validation for cross-flows of β = 0.16, β = 0.2, β = 0.26 and β = 0.33

In general, there is a good correlation between the pitot tube measurements and the PIV except for the no-wind condition and the region closer to the fan platform ($y/H \approx 0.8$). There could however be discrepancies due to the flow not being perfectly aligned with the pitot tube. However, van der Spuy (2011) using hot wire anemometry could also not achieve a perfect correlation within his validation

procedure, between the PIV and the hot wire anemometry, and had recorded differences of similar magnitudes as given here.